A NUMERICAL INVESTIGATION INTO THE AERODYNAMIC EFFECTS OF TUBERCLES IN WIND TURBINE BLADES

A Dissertation
Presented to
The Academic Faculty

By

Giada Abate

In Partial Fulfillment
of the Requirements for the Degree
Doctor of Philosophy in the
School of Aerospace Engineering

Georgia Institute of Technology

May 2019

A NUMERICAL INVESTIGATION INTO THE AERODYNAMIC EFFECTS OF TUBERCLES IN WIND TURBINE BLADES

Approved by:

Professor Dimitri Mavris, Advisor
School of Aerospace Engineering
Georgia Institute of Technology

Professor Lakshmi Sankar
School of Aerospace Engineering
Georgia Institute of Technology

Professor Brian German
School of Aerospace Engineering
Georgia Institute of Technology

Dr. Scott Duncan
School of Aerospace Engineering
Georgia Institute of Technology

Dr. Kelly Griendling
Center of Innovation in Aerospace
Georgia Department of Economic Development

Date Approved: March 29, 2019

You want something, go get it. Period.

Will Smith – The Pursuit of Happiness

To my Family, who always supports me, even overseas.

ACKNOWLEDGEMENTS

The present work marks the end of another chapter of my life and academic career. I would like to thank numerous people who supported me during these five years at Georgia Tech. First, I thank my advisor, Dr. Mavris, who believed in me before but especially after the notorious moment when, sitting on a chair in front of him, I waited for the quals response. On that occasion, he confirmed it by giving me the "ASDL coin" and telling me the importance of working hard and reaching my objectives.

Second, I gratefully recognize the strong support of the amazing (old and new) members of Weber 107: Youngjun Choi, David Pate, Marc Canellas (and Rachel Haga), Michael Patterson, Xiaofan Fei, Matthew Warren, Emre Yilmaz, and Efe Yamac Yarbasi.

My years at Georgia Tech would not have been the same without the Italian team: Principio Tudisco, Marc Salvadori, Paola Zanella, and two of the best people in the world, Francesca Favarò and Matteo Carrara. Thank you, guys, for all the time spent together talking about work, soccer, food, and other silly Italian things.

I especially thank one of the most important people in my life, who is the reason I started a PhD at Georgia Tech and the person without whom I could not be successful, Andrea Garbo. He was always by my side, on good days and bad.

Finally, I send a big thank you to my family: my mom Aida, my dad Antonio, and my brother Domenico. They have been in every day of my life, even from a different continent.

These five years away from my country, my family, and my friends have been very difficult, but thanks to all these amazing people I was able to grow as a person, becoming more strong and confident than ever.

TABLE OF CONTENTS

LIST OF TABLES

LIST OF FIGURES

SUMMARY

Wind turbine performance is clearly affected by complicated environmental effects such as atmospheric turbulence, ground boundary layer, and variation of free-stream wind direction and amplitude. Since the main goal of a wind turbine is energy production, the irregular nature of the wind is considered the main obstacle to a constant power output. Sinusoidal modifications (i.e. tubercles) placed on the leading edge of wind turbine blades seem to mitigate this problem by allowing the wind turbine to operate across a greater range of wind speeds due to the generation of vortices which delay flow separation and improve the aerodynamic performance in the post-stall regime.

The main objective of the present study is to give insights into the application of tubercles on the leading edge of wind turbine blades, specifically the NREL Phase VI wind turbine, such that performance enhancement can be achieved. The main reason such a simplified wind turbine has been considered, rather than a modern multi-megawatt machine, is the availability of several experimental data from wind tunnel tests conducted at the NASA Ames Research Center.

Tubercles are sinusoidal bumps located at the leading edge of a humpback whale's flipper, which are able to improve flow attachment by acting like flow control devices similar to vortex generators. This discovery was the starting point for the development of several projects in the application of tubercles in different areas. Most of the previous studies focused attention on wings and how tubercles can improve their aerodynamic performance. Recently, research has been extended to wind turbine blades, emphasizing how introducing leading edge sinusoidal modifications in the blade design can improve the shaft torque in the post-stall regime due to a working principle similar to vortex generators. In fact, tubercles accelerate the flow at troughs where vorticity of alternate signs leads to counter-rotating vortices which re-energize the boundary layer and delay flow separation. Unfortunately, the

physical phenomenon behind tubercles is not entirely clear, and some researchers do not agree with the basic idea that tubercles work like vortex generators.

In the present work, tubercles have been applied to the NREL Phase VI wind turbine blade to study their effects on blade aerodynamics and wind turbine performance. In particular, tubercle effects on shaft torque and annual energy production (AEP) have been analyzed; more specifically, tubercle amplitude, wavelength, and spanwise location (or percentage of span covered) have been considered as design variables. Moreover, since the physical phenomenon behind tubercles is still not fully clear, a physical analysis has been conducted to understand their working principles and to compare the new findings with previous works. Since past research on wind turbine application considers random values of tubercle amplitude and wavelength, in the present work a more systematic study has been made by using a design of experiments (DoE) for the generation of tubercle configurations to test by a three-dimensional computational fluid dynamics (CFD) analysis.

In particular, the thesis research has been developed in three main phases. Firstly, amplitude and wavelength have been considered as two design variables for a Latin hypercube DoE, and 20 blades have been generated. Then, since it has been observed that tubercles on whale flippers are unevenly distributed and placed closer to the tip, only the tubercle spanwise location has been varied, keeping fixed amplitude and wavelength. Finally, all three design variables listed above (i.e. amplitude, wavelength, and spanwise location) have been considered together in a 57-case hybrid DoE (Latin hypercube + full factorial). All the blade geometries have been simulated by a three-dimensional CFD analysis, which was embedded in a high-performance computing simulation framework made of a geometry creation code, a mesher, and a CFD solver. Results in terms of shaft torque and AEP have been compared with the baseline turbine underlying the importance of tubercles especially in the off-design conditions, when the blade is fully stalled and characterized by a strong spanwise flow, which is partially blocked by the streamwise vortices generated by tubercles. The CFD results have been also used as training points for a surrogate model

generation, which helps to identify the regions in the design space where the performance improvement is relevant. In particular, tubercles seem to be beneficial in the design condition when placed closer to the blade tip; in the off-design regime, they can be extended from midspan to the blade tip that is considered the most influential area in the power generation. Values of tubercle amplitude and wavelength that positively affect the performance have been also identified in a limited region of the design space, which varies depending on the wind speed considered.

CHAPTER 1

MOTIVATION

1.1 Wind Energy

The global population is increasing day by day, and an intensive and uncontrollable development of human civilization and industrialization has a negative impact on the environment and energy resources. In order to prevent an energy crisis and to preserve the planet, it is necessary to consider renewable and "clean" energy sources. The use of fossil fuel based power plants is having negative effects on global warming and climate change; therefore, most countries of the world have decided to adopt several measures to reduce the level of atmospheric pollution [42, 61, 74]. At the beginning of the 20th century, the increasing interest by governments in the "health" of our planet and in the necessity of renewable energy sources permitted the re-emergence of wind as a significant source of energy. Improvements in technology and wind turbine efficiency have led to a dramatic reduction in the cost of wind energy since 1980 [12, 64], but other parameters, e.g., mean wind speed and the related annual energy production (AEP), are fundamental in the wind energy economy.

Since wind is a source easily available everywhere in the world, especially in some areas such as coasts and oceans where the mean wind speed is very high and more suitable for energy production (Fig.1.1), it will play a crucial role in the future energy supply [24]. In 2017, Asia-Pacific and China alone accounted for almost 47% of the total global investments in clean energy [45]. For eight years in a row, Asia was the largest regional market in the world for new wind power development, and China maintaned the leadership positon in terms of annual installations [45], followed by the United States and Germany (Fig.1.2). From 2001 to 2017, there was a relevant increase in the global wind energy production

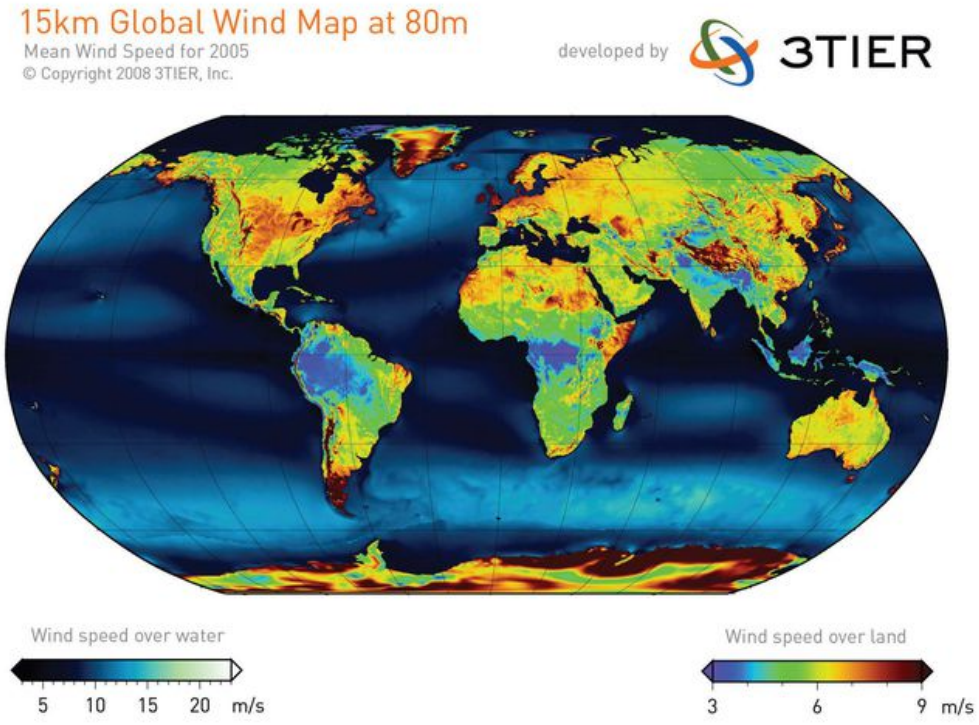

Figure 1.1: Global mean wind speed at an altitude of 80 m. [43]

(Fig.1.3), and according to the Global Wind Energy Council, this positive trend will characterize all the regions of the world, as shown in the market forecast for $2017-2021$ in Fig.1.4.

There are three main reasons why wind energy has grown so much in recent years: first, the need for renewable and "clean" energy sources to mitigate the global warming problem; second, the application of today's technology has permitted the solution to most of the issues related to wind power generation; third, the introduction of government policies to economically support wind energy [15]. The diffusion of wind as a source of energy is attributable also to new research studies from various scientific areas, including material science, computer science, aerodynamics, analytical design and analysis methods, testing and monitoring, and power electronics, that adapted their studies to wind energy applications. In particular, aerodynamic design methods that were originally developed for the aerospace industry have been successfully applied to wind turbines [15].

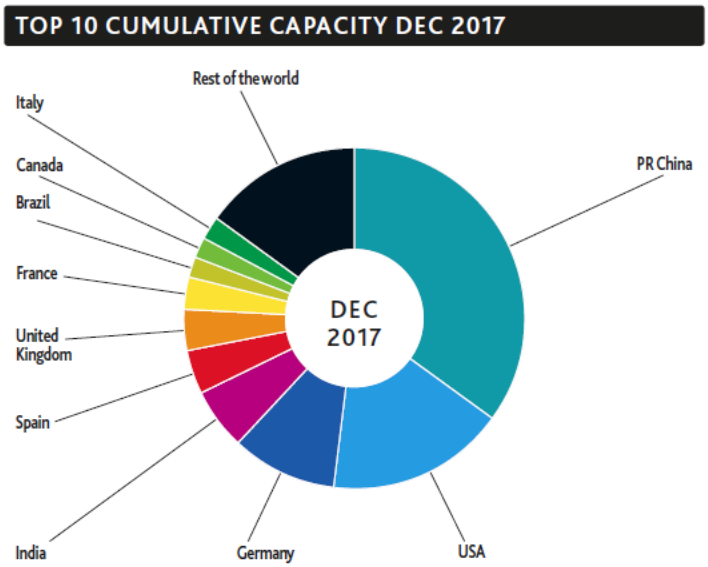

Country	MW	% Share
PR China	188,392	35
USA	89,077	17
Germany	56,132	10
India	32,848	6
Spain	23,170	4
United Kingdom	18,872	4
France	13,759	3
Brazil	12,763	2
Canada	12,239	2
Italy	9,479	2
Rest of the world	82,391	15
Total TO P10	**456,732**	**85**
World Total	**539,123**	**100**

Source: GWEC

Figure 1.2: Top 10 world countries in the production of wind energy in December 2017. [46]

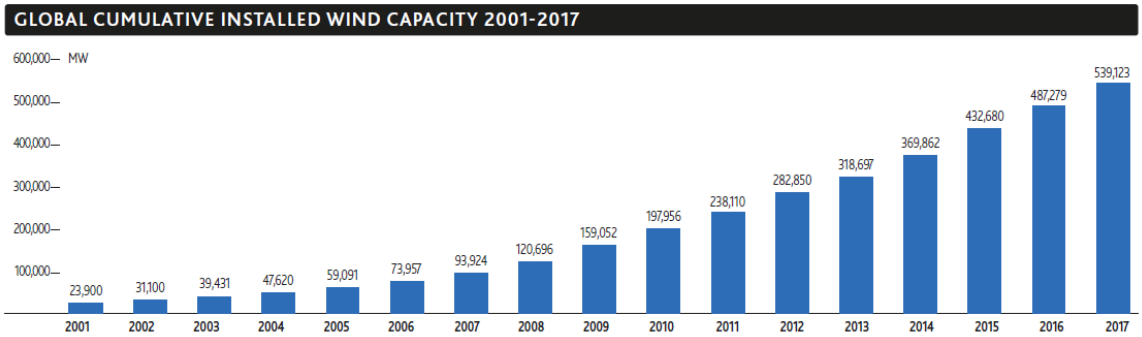

Figure 1.3: World wind energy production from 2001 to 2017. [46]

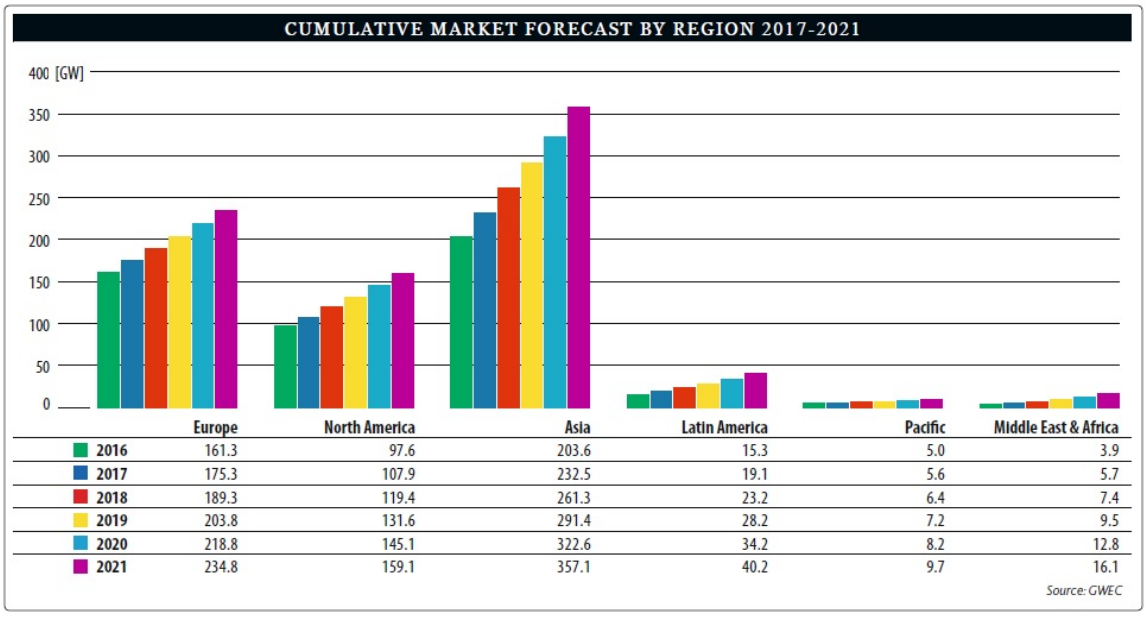

	Europe	North America	Asia	Latin America	Pacific	Middle East & Africa
2016	161.3	97.6	203.6	15.3	5.0	3.9
2017	175.3	107.9	232.5	19.1	5.6	5.7
2018	189.3	119.4	261.3	23.2	6.4	7.4
2019	203.8	131.6	291.4	28.2	7.2	9.5
2020	218.8	145.1	322.6	34.2	8.2	12.8
2021	234.8	159.1	357.1	40.2	9.7	16.1

Figure 1.4: Forecast of wind energy production until 2021. [45]

1.2 Wind Turbines

Wind turbines extract the kinetic energy of large masses of air moving over the earth's surface and convert it into electricity. The aerodynamic lift force on their blades produces a positive torque on a rotating shaft, leading to the generation of mechanical power, which is transformed into electricity by a generator [15, 91]. A representation of the different components of a wind turbine rotor is presented in Fig.1.5.

As already mentioned, the variability in wind intensity and direction causes some issues in the energy production, such as:

- variable wind turbine power output,
- need of power control devices,
- blade stall and inefficiency of the turbine at high wind speeds,
- strong cyclic loadings during stall on the generator and on the blades.

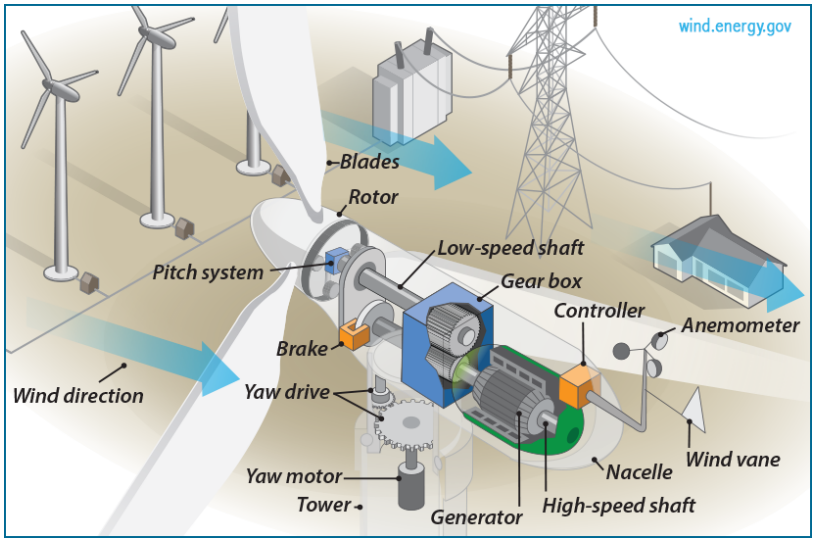

Figure 1.5: Schematic representation of wind turbine parts. [15]

The following sections present in more detail the problems listed above, giving particular attention to the link between wind speed and turbine performance.

1.2.1 Power Output Instability

One of the main issues characterizing wind energy production is the instability of wind turbine power output, which can be related to different phenomena, e.g., atmospheric turbulence, ground boundary layer, wind direction, and wind speed variation [56, 73]. In particular, wind speed variability plays an important role in the evaluation of wind turbine performance; therefore, the following sections present how wind speed is considered in the design process and what main parameters describe wind turbine performance.

1.2.1.1 Wind Speed Variation

The wind speed variation is usually represented by probability distribution functions, such as Weibull and Rayleigh distributions [52, 60, 66, 67, 86].

The Weibull probability density function requires the knowledge of two parameters: shape factor k and scale factor c, which are related to the mean wind speed $\overline{U}$. The equations representing the Weibull probability density function ($p(U)$) and the cumulative distri-

bution function ($F(U)$) are listed below [73]:

$$p(U) = \frac{k}{c}\left(\frac{U}{c}\right)^{k-1} \exp\left[-\left(\frac{U}{c}\right)^{k}\right] \tag{1.1}$$

$$F(U) = 1 - exp\left[-\left(\frac{U}{c}\right)^{k}\right] \tag{1.2}$$

Looking at the examples of Weibull probability density functions in Fig.1.6(a), an increase in the shape factor k causes the curve to become steeper, showing less variation in the parameter plotted on the x-axis, in this case the wind speed. A detailed description of the two factors k and c, and how to evaluate them starting from $\overline{U}$ are presented in Manwell *et al.* [73].

The Rayleigh distribution is a particular form of the Weibull one, in which the shape factor k is set equal to 2. Generally, it is preferable to use the Rayleigh probability distribution to represent wind speed variability since it is easier to implement compared to the Weibull distribution [108]. The probability density function ($p(U)$) and the cumulative distribution function ($F(U)$) are given by the following equations [73]:

$$p(U) = \frac{\pi}{2}\left(\frac{U}{\overline{U^2}}\right) exp\left[-\frac{\pi}{4}\left(\frac{U}{\overline{U}}\right)^{2}\right] \tag{1.3}$$

$$F(U) = 1 - exp\left[-\frac{\pi}{4}\left(\frac{U}{\overline{U}}\right)^{2}\right] \tag{1.4}$$

Examples of Rayleigh probability density functions for different values of mean wind speed are plotted in Fig.1.6(b).

1.2.1.2 Wind Turbine Performance

As described previously, wind turbines are subject to complicated environmental phenomena–like wind speed variability–that affect power generation. The probability density functions

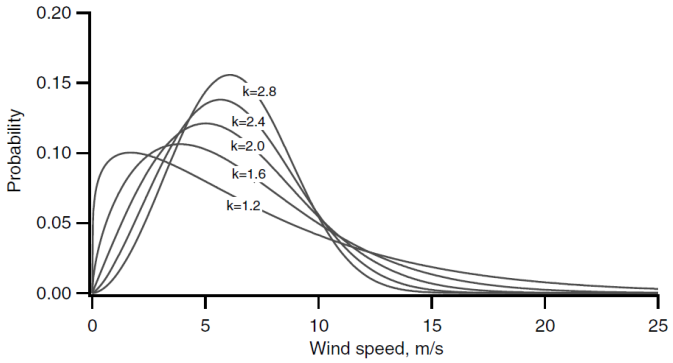

(a) Weibull

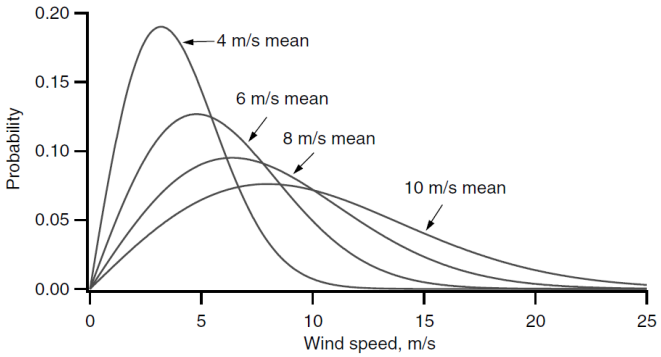

(b) Rayleigh

Figure 1.6: Examples of probability density functions. [73]

introduced in the previous section (Sec.1.2.1.1) are used to evaluate the wind speed effect in the calculation of the annual energy production, which is the average energy produced by a wind turbine in one year:

$$AEP = \overline{P}_{WT} \times 365 \times 24 \tag{1.5}$$

where $\overline{P}_{WT}$ is the average power produced in [kW], 365 are the days in a year, and 24 are the hours per day. The average power ($\overline{P}_{WT}$) is the integral of the power generated at a given wind speed ($P(U)$) multiplied by the probability of that wind speed ($p(U)$):

$$\overline{P}_{WT} = \int_0^\infty P_{WT}(U)p(U)dU \tag{1.6}$$

For the calculation of $p(U)$, it is possible to use the Weibull or the Rayleigh equations described in Sec.1.2.1.1. The power generated by the turbine (P_{WT}) is different from the power available in the wind (P_w). Wind turbines extract kinetic energy (E) from the wind, transforming it into electricity; the kinetic energy of a stream of air with mass m and moving with a velocity U is given by:

$$E = \frac{1}{2}mU^2 \tag{1.7}$$

Considering a wind rotor of cross-sectional area S (Fig.1.7) exposed to a wind stream, the energy per unit time (power available in the wind) can be expressed by the following equation:

$$P_w = \frac{1}{2}\rho SU^3 \tag{1.8}$$

The parameters affecting P_w are air density ρ, rotor area S, and, in particular, wind speed U, which is more prominent due to its cubic relationship with the power [74]. Again the power available in the wind is different from the power generated by the turbine because when the wind passes through the turbine, a portion of its kinetic energy is transferred to

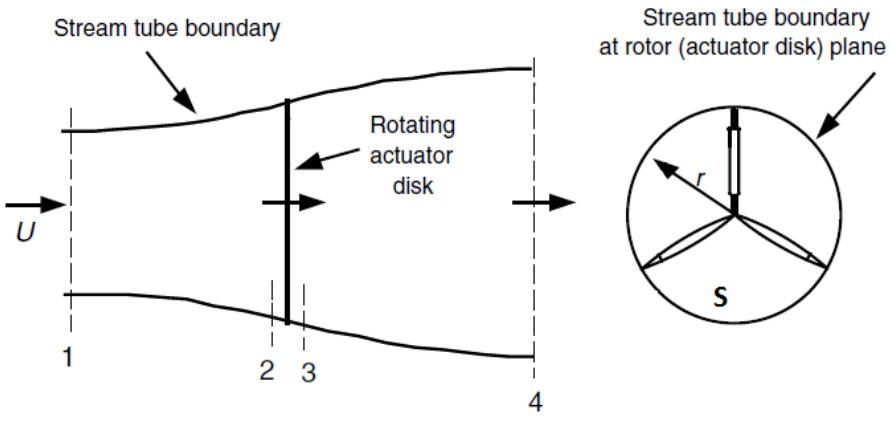

Figure 1.7: Schematic representation of a wind turbine rotor. [73]

the rotor while the remaining is carried away by the air leaving the turbine. Therefore, the actual power generated (P_{WT}) is the power available in the wind multiplied by a power coefficient (C_P) that represents the efficiency of the energy transfer from wind to rotor:

$$P_{WT} = C_P P_w \tag{1.9}$$

The maximum theoretical value of the power coefficient is known as the Betz limit and is equal to 59.3% (or 16/27). The derivation of the Betz limit is available in Manwell *et al.* [73].

As previously emphasized, power generated by a wind turbine is strongly linked with wind speed, and this relation is described by the power curve. An example is shown in Fig.1.8; this characteristic curve is used to easily predict the energy production of a wind turbine without considering the technical details of its components. The power curve is defined by three elements:

- **Cut-in speed**: the minimum wind speed at which the turbine will deliver useful power;
- **Rated wind speed**: the wind speed at which the rated power (generally the maximum power) is reached;

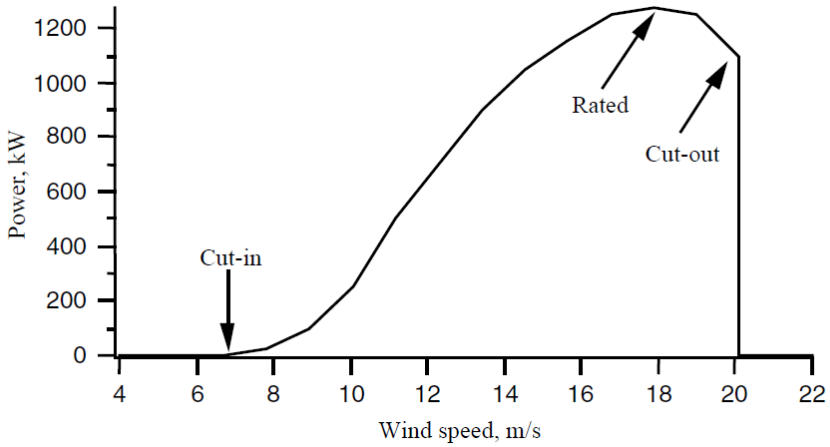

Figure 1.8: Wind turbine power curve. [73]

- **Cut-out speed**: the maximum wind speed at which the turbine is allowed to deliver power.

The cut-out speed is the upper limit of the wind speed given by engineering design and safety constraints [73].

1.2.1.3 Power Control Strategies

As presented in Sec.1.2, one of the main wind turbine issues is the variable power output due to the nature of the wind. In the case of strong wind conditions, it is necessary to waste part of the excess wind energy to avoid damages to the turbine. For this reason, all wind turbines require some power control mechanisms to adjust their operative condition depending on the wind speed. These power control strategies are divided into two categories: pitch and stall controls.

By using the pitch control, it is possible to change the blade pitch angle to calibrate the power generated by the turbine. In the case of high wind speeds, the blades are slightly pitched out of the wind to reduce the power generated, with the final purpose to go below the rated power limit, and, thus, avoid turbine damages. Conversely, when the wind speed decreases and the turbine produces less power, the blades are pitched into the wind to in-

crease the power output. Designing a pitch-controlled wind turbine is very difficult because it is necessary to ensure that the rotor blades pitch exactly the amount required; every time the wind changes, the blades are pitched a few degrees in order to keep the rotor blades at the optimum angle of attack to maximize the power output.

Stall control strategies could be passive or active. Passive stall-controlled wind turbines have blades with a fixed pitch angle, aerodynamically designed and mounted on the rotor such that for high wind speeds (i.e. above rated wind speed), the blades stall gradually, leading to a drop in the generated power below the rated one. The stall control is much simpler than the pitch method since it does not need moving parts in the rotor; however, it is more complex in the aerodynamic blade design with related challenges in the turbine structural dynamics. In spite of this, two thirds of wind turbines currently installed in the world are stall-controlled machines [15]. An increasing number of large wind turbines (i.e., 1 MW and up) are being developed with an active stall power control [15]. This type of machine has pitchable blades such that at low wind speeds, they are pitched to reach rated power; once that happens, it is necessary to reduce the power generated by pitching the blades again to reach stall. Active stall methods permit a more accurate control of the power oputput compared to the passive stall strategy.

1.2.2 Summary

Wind turbines work in very difficult wind conditions that can lead to the following issues:

- variation of the power generated,
- need of power control strategies,
- stall and inefficiency of the wind turbine at high wind speeds,
- strong cyclic loading due to the stall.

Different solutions and devices can be applied to solve most of these problems, but recently a new method has been studied that consists of the application of sinusoidal modi-

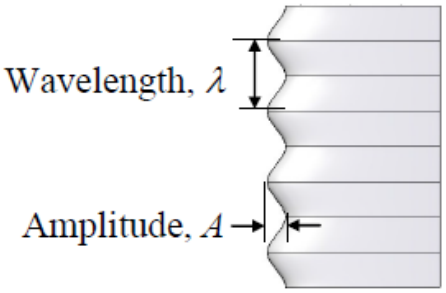

Figure 1.9: Tubercle amplitude and wavelength. [51]

fications (i.e., tubercles) on the leading edge of wind turbine blades. The following section will give a description of tubercles, their physical phenomenon, and how they can improve aerodynamic performance.

1.3 Tubercles

Tubercles are leading edge sinusoidal modifications characterized by two geometric parameters: amplitude and wavelength (Fig.1.9). The effects of these "bumps" were discovered during research on humpback whale flippers [37]. These immense animals (Fig.1.10) are considered the most "acrobatic" whales, and their ability to perform incredible rotations in the air and their high maneuverability underwater are due to the presence of tubercles that characterize the leading edge of their flippers [30, 93]. According to the observations made by Fish *et al.* [36], tubercles are unevenly distributed along the flipper with the largest tubercles starting at around 33% of the span; the intertubercular distances decrease distally, remaining relatively constant at $7-9\%$ of the span over the midspan (Fig.1.11). The number of tubercles is usually between 9 and 11, and as shown in Fig.1.10 and Fig.1.11, they are more concentrated at the flipper tip rather than the root.

The physical phenomenon behind tubercles is still being studied; however, most of the previous research indicates that they generate counter-rotating vortices that re-energize the

Figure 1.10: Tubercles on humpback whale flippers.

boundary layer and delay flow separation. As shown in Fig.1.12, the oncoming flow is deflected and redirected with a strong acceleration to the tubercle troughs, where vorticity of alternate sign is developed, which leads to the generation of counter-rotating vortices (Fig.1.13). These vortices re-energize the boundary layer by replacing the low-inertia fluid with the higher momentum fluid, resulting in a flow separation delay. A more detailed description of the physical phenomenon of tubercles will be presented in Sec.2.4.

Based on what has been said, the application of tubercles on wind turbine blades could improve the aerodynamic performance, especially when the blade is fully stalled, leading to stall delay and larger operative wind speed ranges. In Chapter 2, a literature review about the positive effects of tubercles on wing and wind turbine applications will be described.

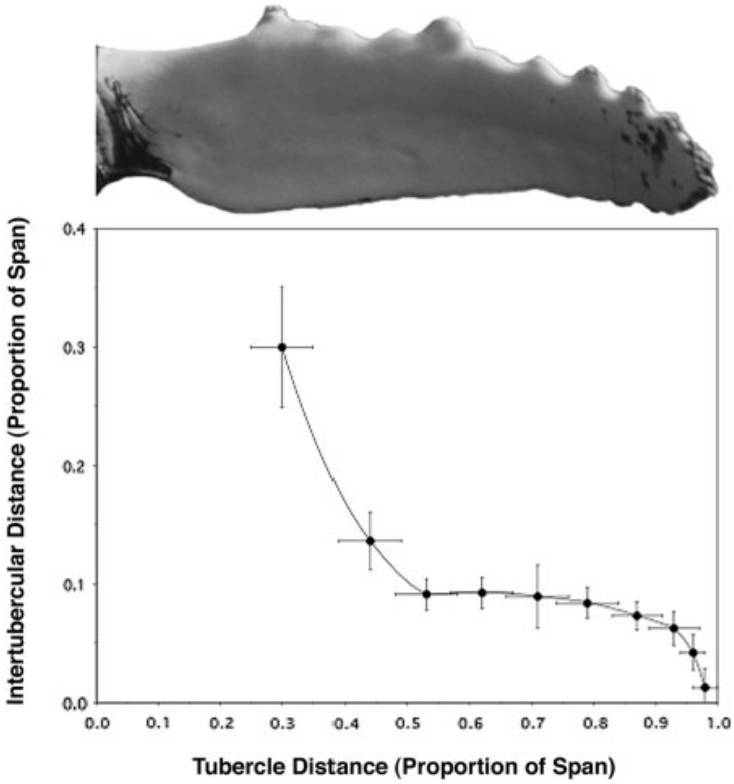

Figure 1.11: Intertubercular distance as a function of the distance of each tubercle from the shoulder of the whale. [36]

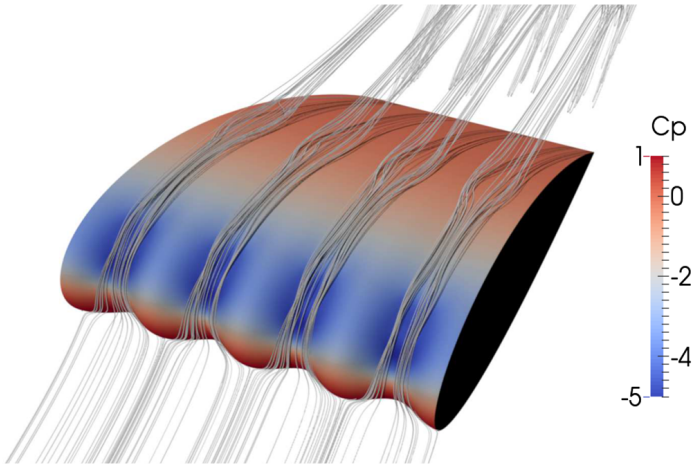

Figure 1.12: Flow redirected to the troughs of tubercles. [88]

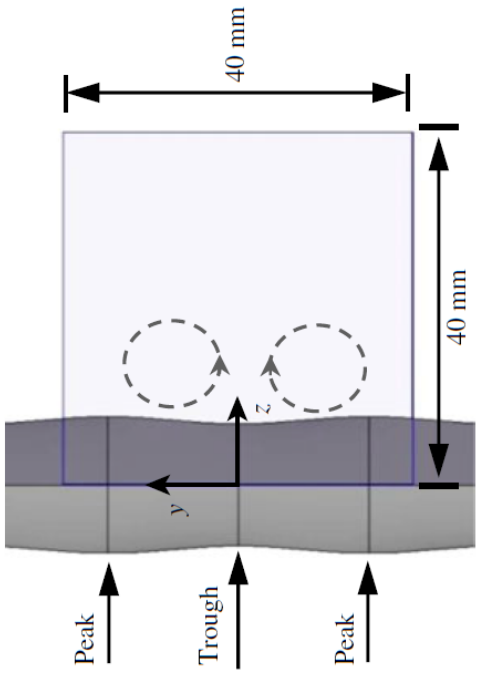

Figure 1.13: Vorticity of opposite sign at the troughs. [51]

CHAPTER 2

LITERATURE REVIEW

This chapter focuses on previous studies on tubercles, describing their effects on wing and wind turbine applications. Since leading edge bumps seem to work as passive flow control devices, an overview of the passive flow control mechanisms commonly used in wind turbine applications will be also provided.

2.1 Purpose of Tubercles on Humpback Whale Flippers

The humpback whale is one of the largest animals in the ocean, and it is also considered the most "acrobatic" whale. Its high maneuverability can be directly linked to its feeding ecology [51], and its famous ability to perform acrobatic turnings in the air is due to the presence of tubercles on the leading edge of its flippers.

One of the first studies on tubercles was conducted by Fish and Battle in 1995 [37]; they analyzed and described the shape of a humpback whale's flipper in terms of hydrodynamic parameters. They emphasized how leading edge tubercles on flippers can be considered flow control devices that are able to maintain stability and create force imbalances for maneuvering [37]. By analyzing a 9.02 m male humpback whale's flipper, Fish and Battle noticed an uneven distribution of tubercles along the span; as shown in Fig.2.1, the largest tubercle (T1) is located at 33% of the span, and the smallest (T11) is close to the tip at 99% of the span. The intertubercular distances are almost constant between T2$-$T3 and T7$-$T8, and they decrease moving toward the tip. Fish and Battle noticed that flippers have an elliptical planform, which is considered the optimal shape to achieve a uniform lift distribution; they also analyzed the mid-span section, finding some similarities with the NACA $63_4 - 021$ airfoil. Moreover, looking at the number and position of tubercles along

the flipper span, Fish and Battle supposed that these leading edge bumps act as flow control devices which generate vortices that are able to delay flow separation and result in the high maneuverability typical of humpback whales [33, 35].

To better understand the purpose of tubercles, Miklosovic *et al.* [78] tested whale flipper models in a wind tunnel. They measured lift and drag as a function of the angle of attack, and compared the results with the same flipper model without tubercles (Fig.2.2). An incompressible and steady state flow was considered for the test with a maximum Mach number of 0.2 and a Reynolds number between $5.05 \cdot 10^5$ and $5.2 \cdot 10^5$, which is in the operative range of an adult animal. In Fig.2.3, results in terms of lift coefficient, drag coefficient, and lift-to-drag ratio are reported. From the comparison with the smooth flipper model (solid line), the lift coefficient starts to increase from around 12° of the angle of attack, whereas in terms of drag coefficient, the two models have comparable values up to 12° but then the flipper with tubercles shows better results. Miklosovic *et al.* concluded that leading edge tubercles improve flipper performance, providing higher lift and lower drag in the post-stall regime. They also noticed a similarity with vortex generators since tubercles generate counter-rotating vortices that re-energize the boundary layer, delaying flow separation.

In 2007, Miklosovic *et al.* [77] extended their work, testing full-span and semi-span models. For the full-span flippers, Reynolds numbers of $2.74 \cdot 10^5 - 2.77 \cdot 10^5$ and a Mach number of 0.13 were considered; whereas, the semi-span tests were conducted at Reynolds numbers as high as $5.34 \cdot 10^5 - 6.31 \cdot 10^5$ and a Mach number of 0.21. All the flippers were based on the NACA 0020 airfoil profile, as shown in Fig.2.4. Looking at the results of the full-span (Fig.2.5) and semi-span (Fig.2.6) models, it is possible to affirm that incorporating tubercles on the leading edge of flippers leads to performance enhancement, whereas an opposite trend is visible when they are applied to a full-span rectangular planform. From the comparison between full-span and semi-span models, Miklosovic *et al.* also concluded

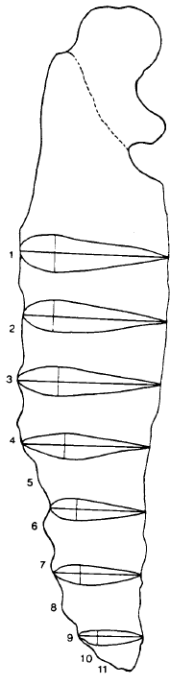

Figure 2.1: Schematic representation of a humpback whale's flipper. [37]

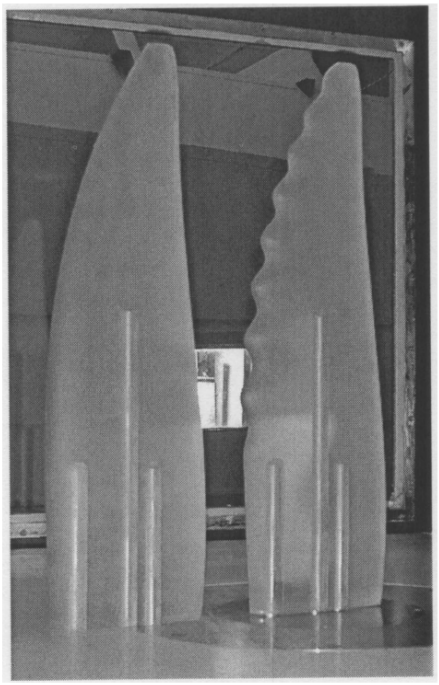

Figure 2.2: Smooth and scalloped humpback whale flipper models. [78]

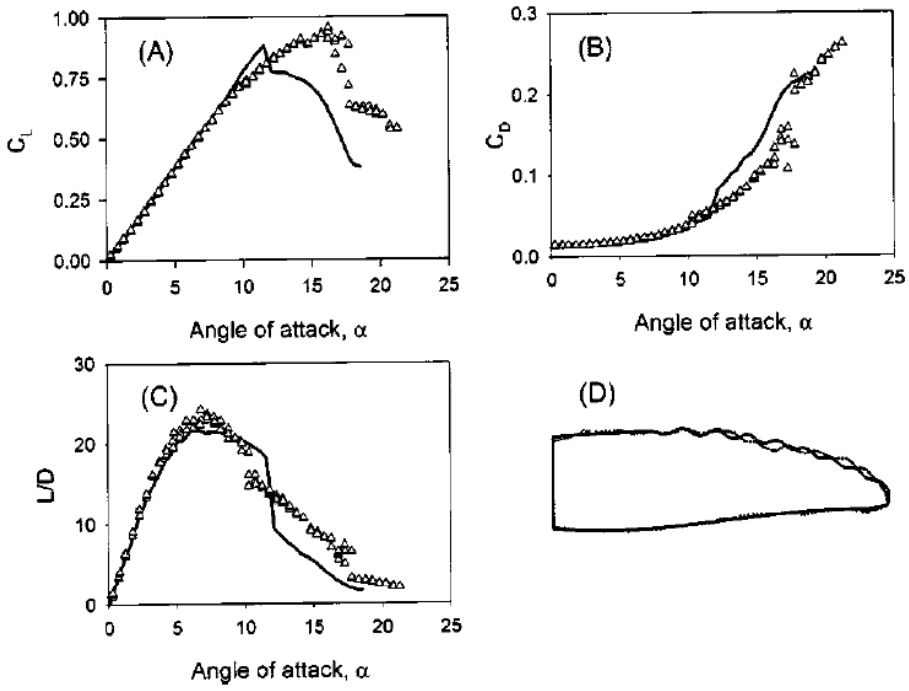

Figure 2.3: Lift and drag results compared with the smooth model (solid line). [78]

that tubercles provide a three-dimensional benefit. However, in the result analysis, it is important to note that different Reynolds number ranges were used for the two tests.

A computational study on whale flippers with and without tubercles was conducted by Pedro and Kobayashi [83]. They noticed higher aerodynamic performance in the model with tubercles close to separation due to the presence of streamwise vortices originated by the leading edge bumps (Fig.2.7). These vortical structures carry momentum to the boundary layer, delaying the trailing edge separation; moreover, they confine leading edge separation to the tip region [83].

Another important study on how tubercles affect the aerodynamic characteristics of humpback whale flippers was conducted by van Nierop *et al.* [94]. They demonstrated how a standard aerodynamic theory model could explain most of the phenomena observed experimentally. Despite what Miklosovic *et al.* found Ref.[78], van Nierop *et al.* stated that it is not possible that tubercles act as vortex generators, because their amplitude and wavelength are much larger than the boundary layer thickness [94]. Therefore, they propo-

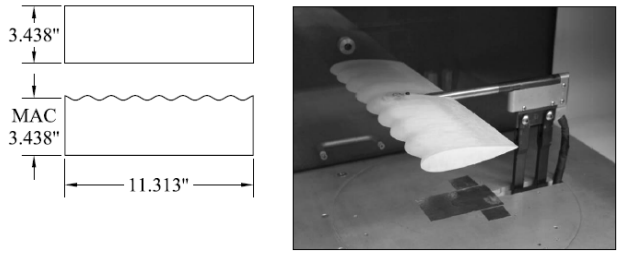

(a) Full-span models

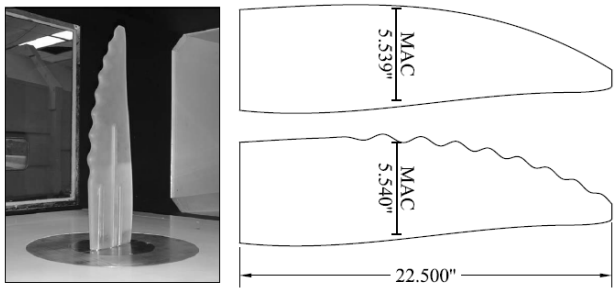

(b) Semi-span models

Figure 2.4: Models tested by Miklosovic *et al.*. [77]

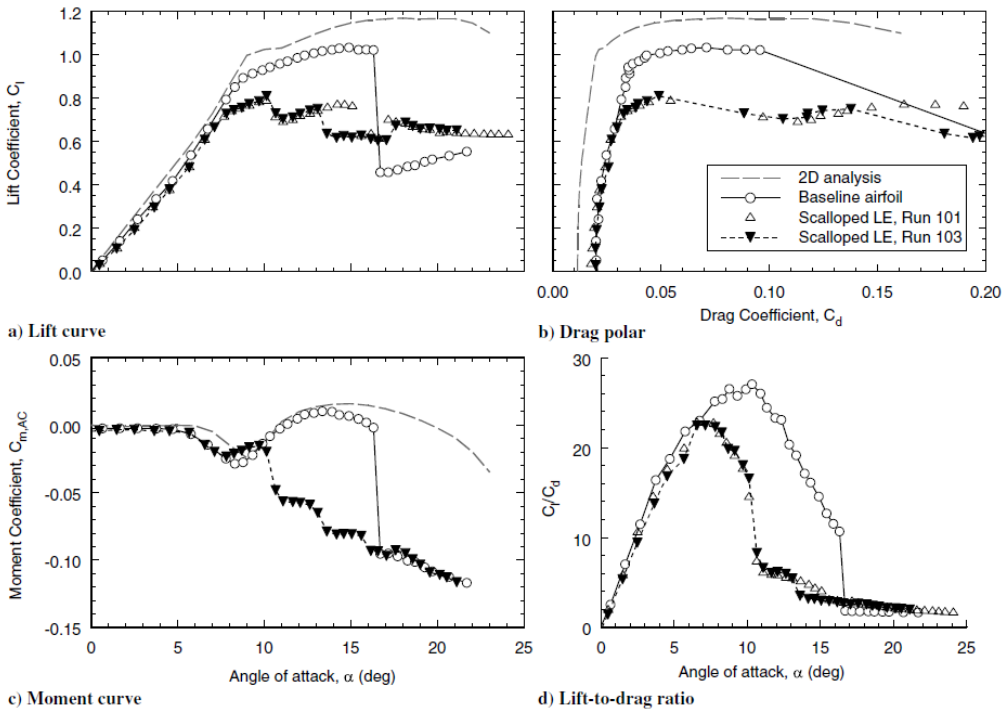

Figure 2.5: Full-span results. [77]

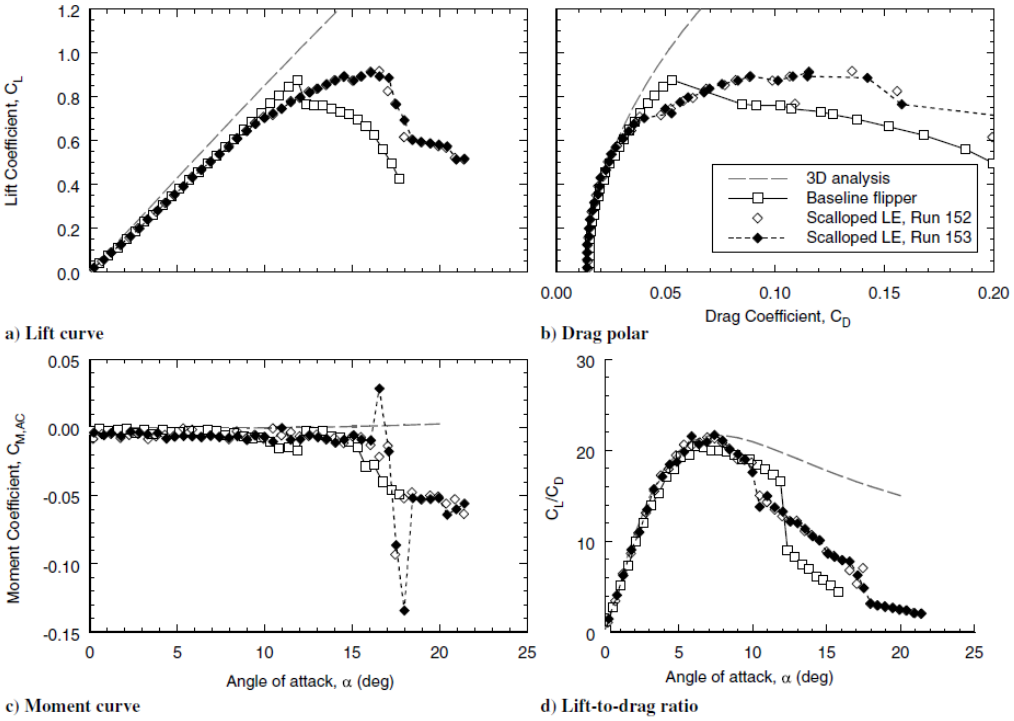

Figure 2.6: Semi-span results. [77]

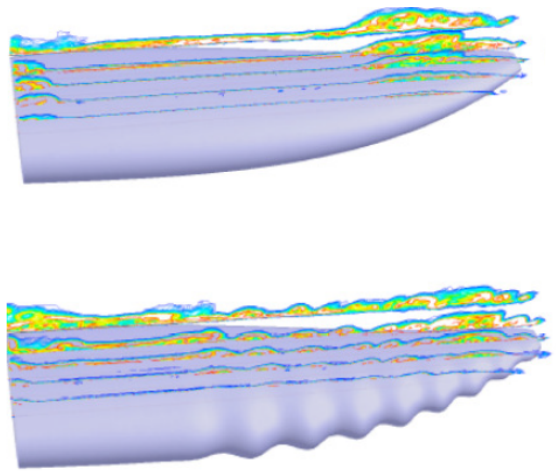

Figure 2.7: Vorticity in spanwise direction. [83]

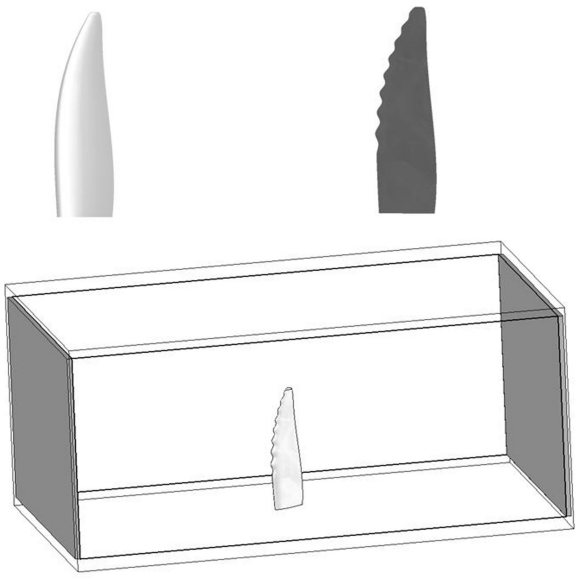

Figure 2.8: Geometries of the two models simulated by Weber *et al.*. [99]

sed a different flow control mechanism: leading edge bumps alter the pressure distribution on the flipper surface such that the boundary layer separation is delayed, resulting in a more gradual stall. Van Nierop *et al.* were the first to go against the common idea that tubercles work like vortex generators; they also emphasized the necessity to conduct deeper studies to better understand the physical phenomenon. A more exhaustive argumentation on similarities and differences between leading edge bumps and vortex generators will be presented in Sec.2.5.6.

One of the latest studies on tubercles applied to flippers was conducted by Weber *et al.* [99], who made computational simulations of two humpback whale flipper models (Fig.2.8). They noticed from flow visualization that separation appears at tubercle troughs right behind the leading edge in the flipper with tubercles, whereas, a trailing edge stall characterizes the smooth model. Moreover, at high angles of attack at which the regular flipper is fully stalled, the model with tubercles shows several regions of attached flow, leading to better performance in the post-stall regime [99].

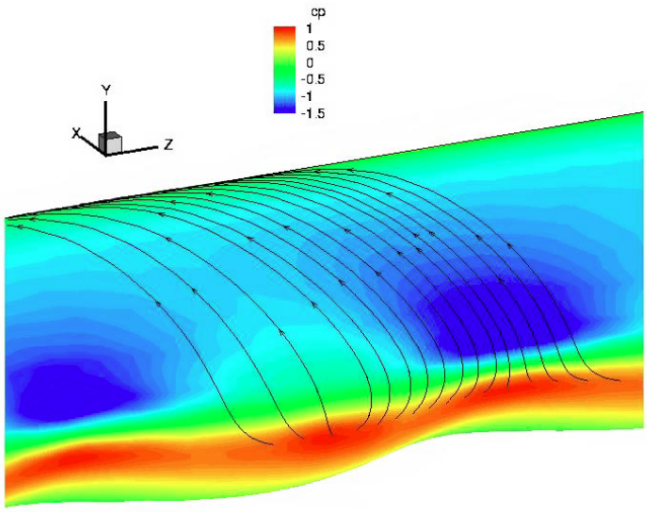

Figure 2.9: Streamlines. [97]

2.2 Tubercles Applied to Wings

Several studies have focused on the performance analysis of wings with leading edge tubercles. Watts and Fish [97] made some numerical simulations of finite-span wings with and without tubercles, noticing that leading edge bumps have strong effects on the oncoming flow. They deflect and redirect the flow to their troughs with a strong acceleration (Fig.2.9), resulting in low pressure regions (Fig.2.10). Unfortunately, Watts and Fish's work is characterized by a considerable limitation: they did not consider viscous effects and, therefore, they did not model boundary layer development and streamwise vorticity.

Stein and Murray [92] tested and analyzed three different airfoil models to better understand the stall mechanism associated with tubercles. In particular, they considered: a smooth airfoil, an airfoil with tubercles, and an airfoil with vortex generators (Fig.2.11). Results show inferior lift and drag performance in the model with tubercles compared to the smooth one. Moreover, flow analysis of the airfoil with tubercles and of the one with vortex generators revealed that the working principle of leading edge sinusoidal modifications as a flow control device is more similar to wing fences, since they create vortices able to prevent stall progression rather than re-energizing the boundary layer [92].

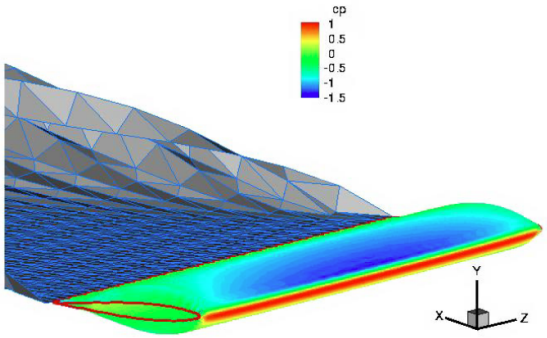

(a) Smooth wing

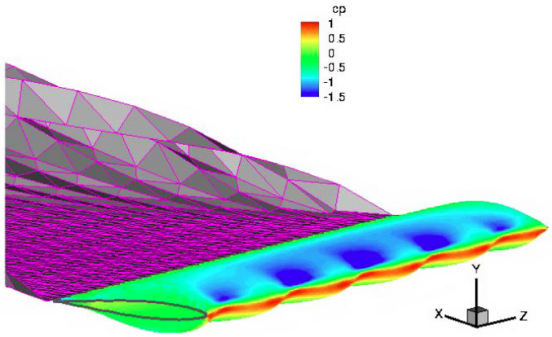

(b) Wing with tubercles

Figure 2.10: Simulation of flow over wings. [97]

Figure 2.11: Airfoil models used by Stein and Murray: smooth wing (upper left), wing with tubercles (upper right), wing with VGs (lower). [92]

Johari *et al.* [59] varied the values of tubercle amplitude and wavelength in the ranges of humpback whale flippers, and compared six models with the baseline one (Fig.2.12). In general, they noticed a different stall behavior between airfoils with tubercles and the baseline model, with a delay in the separation when tubercles are applied; moreover, leading edge bumps cause a reduction in lift coefficient when the angle of attack is below the baseline stall angle. However, in the post-stall regime, the tubercles can improve the lift coefficient by as much as 50% compared to the baseline model. By varying amplitude and wavelength, Johari *et al.* studied also the effects of those geometric parameters in stall, lift, and drag. In particular, airfoils with smaller amplitude performed best in terms of stall angle and maximum lift coefficient, and higher values of amplitude resulted in softer stall characteristics. Wavelength effects were considered minor by the authors, even though tubercles with smaller wavelength achieved higher maximum lift coefficient and stall angle with lower drag.

Hansen *et al.* [49] tested tubercles on two different full-span wings: NACA 0021 and NACA 65-021 airfoil sections. The NACA 0021 was chosen because it was considered more similar to the cross-sectional profile of the whale's flipper; the NACA 65-021 was used as a different type of airfoil for comparison purposes since it has the maximum thickness position further aft at 50% of the chord. Results show that both wings have higher lift coefficient and larger stall angle when tubercle amplitude is reduced. However, in the post-stall regime, the performance of wings with larger amplitude seems to be more favorable. The wavelength reduction leads to improvements in maximum lift coefficient, stall angle, and post-stall characteristics. Neverthless, there is a point at which further reduction in wavelength has a negative impact on performance. By comparing the results with the baseline wing, Hansen *et al.* noticed also that tubercles are more beneficial in the NACA 65-021 wing rather than the NACA 0021 because when the position of the maximum thickness is further aft, as in the NACA 65-021, the extend of the laminar boundary layer is greater, and thus tubercles can be more beneficial [49].

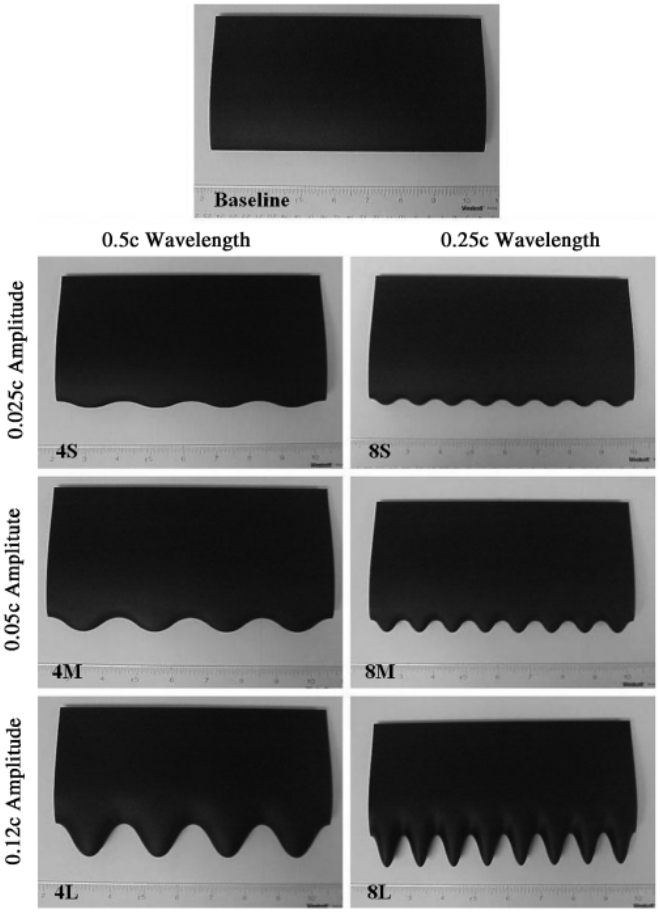

Figure 2.12: Airfoil models used by Johari *et al.* [59]

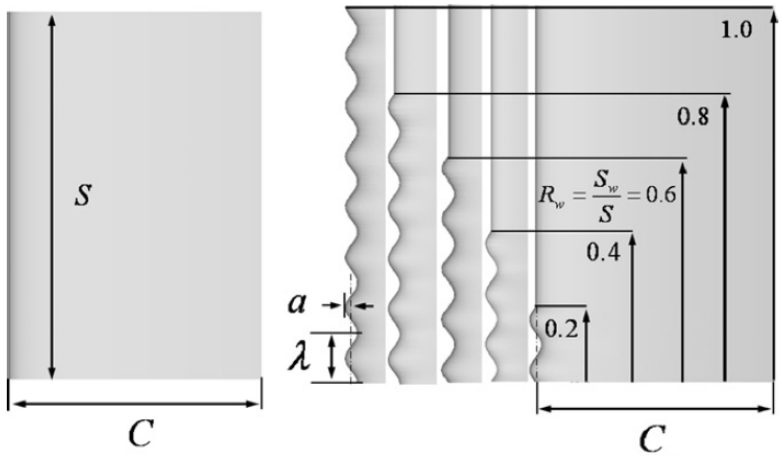

Figure 2.13: Baseline and five models tested by Yoon *et al.* [103]

Yoon *et al.* [103] numerically investigated the effects of a wavy leading edge on flow hydrodynamic characteristics around a rectangular wing by changing tubercle position along the span. They tested five different values of waviness ratio, defined by the wing span length over the spanwise length covered by tubercles at three different angles of attack. Figure 2.13 shows the five models tested, characterized by fixed amplitude and wavelength. For low angles of attack, the effect of wavy leading edge modifications on hydrodynamics forces and and flow structures is almost negligible. As the waviness increases, the stall occurs sooner than in the smooth wing; in the post-stall regime, lift coefficient increases in the wavy wings compared to the one in the baseline model. From a flow analysis, Yoon *et al.* found also that all the wings are characterized by spiral formations of limiting streamlines occurring in the wavy troughs, where a relatively low pressure has been noticed (Fig.2.14).

Another recent study was conducted by Bolzon *et al.* [14] who implemented Prandtl's lifting line theory to determine the effects of tubercle amplitude and wavelength on lift coefficient, induced drag coefficient, and lift-to-drag ratio of a NACA 0021 wing. In addition to those two tubercle gometric parameters, they also considered the phase of tubercles, meaning how tubercles end at the wing tip. In Fig.2.15, there is a schematic representation of the tubercle wing parameters (Fig.2.15(a)) and the geometry of the last tubercle once

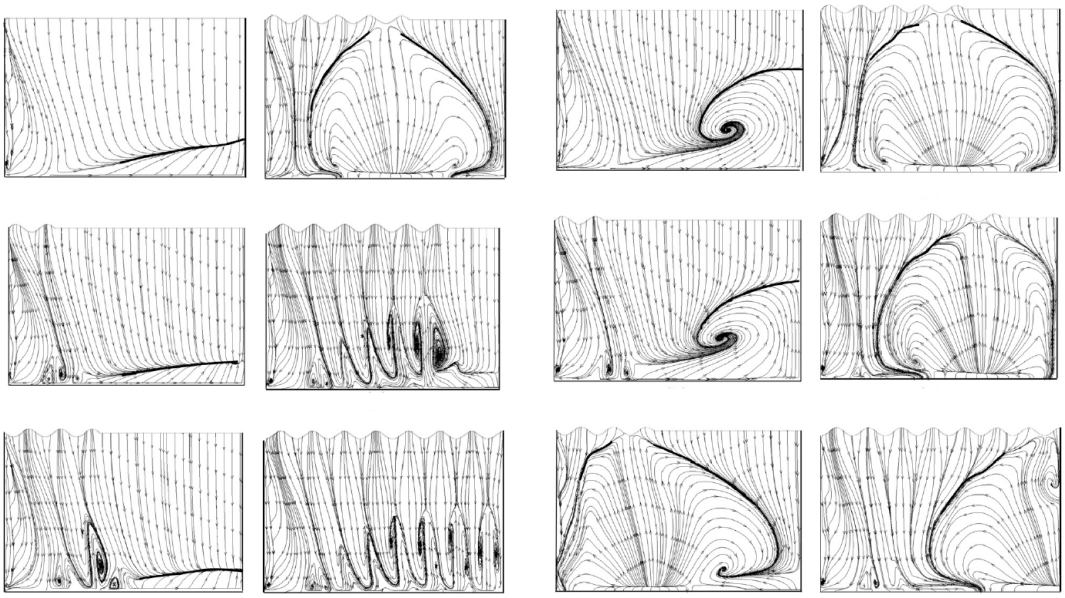

(a) $\alpha = 16°$ (b) $\alpha = 20°$

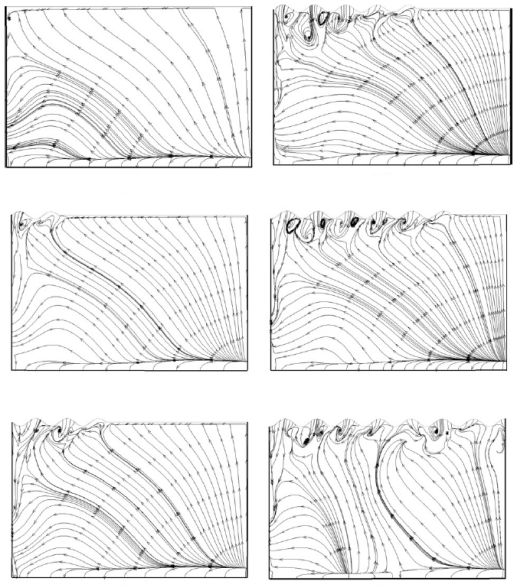

(c) $\alpha = 32°$

Figure 2.14: Limiting streamlines on the upper surface. [103]

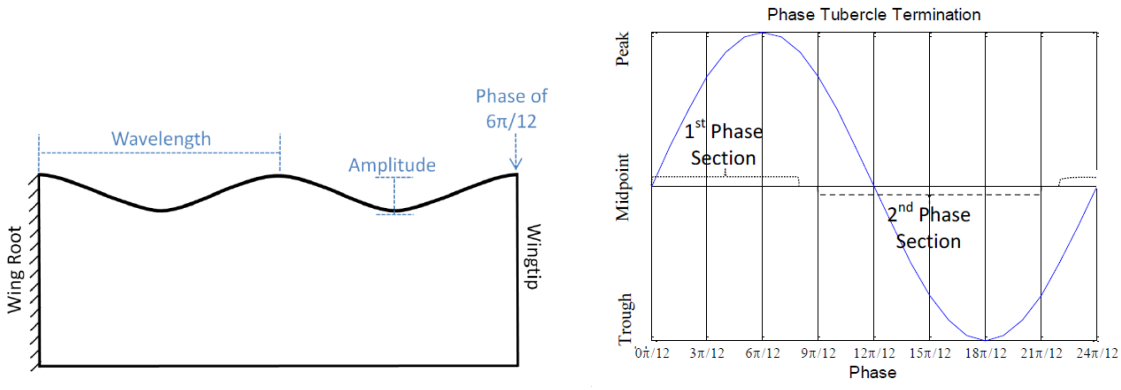

(a) a (b) b

Figure 2.15: Amplitude, wavelength, and tubercle phase considered by Bolzon *et al.* Ref.[14].

a specific phase is given (Fig.2.15(b)). Bolzon *et al.* found that without accounting for the phase, tubercle amplitude and wavelength have only a little impact on lift coefficient, induced drag coefficient, and lift-to-drag ratio; however, coupling them with the phase, the geometric parameter effects are more pronounced. In particular, the greatest increase of lift-to-drag ratio was obained with a phase of approximately $0\pi/12$, meaning the last tubercle ending between a trough and a peak; then again, a decrease in lift and induced drag coefficients was also visible. To reach the maximum value of lift and induced drag coefficients, it is necessary to have a wing with a $12\pi/12$ tubercle phase, corresponding to the last tubercle shape between a peak and a trough; however, the lift-to-drag ratio decreases for this specific configuration.

DePaula *et al.* [75, 81] experimentally investigated the wavy leading edge phenomena for the very thick airfoil NACA 0030 at low Reynolds number. In particular, three tubercle configurations (Fig.2.16) in terms of amplitude and wavelength were tested in a Reynolds number range between 5000 and 290.000. For the highest Reynolds number, results show worse aerodynamic performance for the wavy leading edge compared to previous studies on thinner airfoils. However, at a Reynolds number of 120.000, one tubercle configuration

Figure 2.16: Tubercle configurations tested by DePaula *et al.* Ref.[81].

exhibited an increase of 19.4% in lift coefficient, better aerodynamic performance, and a stall delay.

In summary, most of prior works on tubercle wing application found some advantages in lift and drag coefficients in the post-stall regime, while negative or irrelevant effects are noticible in other flow conditions. Moreover, stall is delayed in wings with tubercles due to the generation of streamwise vortices, which seem to re-energize the boundary layer or block the development of spanwise flow. The positive effects of tubercles in the post-stall regime can be useful in wind turbine application since they can permit to increase the operative wind speed range by postponing the blade stall to higher wind speeds, and therefore, increase the power generated at wind conditions where usually the wind turbine blade stalls and becomes inefficient. Tubercles in wind turbine application will be presented in the following section.

2.3 Tubercles Applied to Wind Turbines

Only a portion of the previous research analyzes the effects of leading edge tubercles on wind turbine performance [3, 6, 7, 9, 44, 53, 54, 55, 63, 96, 106], and the most relevant studies are presented below.

In 2009, a prototype of a blade with leading edge sinusoidal modifications was tested by the Wind Energy Institute of Canada (WEICan) [9]. A conventional Wenvor 10 meter two-blade turbine was retrofitted by fabricating and attaching leading edge tubercle elements to produce the first model of wind turbine with tubercles (Fig.2.17). The machine was tested for several months and the results were compared with the regular Wenvor turbine. It was found that annual power production was increased by 20%, turbine noise was reduced considerably, and the responsiveness to rapid changes in wind speed was significantly improved. Furthermore, other advantages were found, including:

- tubercles generate higher lift by energizing the boundary layer with better results compared to vortex generators;
- tubercles stall gradually and, even when they partially stall, they continue to generate more lift than any other airfoil type (useful for wind turbines with no active pitch control);
- tubercles mitigate some undesiderable vortices and reduce aeroelastic instabilities in the wakes;
- vortices generated between tubercles act as virtual fences, blocking the spanwise flow and delaying the tip stall; and
- the decrease in tip stall strength results in a reduction of noise and vibrations.

Another important study was conducted by Zhang and Wu [106]; they numerically investigated the aerodynamic characteristics of the NREL Phase VI wind turbine blade

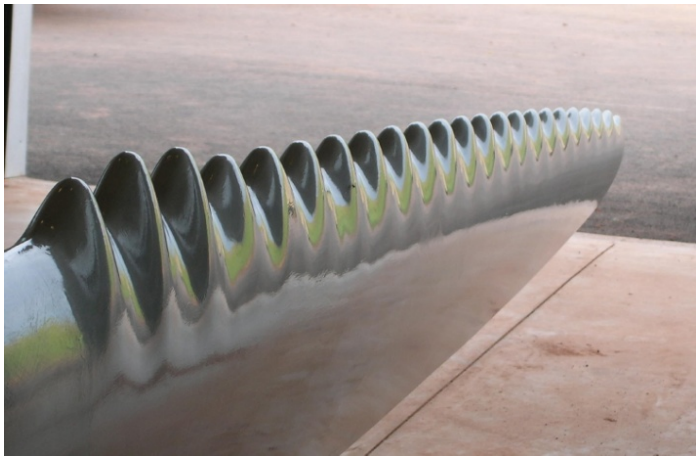

Figure 2.17: Wenvor blade with tubercles. [9]

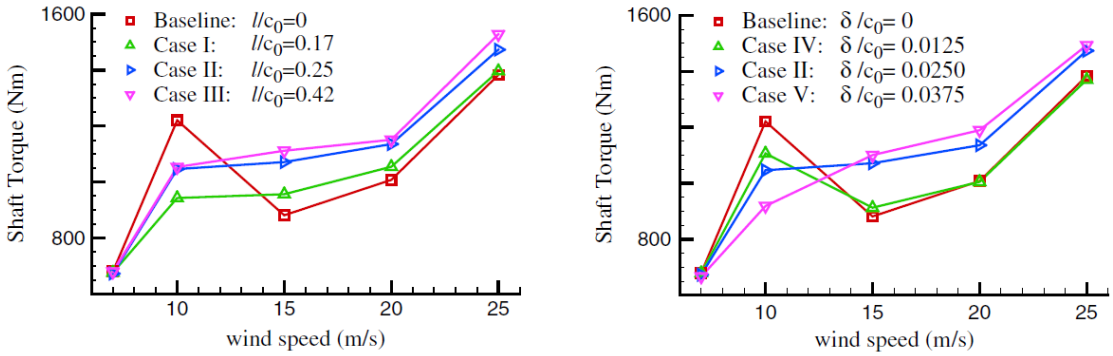

Figure 2.18: Shaft torque comparison. [106]

with random values of tubercle amplitude and wavelength. They simulated five different tubercle configurations at five wind speeds (i.e., 7, 10, 15, 20, 25 $\mathrm{m/s}$) assuming steady, incompressible, and fully turbulent flow. Although between 15 and 25 $\mathrm{m/s}$ the flow is characterized by some unsteady behaviors, they justified the steady assumption by running unsteady simulations and comparing the results with the steady ones. No visible differences between the two were noticed, confirming the reliability of steady flow assumption. Figure 2.18 presents the shaft torque comparison between the regular NREL blade (baseline) and the five tubercle configurations tested. A significant improvement is evident at high wind speeds (off-design regime) in blades with tubercles; however, an opposite trend is visible with movement toward to the design condition (10 $\mathrm{m/s}$).

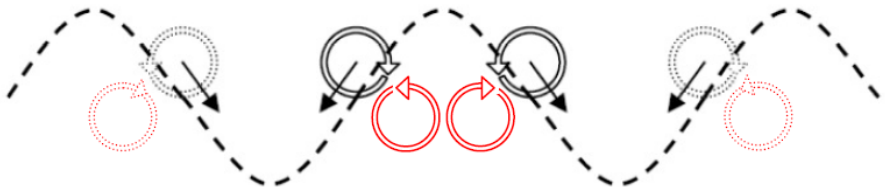

Figure 2.19: Schematic representation of vortex migration toward the troughs. [27]

2.4 Tubercle Physical Phenomena

The physical principle behind tubercles is still being investigated but according to past studies, the common idea is that tubercles act like vortex generators by producing vortices that re-energize the boundary layer, delaying flow separation [13].

Custodio [27] suggested that lift enhancement given by the application of tubercles on wings is related to the migration of the generated counter-rotating vortices toward the troughs (Fig.2.19), and their merging is responsible for the observed low-pressure regions on the suction surface. In the post-stall regime, the increase in the angle of attack results in the generation of stronger vortices, leading to a high lift enhancement.

Favier *et al.* [31] performed numerical simulations on a NACA 0020 infinite wing in a deep stall regime ($\alpha = 20°$) with and without the presence of tubercles on the leading edge and considering a low Reynolds number. Amplitude and wavelength were changed, identifying three tubercle configurations to simulate (Fig.2.20). They found that with a certain choice of amplitude (i.e., 7% of the chord) and wavelength (i.e., around 1% of the chord), the wake topology is drastically modified, the shedding regime disappears, and the flow is dominated by streamwise vortical structures that leads to a partial flow attachment in correspondence with the peaks. However, this study considered Reynolds numbers below the ranges characterizing humpback whale flippers; therefore, it is necessary to look at higher values, close to those observed in nature, and at least large enough to achieve fully turbulent regimes.

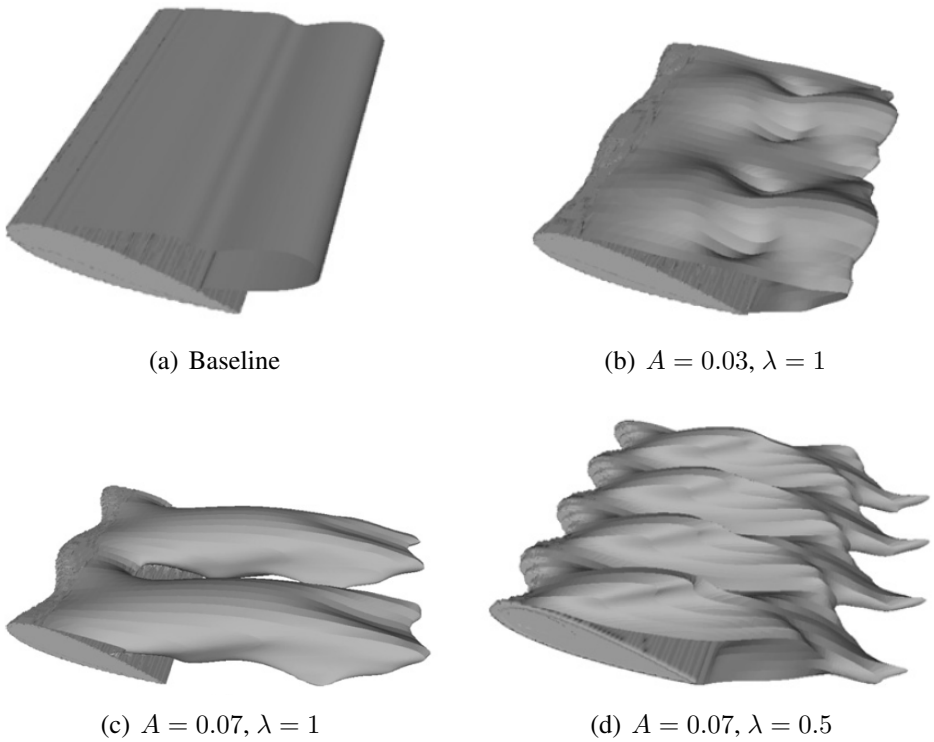

(a) Baseline

(b) $A = 0.03$, $\lambda = 1$

(c) $A = 0.07$, $\lambda = 1$

(d) $A = 0.07$, $\lambda = 0.5$

Figure 2.20: Recirculation regions shown by isosurfaces of zero longitudinal velocity. [31]

Dropkin *et al.* [28] computed numerically the flowfield and the aerodynamic forces on a two-dimensional airfoil with sinusoidal leading edge modifications; results were also compared with the baseline NACA $63_4 - 021$ airfoil. Amplitude and wavelength were set constant at 12% and 50% of the mean chord length, respectively. The two models tested are presented in Fig.2.21. Looking at the pathlines of the baseline and modified airfoils in Fig.2.22, the flow separation pattern is different between the two models. In the baseline airfoil, the separation starts at the trailing edge and moves upstream with the increase of the angle of attack; in the modified model, the flow appears to be attached at $\alpha = 6^\circ$ but it converges and twists, indicating the presence of streamwise vorticity over the surface. Increasing the angle of attack, the pathlines converge and diverge in adjacent troughs with a biperiodic pattern, and the flow separation happens farther downstream compared to the baseline airfoil. At $\alpha = 18^\circ$, the pathlines are still characterized by the biperiodic pattern, which disappears at 24° where the only flow attached is over the tubercle peaks. Dropkin

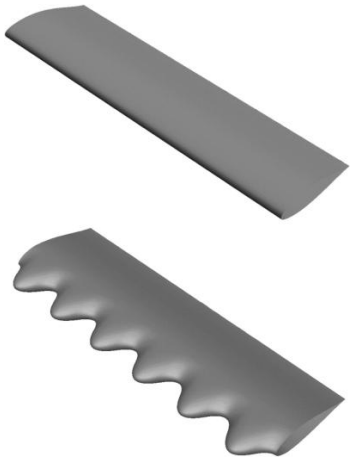

Figure 2.21: Baseline and modified airfoils simulated by Dropkin *et al.* [28]

et al. noticed also some effects on the pressure distribution; in particular, symmetric and periodic low-pressure regions appear in the troughs of tubercles at low angles of attack (Fig.2.23), and they evolve into more complicated patterns at higher α. The presence of low-pressure regions characterizes the modified airfoil also at high angles of attack, leading to an increase in lift. Conversely, the baseline model has uniform surface pressure distribution up to the separation line and multiple stall cells afterward.

The biperiodic vortical structures observed by Dropkin *et al.* were confirmed by Sousa and Camara [76]. They numerically simulated infinite wings with leading edge tubercles, and noticed that vortices are generated at the troughs, remaining approximately periodic along the spanwise direction at lower angles of attack. However, when the incidence increases, the biperiodic pattern disappears.

Zhang *et al.* [104, 105] tested a full-span NACA $63_4 - 021$ wing with tubercles at low Reynolds numbers ($< 10^5$) with an angle of attack between $0°$ and $90°$. Amplitude and wavelength of tubercles were fixed at 0.12c and 0.25c, respectively, with c representing the airfoil chord set to 100 mm. Results confirm that tubercles delay stall and improve wing performance in the post-stall regime; moreover, Zhang *et al.* noticed a similarity with vortex generators in the control of boundary layer separation. They observed complex phenomena at the troughs that seem to have a primary role in the stall control; these

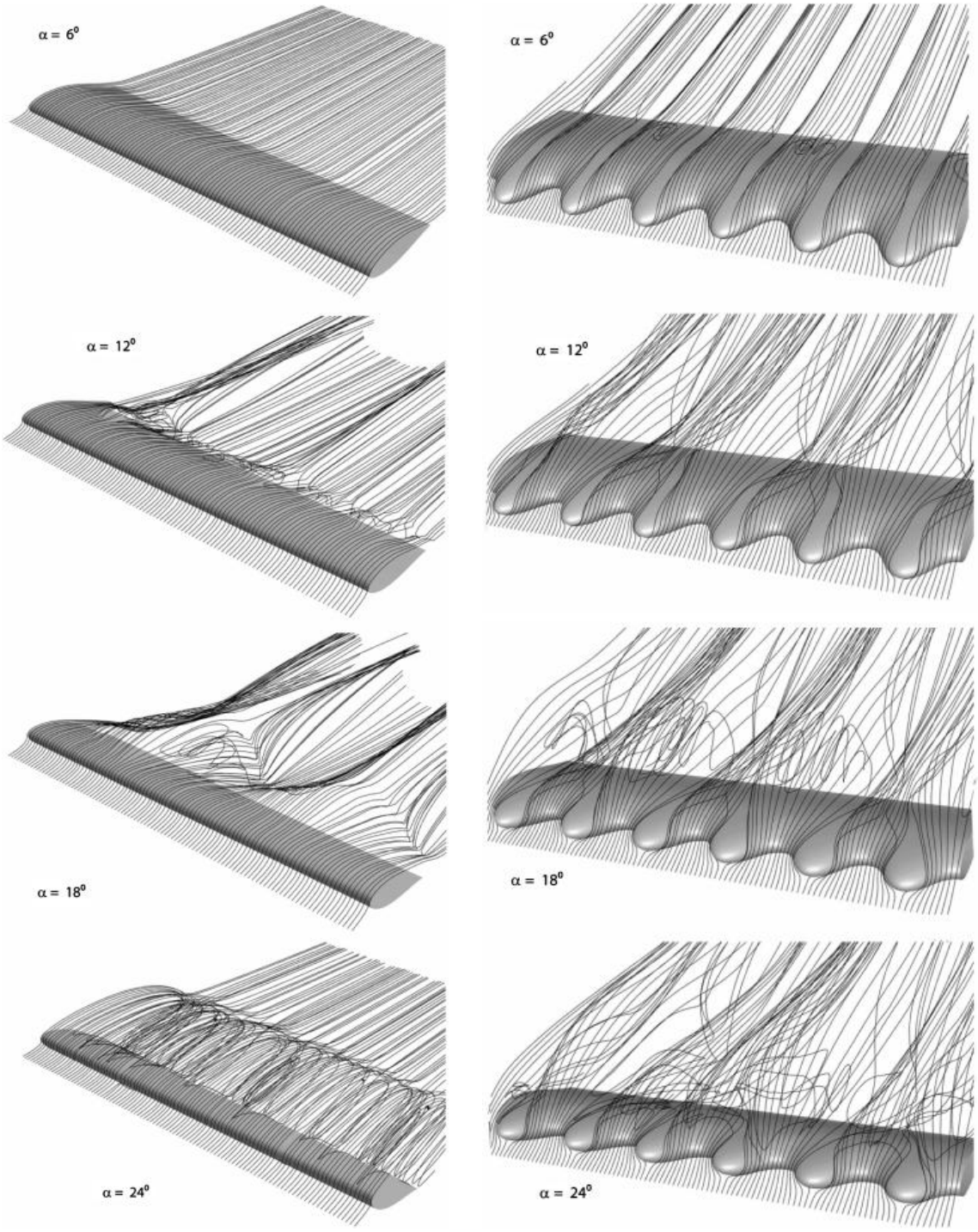

(a) Baseline airfoil (b) Modified airfoil

Figure 2.22: Pathlines over the suction side. [28]

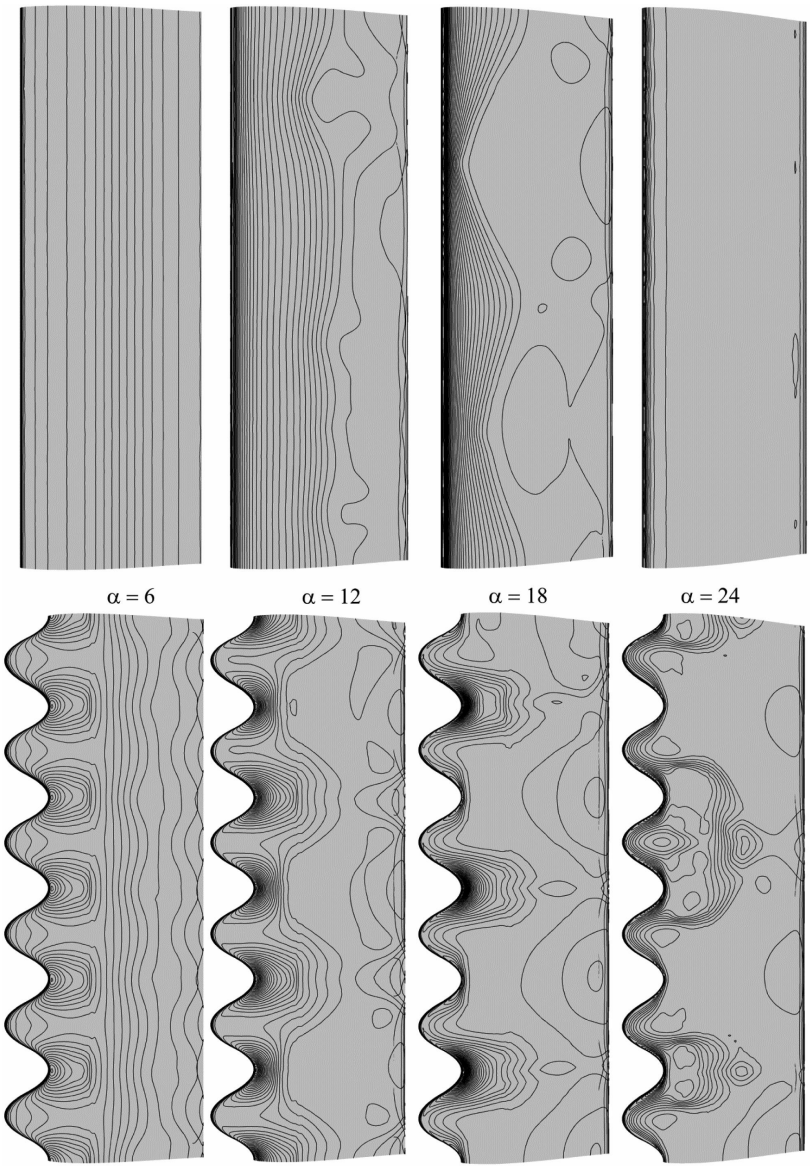

Figure 2.23: Surface pressure distribution of the baseline and modified airfoils. [28]

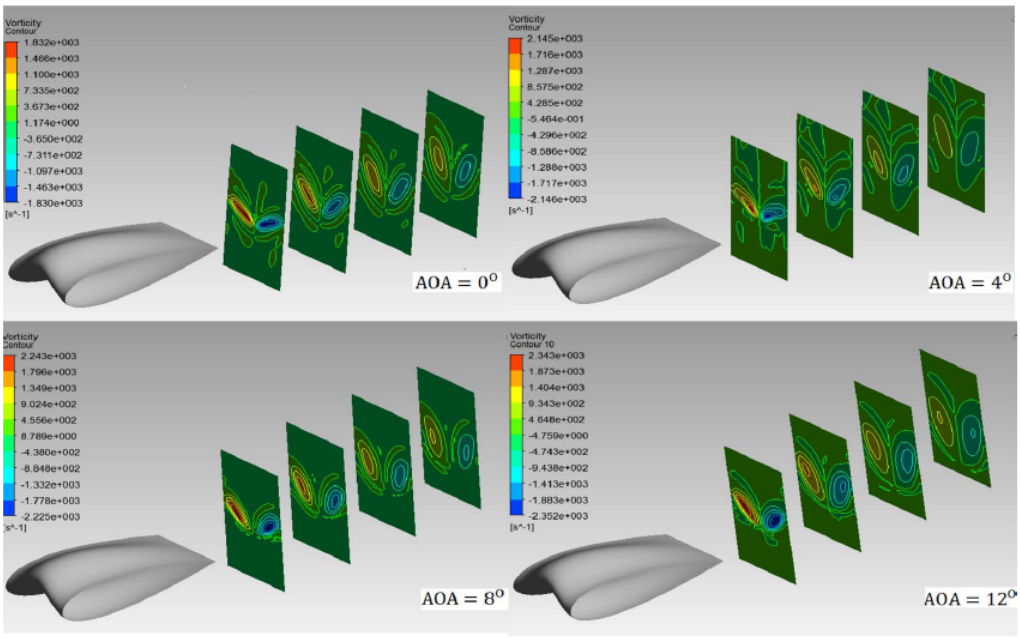

Figure 2.24: Contours of streamwise vorticity on planes located downstream of the trailing edge. [85]

phenomena include streamwise vortices, earlier laminar separation and more natural laminar/turbulence transition, turbulent reattachment, and turbulent boundary layer detachment [104]. In contrast, flow over the peak sections remains attached well over the airfoil suction side due to much stronger streamwise vortices [104].

Rostamzadeh *et al.* [85] tested and simulated four NACA 0021-based airfoils, observing that pairs of counter-rotating vortices are generated in the wake (Fig.2.24). Each vortex is characterized by smaller vortices: one generated from the upper and the other from the lower wing surfaces. As some previous works observed, flow separation happens first behind tubercle troughs rather than peaks; the reason is related to the presence of counter-rotating vortices that push the fluid toward the surface on the peak, reducing the local angle of attack and inhibiting chordwise separation [85]. The contours of the adverse pressure gradient and limiting streamlines are represented in Fig.2.25.

Other numerical simulations of infinite-span wings with tubercles were conducted by Skillen *et al.* [88]. They analyzed the physical mechanism behind performance impro-

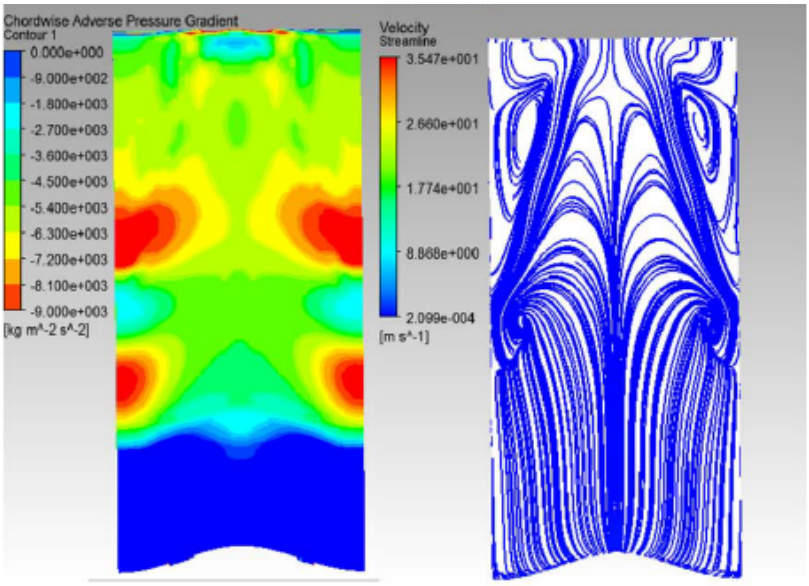

Figure 2.25: Contours of adverse pressure gradient and limiting streamlines on the upper surface. [85]

vement due to leading edge modifications, and they found that initially the oncoming flow is deflected and redirected to the troughs of the tubercles with a strong acceleration (Fig.2.26). Low-inertia near-wall fluid is drawn toward the suction peak, resulting in the formation of secondary flow; in particular, the low-inertia boundary layer is transported away by the secondary flow and it is replaced by higher momentum fluid drawn from above. This implies a re-energization of the boundary layer behind each tubercle peak, leading to a delay in the flow separation, which happens earlier behind the troughs due to strong adverse pressure regions. In Fig.2.27, slices of streamwise vorticity are plotted. Skillen *et al.* also affirm that the strength of the re-energization mechanisms must be a function of the tubercle geometric parameters and Reynolds number. In fact, at a very low Reynolds number, there is not a transition to turbulence, meaning the only active mechanism would be the re-energization by the secondary flow; whereas, at a significantly higher Reynolds number, transition occurs closer to the leading edge and more uniformly across the span [88].

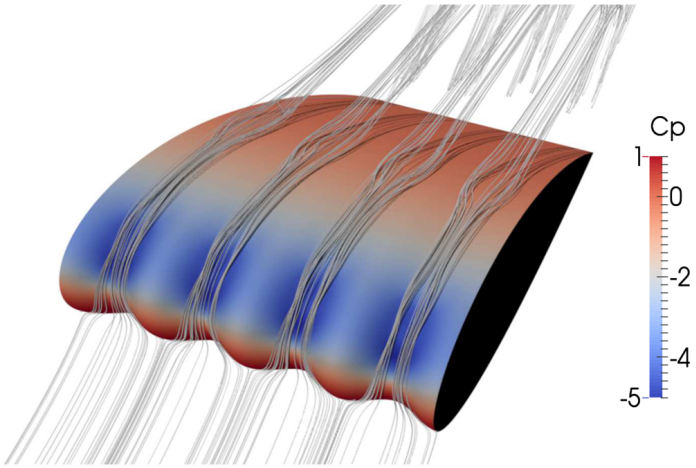

Figure 2.26: Time-averaged streamlines. [88]

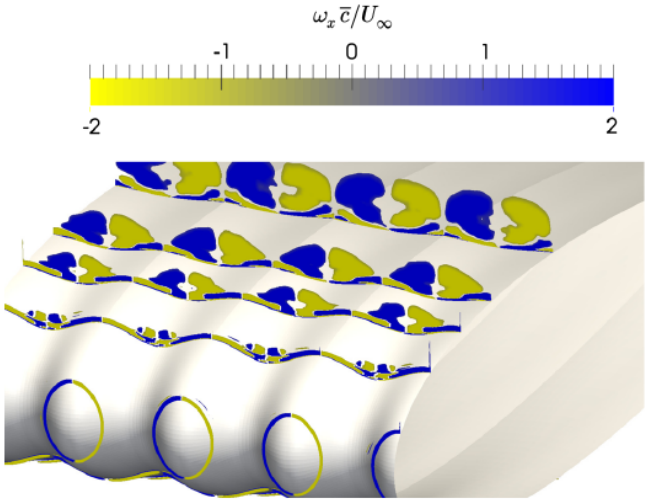

Figure 2.27: Slices colored by time-averaged streamwise vorticity. [88]

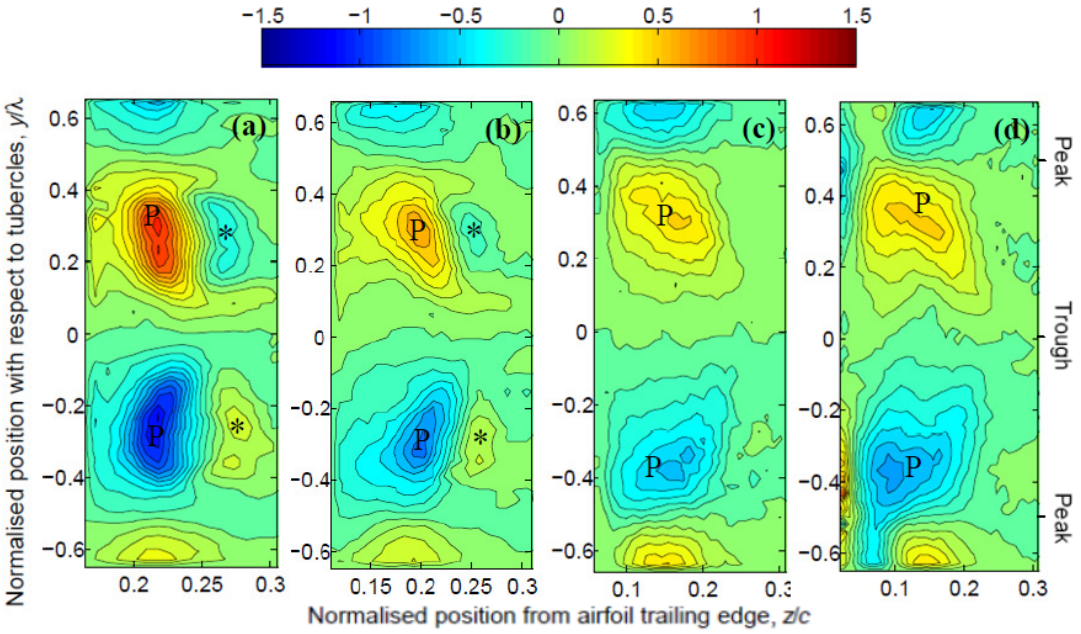

Figure 2.28: Vorticity contours for sequential chordwise planes at (a) $x/c = 0.4$, (b) $x/c = 0.6$, (c) $x/c = 0.8$, (d) $x/c = 1$. [51]

Hansen *et al.* [50, 51] made an experimental and numerical study to investigate the formation and evolution of the streamwise vortices that characterize tubercles on an infinite wing at low Reynolds numbers. They noticed an increase in flow velocity and a larger adverse pressure gradient at the troughs, leading to a boundary layer separation at low angles of attack. These results are consistent with the previous research, where the larger adverse pressure gradient in the troughs was attributed to the short chord length at that spanwise location. From a flow field analysis and as shown in Fig.2.28, vorticity of alternate sign – represented in blue and red – is generated at the troughs, resulting in the formation of counter-rotating vortices; the figure also shows weaker vorticity with movement away from the trailing edge (i.e., moving from Fig.2.28(a) to (d)).

In conclusion, it is well known that tubercles generate counter-rotating vortices, but the interaction between those vortices with the flow over a surface is still under investigation. The common idea is that leading edge modifications work similarly to vortex generators; therefore, in the following section, a description of the passive flow control devices used

in wind turbine application will be presented, and a comparison between vortex generators and tubercles will be done, identifying similarities and differences.

2.5 Passive Flow Control Devices in Wind Turbines

The basic principle of a flow control device is to manipulate a flow field to achieve a particular design objective. In recent decades, many different flow control devices have been developed for aeronautical issues, and most of them have been optimized and adapted to wind turbine applications. Depending on their operating principle, flow control devices can be classified as active [10] or passive. For the purpose of this dissertation, the attention will be focused on passive flow control devices affecting boundary layer and spanwise flow, including:

- Vortex Generators (VGs),
- Microtabs,
- Serrated Trailing Edge,
- Boundary Layer Fences,
- Spoilers.

At the end of this section. a summary of the physical principles, advantages, and disadvantages of the control devices listed above is presented in Table 2.1.

2.5.1 Vortex Generators

A vortex generator is a passive flow control device that modifies the boundary layer, bringing momentum from the outer flow region into the inner one [4]. The main goal is to delay flow separation and increase the maximum lift coefficient by re-energizing the boundary layer. VGs are small triangular or rectangular vanes with a height usually similar to the

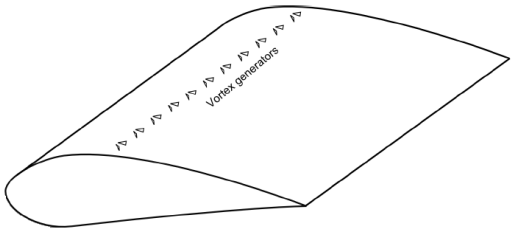

Figure 2.29: Vortex generators over a wing. [4]

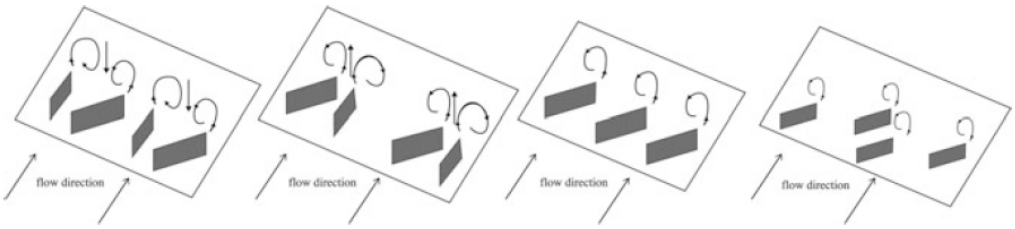

Figure 2.30: VGs generating co-rotating and counter-rotating vortices. [4]

boundary layer thickness; they are inclined with respect to the oncoming flow and placed as close as possible to the leading edge (Fig.2.29). As shown in Fig.2.30, they can generate co-rotating or counter-rotating vortices, depending on their orientation; Godard and Stanislas [40] demonstrated that VGs work most efficiently when they have a triangular shape and create counter-rotating vortices. For wind turbine appplications, vortex generators present a number of advantages such as a small size that allows a large number of them to be distributed along the blade span; easy and low-cost replacement, and the option to add them once the blade is built. On the other hand, VGs increase the drag due to their implantation on the body surface, and great care is also needed when they are integrated into the blades to avoid wind turbine performance deterioration.

2.5.2 Microtabs

Microtabs are small tabs situated close to the trailing edge of an airfoil and perpendicularly to its surface; their length is about $1-2\%$ of the chord corresponding to the boundary layer thickness. The microtabs push the boundary layer (BL) flow away from the airfoil surface, generating a recirculation area behind them, as shown in Fig.2.31. The recirculation zone

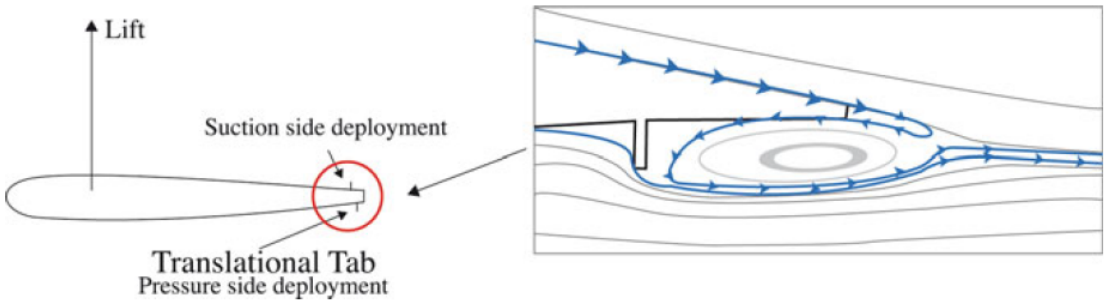

Figure 2.31: Microtabs at the TE of an airfoil. [4]

affects the aerodynamics by shifting the separation point and, therefore, providing changes in the lift. In particular, lift can be improved by deploying the microtab on the pressure side of the airfoil; whereas it can be reduced if the microtab is deployed on the suction side [4]. Yen *et al.* [102] determined the optimal distribution, height, and location of the microtabs by conducting computational fluid dynamics (CFD) simulations and wind tunnel experiments. Their results showed that the best place to situate the tab with respect to the lift and drag is at around 95% of the chord for the lower surface and 90% of the chord for the upper surface, considering a height of 1% of the chord. Microtabs have some appealing features for wind turbine applications, including a small size, simplicity in the design and manufacturing, and the ability to be installed without significant changes in the actual airfoil manifacturing process. However, they have two main issues: first, their height when fully deployed is usually insufficient to affect the boundary layer flow; second, the actuating mechanism causes suction during tab deployment.

2.5.3 Serrated Trailing Edge

Usually, wind turbine blades have sharp or moderately blunt trailing edges from which the wake is shed. The confluence of the flow from pressure and suction sides of the blade is the main source of aerodynamic noise, increased drag, and reduced lift. Therefore, a way to solve these issues consists of a flexible serrated trailing edge (TE), also known as dino tail [4] (Fig.2.32). As an added aerodynamic profile, it presents the advantage of creating a

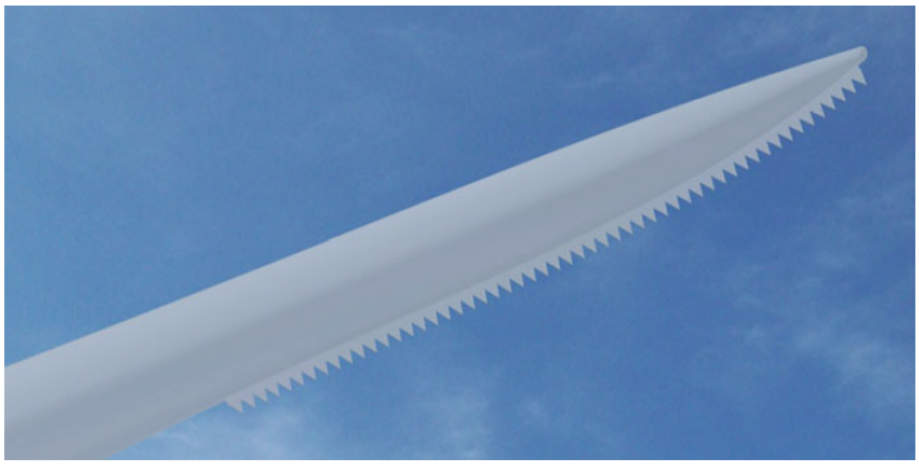

Figure 2.32: Wind turbine blade with serrated trailing edge device. [4]

customized geometry profile for each device according to the operating conditions in which it is located [4].

2.5.4 Boundary Layer Fences

Boundary layer fences are typically small plates wrapping the entire blade surface in the chordwise direction to prevent the creation of spanwise flow (Fig.2.33). On wind turbine blades, the airflow usually spreads in the spanwise direction, leading to the separation of the main flow and, therefore, reducing the blade lift. Boundary layer fences are able to block the spanwise flow, with their effectiveness proportional to their heights [4]; however, increasing the fence height means affecting the aerodynamic characteristics such as lift, and increasing the blade weight. The required height, length, and optimal position of the fence on the blade vary based on different elements, including the distance from the rotor axis of rotation, the rotor width, the most likely speed of the incident flow, etc. Therefore, the best configuration is determined empirically [4].

2.5.5 Spoilers

Wind turbine blades consist of three main regions (Fig.2.34): the root closest to the hub (circular section)(1); the airfoil region furthest away from the hub that generates lift (3);

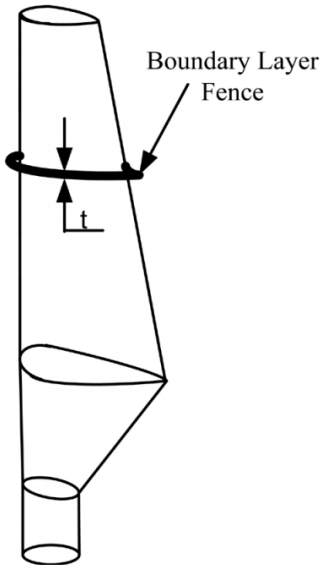

Figure 2.33: Sketch of wind turbine blade with a boundary layer fence. [4]

and a transition region between the two (2). The root and transition regions do not help in the energy production and they even decrease it due to drag. These sections usually work in stall situations, especially at high wind speeds; therefore, spoilers are used and placed in those regions (Fig.2.34) to increase lift during stall and to improve turbine power generation. The potential performance improvement by applying spoilers reaches $1-1.5\%$ of the annual energy compared to the same wind turbine without those control mechanisms. This compensates for the high manufacturing costs for blades with spoilers; however, since wind turbine blades must work with higher angles of incidence, this device has strong negative aerodynamic effects [4].

2.5.6 Tubercles vs Vortex Generators

Most researchers suggest a similarity between tubercles and vortex generators; however, since the amplitude and wavelength of tubercles are larger than the boundary layer thickness, van Nierop [94] proposed a different theory: tubercles change the pressure distribution across the surface, delaying boundary layer separation and resulting in a more gradual stall. This idea was criticized by Zhu [107], who pointed out that in van Nierop's

Table 2.1: Summary of passive flow control devices in wind turbine blades.

Device	Working Principle	Pros & Cons
VGs	counter-rotating vortices	✔ small dimension ✔ cost ✔ replacement ✖ drag ✖ blade integration
Microtabs	recirculation in BL	✔ small dimension ✔ simplicity ✖ insufficient height ✖ actuation
Serrated TE	TE customized geometry	✔ noise ✔ drag ✖ manufacturing ✖ design complexity
BL Fences	block of spanwise flow	✔ lift ✔ stall strength reduction ✖ aerodynamics ✖ weight
Spoilers	transition region geometry modification	✔ lift ✔ power ✖ aerodynamics ✖ manufacturing costs

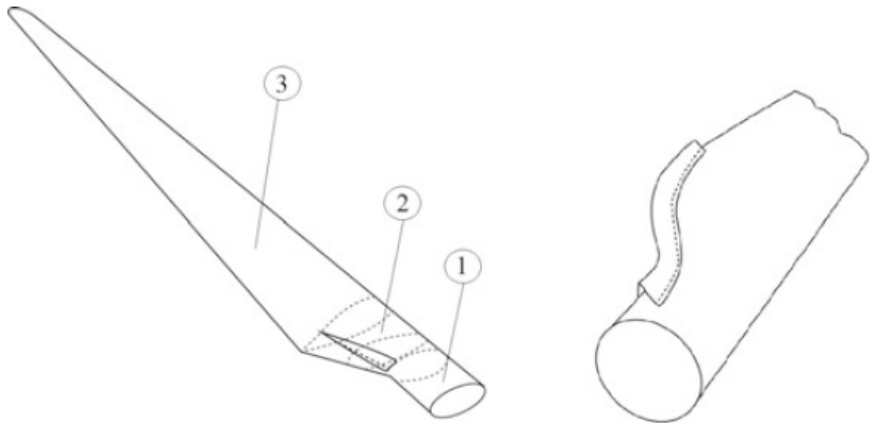

Figure 2.34: Regions of a wind tubine blade with a spoiler. [4]

studies, he neglected tip effects and applied the potential flow theory of an inviscid and irrotational flow to a rotational problem [1]. Stein and Murray [92] do not completely agree with the comparison between tubercles and VGs; in fact, they noticed that vortices generated by tubercles seem to prevent stall progression rather than re-energize the boundary layer, meaning they can be considered more similar to wing fences. Nevertheless, since it is well known that tubercles generate counter-rotating vortices and even though the exact working mechanism is yet to be determined, it is a common idea to consider them similar to vortex generators. However, from a manufacturing point of view, tubercles seem to be more complex to implement as compared to VGs [82]. Recently, as a result of new manufacturing techniques, it is possible to achieve a complex design like leading edge sinusoidal modifications with high quality and relatively low cost by attaching leading edge protuberances to an existing surface (i.e., blade or wing). This method permits also allows for easy replacement of tubercles in the case of wear or damage. A big advantage that tubercles have compared to vortex generators is that they do not increase drag. As already presented in Sec.2.5.1, a noteworthy problem with using VGs is their effect on drag due to their implantation on the body surface; tubercles instead increase lift without increasing drag. Table 2.2 provides a schematic summary of similarities and differences between tubercles and vortex generators.

Table 2.2: Summary of similarities and differences between tubercles and vortex generators.

Device	Working Principle	Pros & Cons
Tubercles	counter-rotating vortices	✔ lift increase ✔ stall delay ✖ manufacturing
VGs	counter-rotating vortices	✔ lift increase ✔ stall delay ✖ drag increase

2.6 Bio-inspired Engineering Problem

Many times, human technologies have been inspired by morphological features of animals, or nature in general [11, 22, 47]; the study of structures and functions of biological systems in design engineering systems is known as biomimetics [1]. A detailed review of technological applications of various biological systems in relation to engineering has been compiled by Bar-Cohen [1, 8]. Many aerodynamic ideas were inspired by the bird's flight, especially owls and seagulls [1, 23, 25, 41, 57, 62, 69, 70, 95, 100] (Fig.2.35,Fig.2.36), and by marine animals, e.g., aircraft skin similar to that of sailfish and swordfish, or riblets inspired by sharks to reduce the skin friction drag [16] (Fig.2.37). The succesful integration of biomimetics into mechanical systems has been a challenge, but recent technological advancements in material science and engineering have made biomimetics more realistic [21, 32, 34].

In this work, leading edge tubercles on humpback whale flippers are applied to wind turbine blades as a flow control mechanism to achieve performance improvements. Since this is a bio-inspired engineering problem, it is important to highlight analogies and differences between the humpback whale flipper and wind turbine blade applications. Both work in a low Reynolds number range ($10^4 - 10^6$): for humpback whales the Reynolds

Figure 2.35: Seagull's flight. [41]

Figure 2.36: Flight configurations inspired by seagull's flight. [41]

Figure 2.37: Examples of biomimetics engineering. [2]

number is between $2 \cdot 10^5$ and $3 \cdot 10^6$ [51, 80], while for the NREL Phase VI wind turbine blade (i.e., the baseline model in the present study), it goes from $5 \cdot 10^5$ at the root to $1 \cdot 10^6$ at the tip, considering a wind speed of 10 $\mathrm{m/s}$ (Fig.2.38). For both flippers and blades, the flow at these Reynolds numbers shows some transition behaviors with abrupt separation of laminar flow near the leading edge. Geometrically, flippers and wind turbine blades have some similarities. Indeed, flipper cross sections can be represented by thick airfoils commonly used for wind turbine applications [51]. Even though some analogies have been observed, flippers and blades are completely different in terms of flow characteristics for two main reasons: first, flippers work with water, whereas the blades work with the air, which means different flow density, temperature, etc.; the second reason is related to how flow approaches each body surface. In other words, wind turbine blades rotates and the approaching flow is characterized by a relative velocity due to the rotational speed of the rotor; whereas, whale flippers can have several different movements (i.e. protraction, retraction, abduction, adduction, lateral and medial rotation [30]) that more often occur

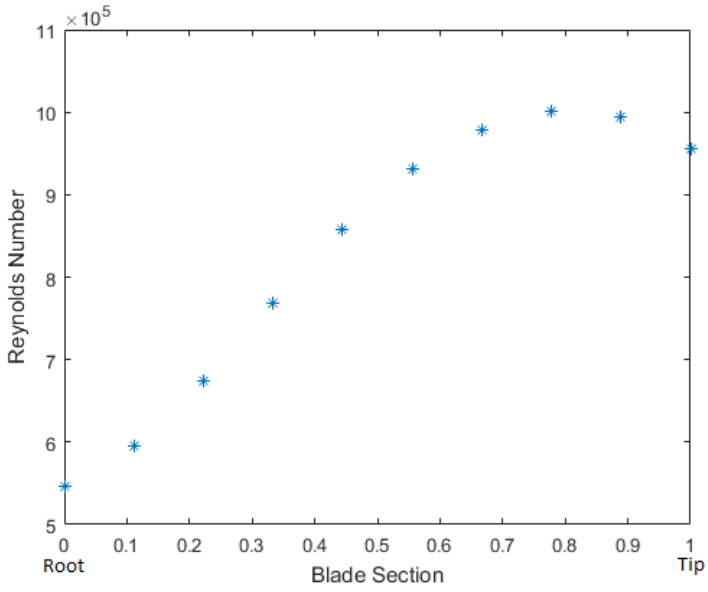

Figure 2.38: Reynolds number along the NREL Phase VI wind turbine blade span at wind speed of 10 $\mathrm{m/s}$.

as combitations [30]. Therefore, considering all these possible configurations, the flow condition around the whale flipper is more variable and difficult to predict.

Analogies and differences between wind turbine blades and flippers will be taken into consideration in the analysis of the problem developed in this dissertation.

2.7 Summary

Summarizing the results from previous research on the aerodynamic analysis of tubercles applied to wings and wind turbines, it is possible to conclude that leading edge modifications permit:

- flow separation delay,
- lift performance improvement in the post-stall regime,
- increase of operative ranges of angle of attack and wind speed,

- increase of power generated at high wind speeds where usually blades stall and wind turbines become inefficient.

From an analysis of the previous studies and considering only an aerodynamic point of view, it is possible to identify the following missing aspects or research gaps:

1. a rigorous study about the effects of tubercle geometric parameters (i.e., amplitude and wavelength) on wind turbine performance;
2. a study about the effects of tubercle position along the blade span;
3. a combined study of amplitude, wavelength, and tubercle position effects on wind turbine performance; and
4. insights into how placing tubercles on the leading edge of wind turbine blades to achieve performance enhancement.

Based on these four points, it is possible to present the problem formulation of this dissertation, and the final objectives of the thesis work.

CHAPTER 3

PROBLEM FORMULATION

In Chapter 2, the advantages of tubercles on wind turbine applications have been examined. Based on those findings and on the research gaps listed, it is possible to present the objective of this work which is focused on the analysis of aerodynamic effects of tubercles applied to wind turbine blades. In the following sections, research questions and hypotheses necessary to achieve the main goal of the present study are detailed.

3.1 Research Objectives

Main Research Objective
Give insights into the application of tubercles on the leading edge of wind turbine blades such that performance enhancement can be achieved.

To achieve this objective, the research work is divided into three phases:

1. an analysis of the effects of tubercle amplitude and wavelength on wind turbine performance;
2. an analysis of the effects of only the location of tubercles along the blade span; and
3. a combined study on the effects of amplitude, wavelength, and tubercle location.

Based on these three phases, the corresponding three sub-objectives have been identified:

1. analyze the effects of tubercle amplitude and wavelength on wind turbine performance;
2. analyze the influence of tubercle spanwise location on wind turbine performance; and

3. analyze the effects of both the tubercle geometric parameters (i.e., amplitude and wavelength) and the spanwise location on wind turbine performance.

In the following sections, research questions and hypotheses are formulated that help in the achievement of the objectives listed above.

3.2 Research Questions and Hypotheses

As presented in Chapter 1, wind turbines show several problems and performance losses due to the variable nature of the wind; for this reason, recent research has focused on the development of new control devices that are able to solve most of these wind power generation issues. The most promising solution seems to exist in the application of tubercles on the leading edge of wind turbine blades. Since only a few studies have been conducted on this topic, some important aspects about the actual implementation of this solution are missing. Based on the main objective of this work, the primary research question is:

Main Research Question
What are the main aerodynamic effects of tubercles applied to wind turbine blades such that it is possible to achieve performance enhancement?

Previous researchers tested tubercles applied to wind turbine blades by choosing random values of amplitude and wavelength, and they did not define any guidelines on how to select those geometric parameters to improve wind power production. In this dissertation, a more in-depth systematic study will be conducted with a particular attention on the NREL Phase VI wind turbine performance.

3.2.1 Amplitude and Wavelength

According to the first sub-objective presented in Sec.3.1, it is necessary to understand how tubercle geometric parameters (i.e., amplitude and wavelength) affect blade aerodynamics. Previous studies [106] showed that tubercle amplitude and wavelength play a large role

in the aerodynamic performance of a wing or a blade, but neither study defined a way of choosing those parameters such that performance enhancement can be achieved. Therefore, the first research question related to the first sub-objective is:

First Research Question
How do tubercle amplitude and wavelength affect wind turbine performance?

Past research does not provide an answer to this question because some studies showed positive results when small values of amplitude and wavelength were used [49, 51, 59], while others noticed the opposite trend [29, 98]. Moreover, in all the past works, tubercle geometric parameters have been chosen randomly without defining specific rules for their selection. Therefore, since a systematic study on the effects of amplitude and wavelength on wind turbine performance is missing, the hypothesis linked to the first research question could be:

First Hypothesis
Specific values – or at least ranges – of amplitude and wavelength exist such that wind turbine performance improvement can be achieved.

3.2.2 Spanwise Location

Another important element to consider in tubercle effects on wind turbine performance is spanwise location. As described in Chapter 2, tubercles are not evenly distributed along the humpback whale's flipper span; they start at around 33% of the span and are more concentrated close to the tip. Thus, it is of interest to study how the spanwise location affects wind turbine performance, and what happens when these effects are coupled with those given by the geometric parameters (i.e., amplitude and wavelength). For these purposes, two other research questions and the corresponding hypoteses are formulated:

Second Research Question
How does tubercle spanwise location affect wind turbine performance?

Wind turbine blades can be divided into three main regions contributing differently to power generation (Sec.2.5.5); in particular, the second half of the blade (from midspan to the tip) is the most influential in the energy production, therefore:

Second Hypothesis

Tubercle spanwise location will have relevant effects in wind turbine power improvement; in particular, tubercles located from midspan to the tip will have more positive effects since the second half of the blade is the most influential in the energy production.

Third Research Question

What happens to turbine performance if amplitude, wavelength, and spanwise location are considered as three design variables?

Third Hypothesis

Considering amplitude, wavelength, and spanwise location as three design variables, it will be possible to identify a limited region in the design space where performance improvements can be achieved.

3.2.3 Hypothesis Verification

In the following chapter, an in-depth analysis of the methodology used to verify the hypotheses presented above and to achieve the objectives listed in Sec.3.1 is developed. In particular, the work is divived into three phases: first, amplitude and wavelength effects on the blade aerodynamic performance are analyzed by generating a two-dimensional design of experiments (DoE); then, only the spanwise location of tubercles is considered as single design variable to highlight the effects of the position of tubercles along the blade span; finally, three design variables (amplitude, wavelength, and tubercle spanwise location) are considered for the generation of a three-dimensional DoE. Figure 3.1 shows the three hypotheses formulated to help in the achievement of the main objective of this work, and the corresponding procedure used to verify each one of those.

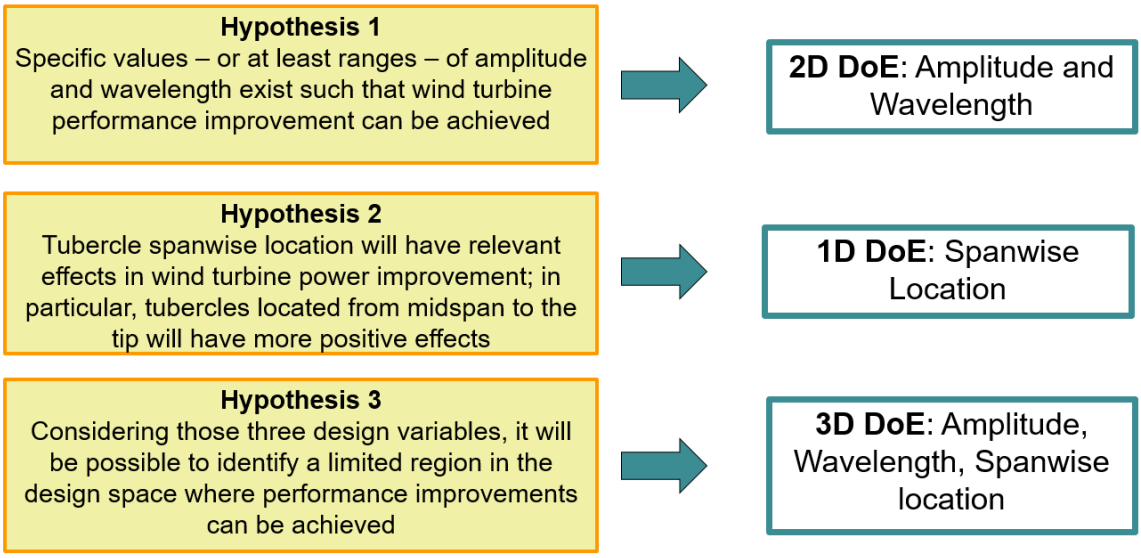

Figure 3.1: Hypotheses verification scheme.

CHAPTER 4

METHODOLOGY

4.1 Methodology Formulation

The main objective of this research is to give insights into the application of tubercles on the leading edge of wind turbine blades to achieve performance improvements. As described in Sec.3.2.3, the work is divided into three phases:

1. variation of tubercle amplitude and wavelength to analyze aerodynamic effects and performance improvements in wind turbine performance;

2. analysis of the only tubercle position along the blade span to highlight its possible influence in wind turbine performance;

3. variation of amplitude, wavelength, and tubercle spanwise location to evaluate aerodynamic effects and performance improvements.

For each of the above phase, the same methodology (Fig.4.1) has been implemented consisting in the following steps:

1. blade parametrization,

2. design variable selection,

3. design of experiments (DoE),

4. computational fluid dynamics (CFD) analysis,

5. performance analysis,

6. surrogate modeling, and

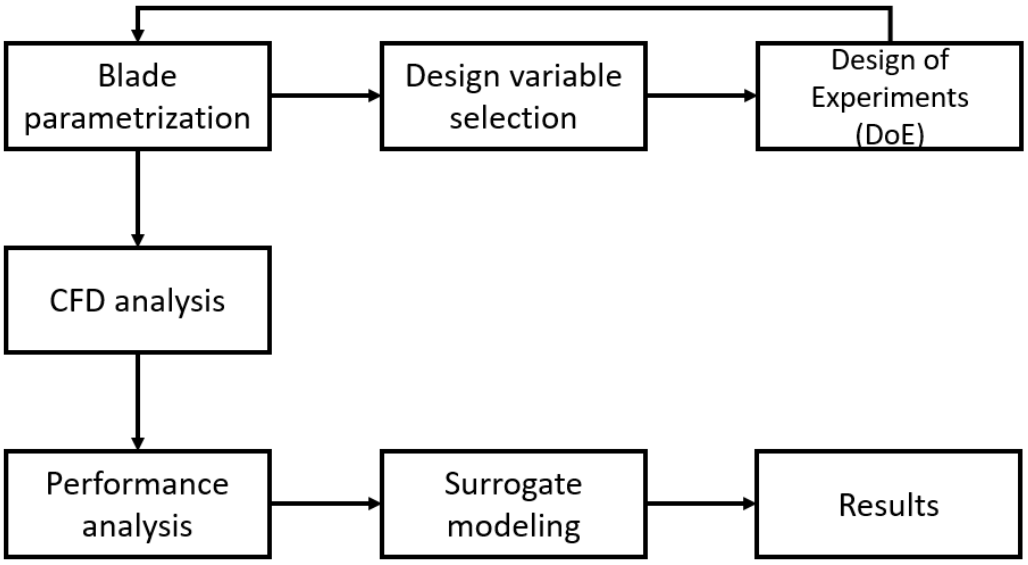

Figure 4.1: Methodology.

7. result analysis.

The first step of the method consists in the geometry parametrization of the baseline wind turbine blade and the blades with tubercles. Once the baseline model has been chosen, the tubercles are generated by scaling the airfoil following a sinusoidal path and keeping the trailing edge line fixed [51], as shown in Fig.4.2. Each airfoil chord varies by a quantity Δc:

$$\Delta c = A \sin\left(\frac{2\pi}{\lambda} z\right) \tag{4.1}$$

where A is the amplitude of tubercles, λ is the wavelength, and z is the location of the section along the blade span (Fig.4.3). The new chord (c) at each airfoil section is given by summing the original value of the chord at that section ($\bar{c}$) with the Δc previously calculated:

$$c = \bar{c} + \Delta c \tag{4.2}$$

From the blade parametrization, it is possible to choose the blade parameters that become design variables in the design of experiments generation.

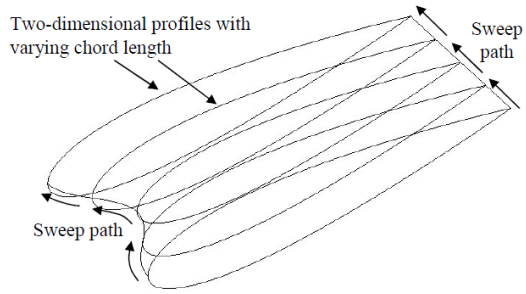

Figure 4.2: Tubercle representation. [51]

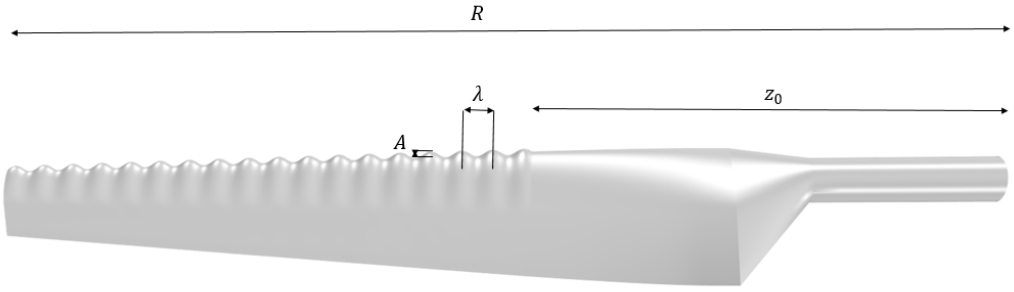

Figure 4.3: Representation of blade parameters.

A systematic analysis of tubercle effects on wind turbine performance is conducted in this work; therefore, a design of experiments is used for the generation of tubercle configurations to test. Depending on the number of the design variables involved, it is possible to identify and choose the DoE scheme more suitable for the problem.

Although advanced sample strategies are available in the literature [20, 26, 38, 39, 71], it has been decided to consider standard methods, including Latin hypercube sampling and full factorial design, due to the low dimensionality (i.e., maximum of three dimensions) of the problems faced in the present work. The Latin hypercube (Fig.4.4) permits a rich sampling of the interior of the design space with high accuracy; but on the other hand, it does not cover well the edges of the design space. For this reason, it is necessary to consider also a full factorial DoE (Fig.4.4), that provides the accuracy on the edges of the design space missing in the Latin hypercube design.

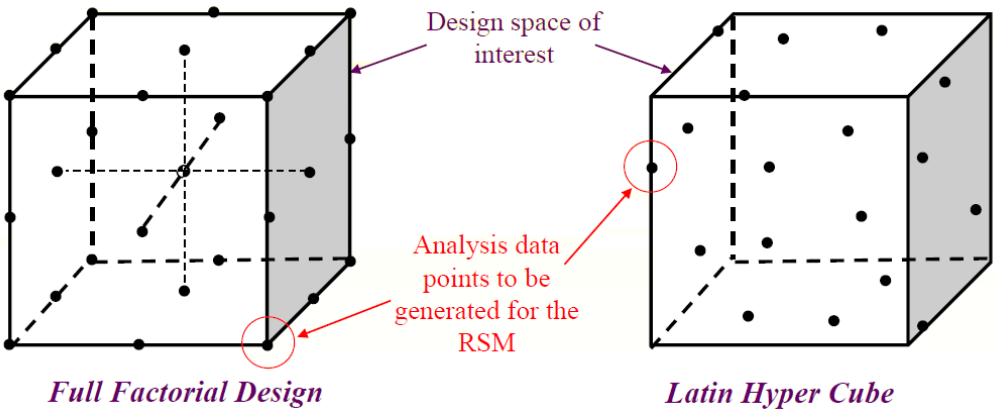

Figure 4.4: Full factorial and Latin hypercube DoEs.

The regular blade and the blades with tubercles resulting from the DoE are tested in a computational fluid dynamics software. In particular, a three-dimensional CFD analysis is performed by using Star-CCM+© that embodies both mesh generation and CFD simulation in a single code. This aspect reduces the risk of format incompatibility when handling the mesh file, resulting in a faster and more efficient procedure.

The CFD results of the tubercle configurations are then analyzed and compared with those of the baseline wind turbine blade. To better visualize the trends of the results, a surrogate model is generated considering a polynomial response surface equation of second or third order depending on the number of design variables involved. The general formulation of the second order equation is the following:

$$y = \beta_0 + \sum_{i=1}^{k} \beta_i x_i + \sum_{i=1}^{k} \beta_{ii} {x_i}^2 + \sum_{i=1}^{k-1} \sum_{j=i+1}^{k} \beta_{ij} x_i x_j + \epsilon \tag{4.3}$$

and the third order equation is:

$$y = \beta_0 + \sum_{i=1}^{k} \beta_i x_i + \sum_{i=1}^{k} \beta_{ii} {x_i}^2 + \sum_{i=1}^{k-1} \sum_{j=i+1}^{k} \beta_{ij} x_i x_j + \sum_{i=1}^{k} \gamma_i {x_i}^3 + \sum_{i=1}^{k} \sum_{j=1, j\neq 1}^{k} \gamma_{ij} {x_i}^3 x_j + \epsilon \tag{4.4}$$

where y is the response, β and γ are regression coefficients, $x_{i,j}$ are the independent variables, and ϵ is the error associated with neglecting higher order effects, missing regressors,

and inherent randomness of the response. The surrogate model is trained by using the CFD results, and the goodness of fit is evaluated in terms of R^2 and normalized root mean square error (NRMSE). R^2 is defined as follows:

$$R^2 = 1 - \frac{SS_E}{SS_T} \tag{4.5}$$

where SS_E is the sum of the squares of the error and SS_T is the total sum of squares defined as:

$$SS_E = \sum_{i=1}^{n} (y - \tilde{y})^2 \tag{4.6}$$

$$SS_T = \sum_{i=1}^{n} (y - \bar{y})^2 \tag{4.7}$$

with y representing the actual value of the function, $\tilde{y}$ the predicted value, and $\bar{y}$ the mean of the actual values. The root mean square error (RMSE) is the square root of the mean square error, which is $(y - \tilde{y})^2$. RMSE is then normalized in the following way:

$$\text{NRMSE} = \frac{\text{RMSE}}{max(y_{\text{train}}) - min(y_{\text{train}})} \tag{4.8}$$

where $max(y_{\text{train}})$ and $min(y_{\text{train}})$ are the maximum and minimum values of the response for the training cases, respectively. The surrogate model generated must have an R^2 close to 1 and low values of NRMSE to be considered a good model. The resulting response is visualized in contour plots that better capture the trend of the results in the design space; from these plots, it will be possible to better analyze the performance effects of tubercles on the leading edge of the NREL Phase VI wind turbine blade.

In the next section, the methodology described above is presented with more details referring to the specific problem analyzed in this research work.

4.2 Methodology Implementation

The methodology described in the previous section is now implemented to the specific test case used in this work to achieve the final objective: get insights into the application of tubercles on the leading edge of wind turbine blades such that performance enhancement can be achieved.

4.2.1 Blade Geometry and Design Variables

The baseline geometry considered is the NREL Phase VI wind turbine blade. The main reason for choosing such a simplified wind turbine rather than a modern multi-megawatt machine is related to the availability of several experimental data coming from wind tunnel tests conducted at the NASA Ames Research Center [48]. Moreover, a turbine with fixed pitch and constant rotational speed is considered because once it has been demonstrated that tubercles are able to increase the wind speed operative range for such a simplified turbine, it is reasonable to suppose that they can work even better when pitch control and variable rotational speed are introduced.

The NREL Phase VI wind turbine is a two-blade machine of 10 m diameter with a rotational speed of 7.54 $\mathrm{rad/s}$. The blades are twisted and tapered with a cylindrical section at the root and an S809 airfoil section from 25% of the span to the tip (Fig.4.5). The yaw angle is fixed at 0°, and the blades are mounted to have a pitch angle of 3°. A fixed pitch rotor is considered in this study to keep the overall cost of the system low. Tubercles are applied to the leading edge of the baseline blade as described in Sec.4.1.

Once the blade parametrization is completed, it is necessary to choose the design variables useful for the DoE generation. For simplicity, non-dimensional values of amplitude ($\bar{A}$), wavelength ($\bar{\lambda}$), and starting spanwise location ($\bar{z_0}$) are considered and defined as follows:

$$\bar{A} = \frac{A}{c_0} \tag{4.9}$$

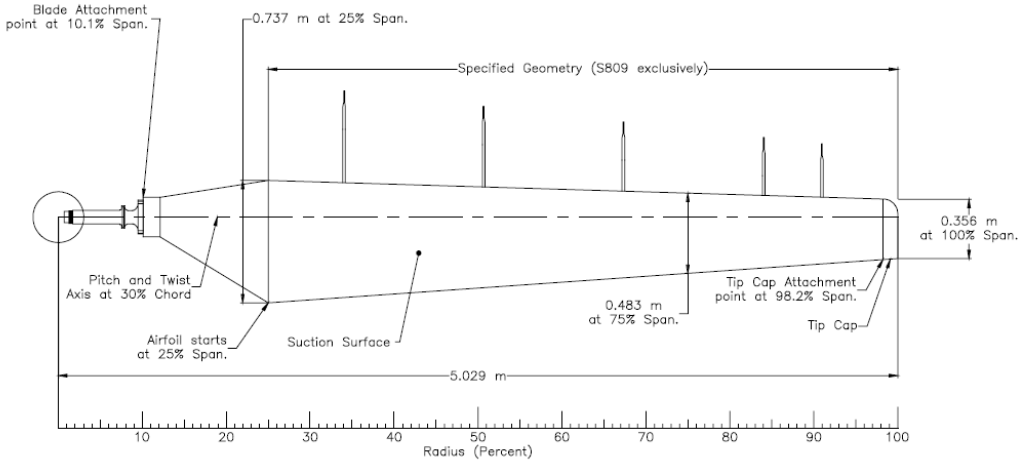

(a) Blade drawing [48]

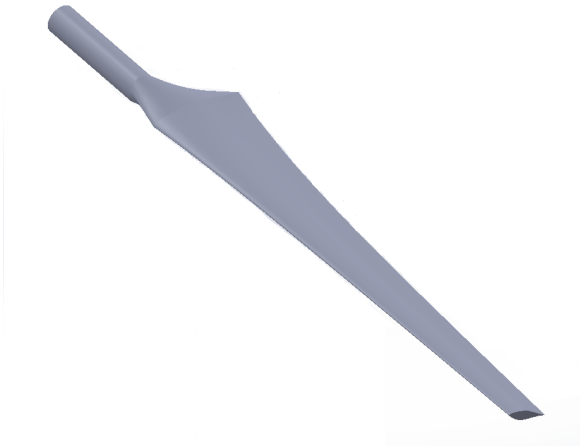

(b) CAD model

Figure 4.5: NREL Phase VI wind turbine blade.

$$\bar{\lambda} = \frac{\lambda}{R} \tag{4.10}$$

$$\bar{z_0} = \frac{z_0}{R} \tag{4.11}$$

where c_0 is the chord length at the blade root, R is the length of the blade, and z_0 defines the starting location along the span where tubercles are placed. Noticeably, amplitude and wavelength do not vary as a function of z, even though it is reasonable to consider their variation since the flow over a wind turbine blade changes along the span; however, in this preliminary study, it has been decided to analyze the effects of constant values of A and λ along the span. A representation of the three design variables (amplitude, wavelength, and starting spanwise location) is provided in Fig.4.3.

Since it is necessary to conduct a validation of the results, the regular NREL Phase VI blade is generated first. Then, several blades with tubercles are created corresponding to the different tubercle configurations resulting from the design of experiments. Two examples of the NREL Phase VI wind turbine blade with tubercles are represented in Fig.4.6: a full-blade tubercle configuration in Fig.4.6(a) where tubercles cover the entire blade span, and a blade with tubercles starting at z_0 in Fig.4.6(b).

4.2.2 Design of Experiments

As presented in Chapter 3, the work is divided into three phases according to the three sub-objectives to achieve, and the corresponding three hypotheses to validate, as summarized in Fig.4.7. First, amplitude and wavelength effects are analyzed by generating a two-dimensional DoE; then, only tubercle spanwise location is considered as single design variable (one-dimensional DoE); and finally, the effects of amplitude, wavelength, and tubercle spanwise location are analyzed by generating a three-dimensional DoE.

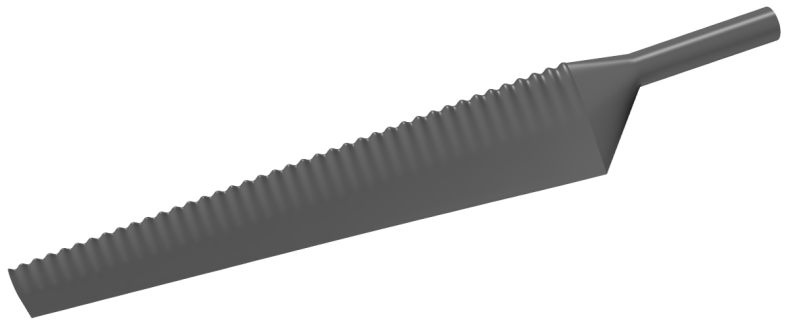

(a)

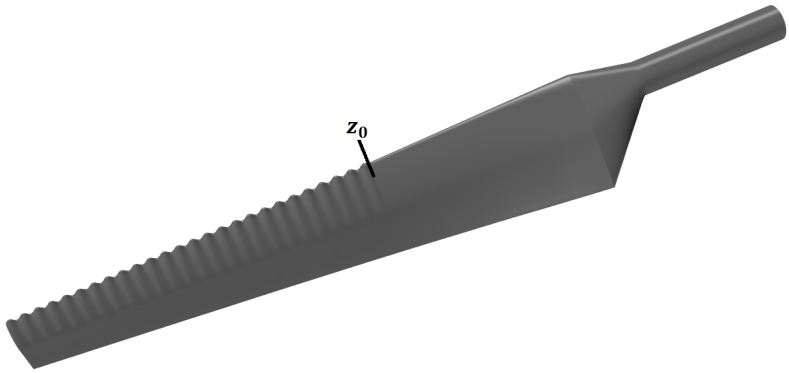

(b)

Figure 4.6: NREL Phase VI blade with tubercles.

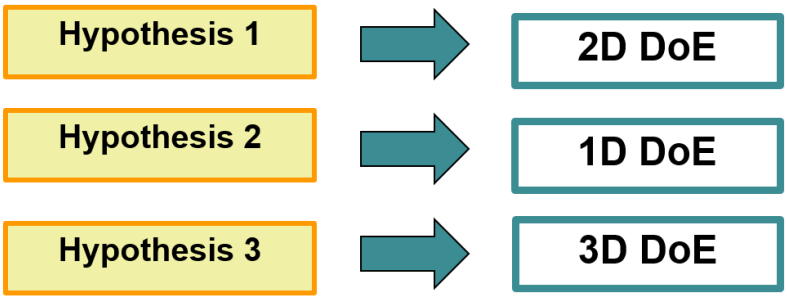

Figure 4.7: Hypotheses and verification methods.

Table 4.1: Two design variable DoE ranges.

Design Variable	Range
$\bar{A}$	$[0.01 - 0.05]$
$\bar{\lambda}$	$[0.016 - 0.075]$

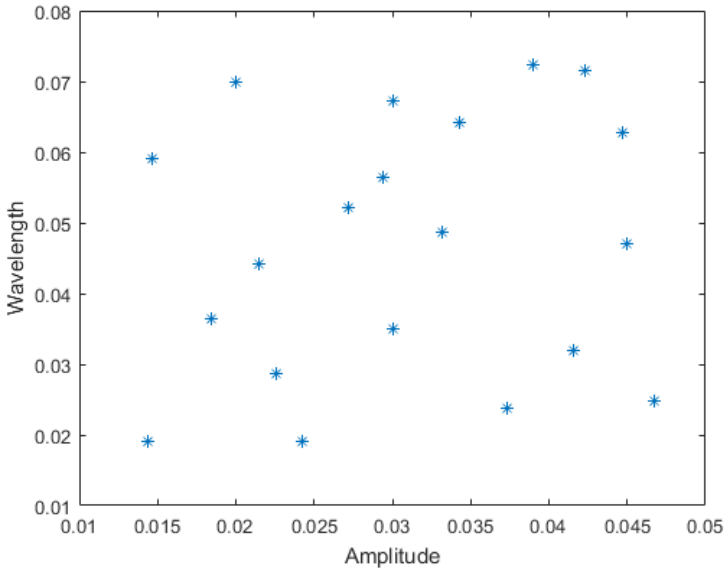

Figure 4.8: Two design variable DoE.

The first part of the study analyzes the effects of non-dimensional amplitude and non-dimensional wavelength (Sec.4.2.1) on wind turbine performance. These two geometric parameters are considered design variables for the generation of a two-dimensional Latin hypercube DoE with 10 points per dimension. Design variable ranges are chosen to generate reasonable geometries, and they are listed in Table 4.1. The resulting design space is illustrated in Fig.4.8, where each dot represents one of the 20 tubercle configurations generated.

In the second part of the work, amplitude and wavelength are fixed and the non-dimensional spanwise location ($\bar{z}_0$) (Sec.4.2.1) is considered as a single design variable. Six tubercle configurations are generated by dividing the regular NREL blade into six sections, corresponding to six values of $\bar{z}_0$: 0.4, 0.51, 0.62, 0.74, 0.85, and 0.95 (Fig.4.9).

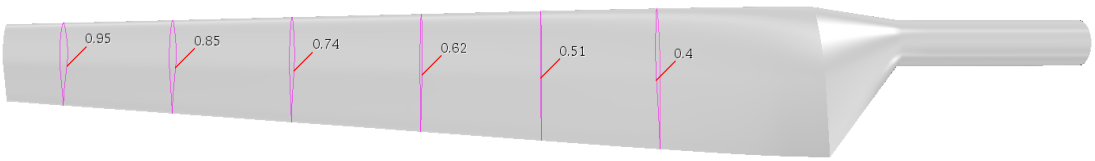

Figure 4.9: NREL blade sections corresponding to the six values of $\bar{z}_0$.

Table 4.2: Three design variable DoE ranges.

Design Variable	Range
$\bar{A}$	$[0.01 - 0.05]$
$\bar{\lambda}$	$[0.016 - 0.075]$
N_{peaks}	$[1 - N_{\text{peaksMax}}]$

The last phase of the study considers three design variables: non-dimensional amplitude, non-dimensional wavelength, and the number of tubercle peaks (N_{peaks}), which substitutes the non-dimensional spanwise location $\bar{z}_0$. The ranges for non-dimensional amplitude and wavelength are the same as those used before (see Table 4.1); whereas, the N_{peaks} is bounded between 1 and the maximum number of peaks that can cover the whole blade span (N_{peaksMax}). Ranges for the three design variables described above are listed in Table 4.2. N_{peaksMax} is a function of the non-dimensional wavelength ($\bar{\lambda}$), found by calculating the portion of blade covered by tubercles (z_{tub}) and the resulting z_0 (Fig.4.10), which are:

$$z_{\text{tub}} = [N_{\text{peaks}} + (N_{\text{peaks}} - 1)] \frac{\lambda}{2} \tag{4.12}$$

$$z_0 = R - z_{\text{tub}} \tag{4.13}$$

where $N_{\text{peaks}} - 1$ is the number of tubercle troughs, and R is the length of the blade. Therefore, the maximum number of tubercle peaks can be found by setting z_{tub} equal to the blade

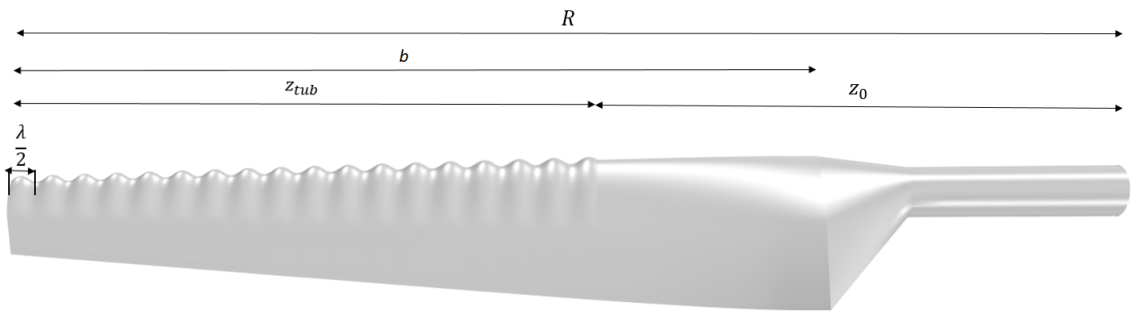

Figure 4.10: Representation of blade parameters.

span b, resulting in the following expression:

$$N_{\text{peaksMax}} = \left[\frac{b}{\frac{\lambda}{2}} + 1 \right] \frac{1}{2} \tag{4.14}$$

Thirty cases are first generated by a Latin hypercube DoE. Since this type of DoE resulted in an unsatisfying coverage of the design space close to the edges (Fig.4.11(a)), a full factorial with three points per dimension is added to the Latin hypercube. In Fig.4.11, Latin hypercube, full factorial, and the summation of the two DoEs are illustrated. For simplicity, results are shown considering a non-dimensional value of z_{tub} that corresponds to the percentage of blade span covered by tubercles:

$$\bar{z}_{\text{tub}} = \frac{z_{\text{tub}}}{b} \tag{4.15}$$

All the tubercle configurations generated by the DoEs have been tested by using three-dimensional CFD simulations.

4.2.3 Numerical Method

Several previous studies simulated both the baseline NREL Phase VI wind turbine blade [19, 65, 67, 68, 87, 89] and the same blade with geometry modifications [18]. In the present work, each tubercle configuration and the baseline NREL Phase VI blade are simulated at

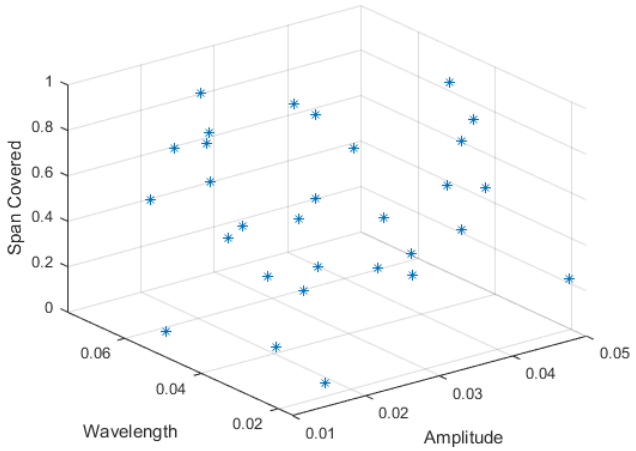

(a) Latin hypercube

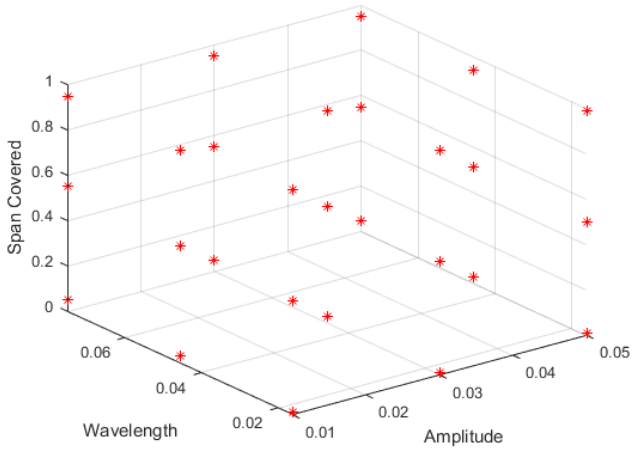

(b) Full factorial

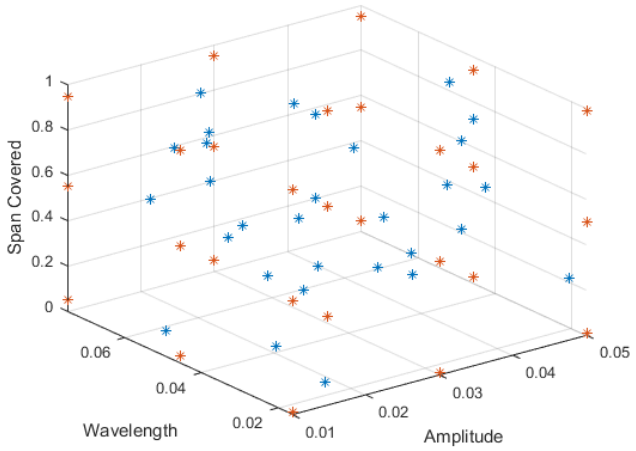

(c) Latin hypercube + full factorial

Figure 4.11: DoE with three design variables.

six wind speeds, which are the same ones used in the wind tunnel tests conducted at the NASA Ames Research Center [48]: 5, 7, 10, 13, 15, and 20 $\mathrm{m/s}$. The flow is assumed to be steady, incompressible, and fully turbulent; even if unsteady phenomena generally characterize the flow at high wind speeds (from 15 $\mathrm{m/s}$), Zhang and Wu [106] showed that the unsteady behaviors of localized vortices have a very limited effect on the overall aerodynamic performance of wind turbine blades. Therefore, Reynolds averaged Navier-Stokes (RANS) equations with the $k-\omega\ SST$ turbulence model are used in the analysis. The $k-\omega\ SST$ model in combination with a $y^+ \leq 1$ prism layer mesh is able to capture the laminar-to-turbulent boundary layer transition [5, 72], even though a fully turbulent assumption has been made. The Reynolds number of the NREL Phase VI blade falls in the low value range ($10^4 - 10^6$); Fig.4.12 shows its variation along the blade span, considering 10 and 20 $\mathrm{m/s}$ of wind speed.

The fluid domain is discretized by using a trimmer mesh, and 50 prism layers with $y^+ \leq 1$ are generated close to the blade surface. An example of the surface mesh on the NREL wind turbine blade with tubercles is shown in Fig.4.13. A block around the blade is created to refine the mesh in that area (Fig.4.14), and the total number of cells characterizing the mesh is about 21 million. A sensitivity study has been conducted to determine the adequate mesh resolution; three mesh densities are generated (i.e., coarse 4×10^6, medium 21×10^6, and fine 56×10^6) to examine if the employed mesh is sufficient for the flow analysis. The sensitivity analysis plot is represented in Fig.4.15.

Based on previous studies [5, 90, 101, 106], the fluid domain around the blade is built with a radius of $6R$; the inlet boundary is located $2R$ upstream and the outlet at $7R$ downstream of the blade, where R is the length of the blade. Preliminary simulations have shown that the flow is unaffected by these domain dimensions. Only one turbine blade is numerically simulated, assuming that the flow is rotationally periodic about the rotation axis. The fluid domain and the boundary conditions are illustrated in Fig.4.16.

Table 4.3 summarizes the mesh and simulation settings applied in this work.

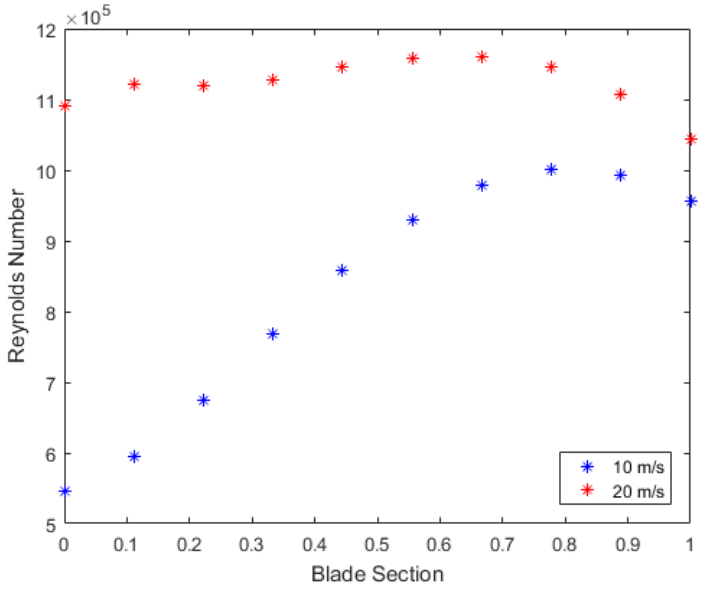

Figure 4.12: Reynolds number values along the NREL Phase VI blade span for two wind speeds.

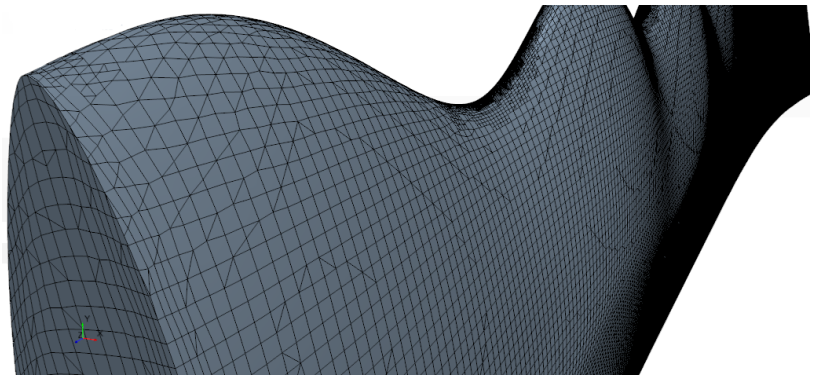

(a) Mesh at the leading edge

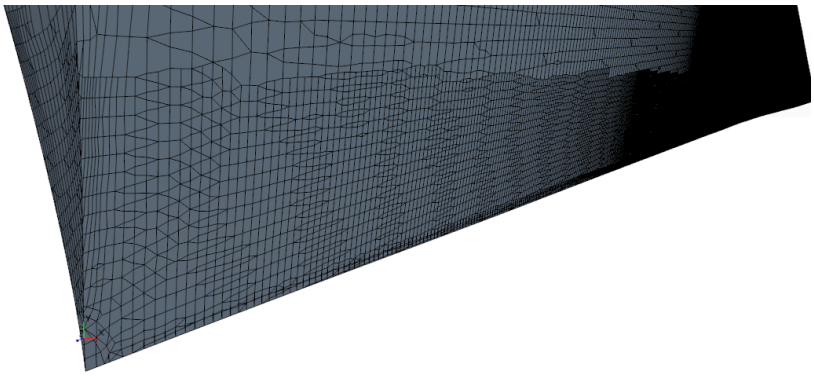

(b) Mesh at the trailing edge

Figure 4.13: Surface mesh on the NREL blade with tubercles.

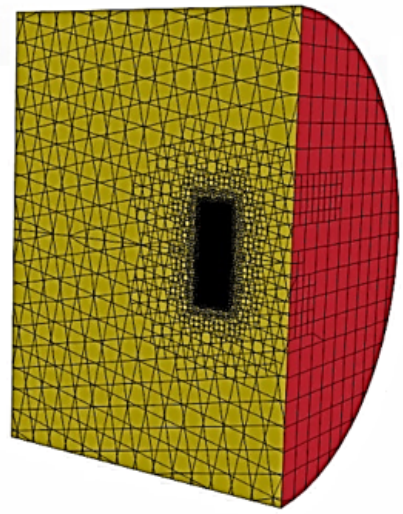

Figure 4.14: Meshed domain with a refinement block around the blade.

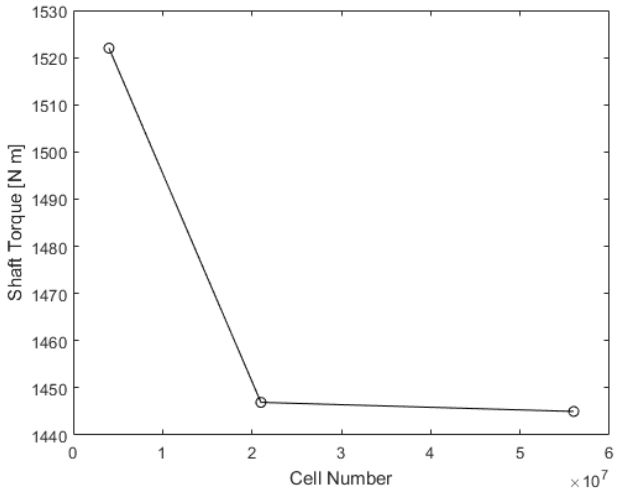

Figure 4.15: Mesh sensitivity study for NREL Phase VI blade at 10 $\mathrm{m/s}$ of wind speed.

Table 4.3: Summary of mesh and simulation settings.

	Settings
Flow	Steady
	Incompressible
	Fully turbulent
Turbulence model	$k-\omega\ SST$
Mesh	Trimmer
	50 prism layers with $y^+ \leq 1$
	$\sim$ 21 million cells
Fluid domain	Radius = $6R$
	Inlet at $2R$ upstream
	Outlet at $7R$ downstream
Boundary conditions	Inlet = velocity inlet
	Outlet = flowsplit outlet
	Symmetry plane = symmetric (periodic)
	Blade = wall

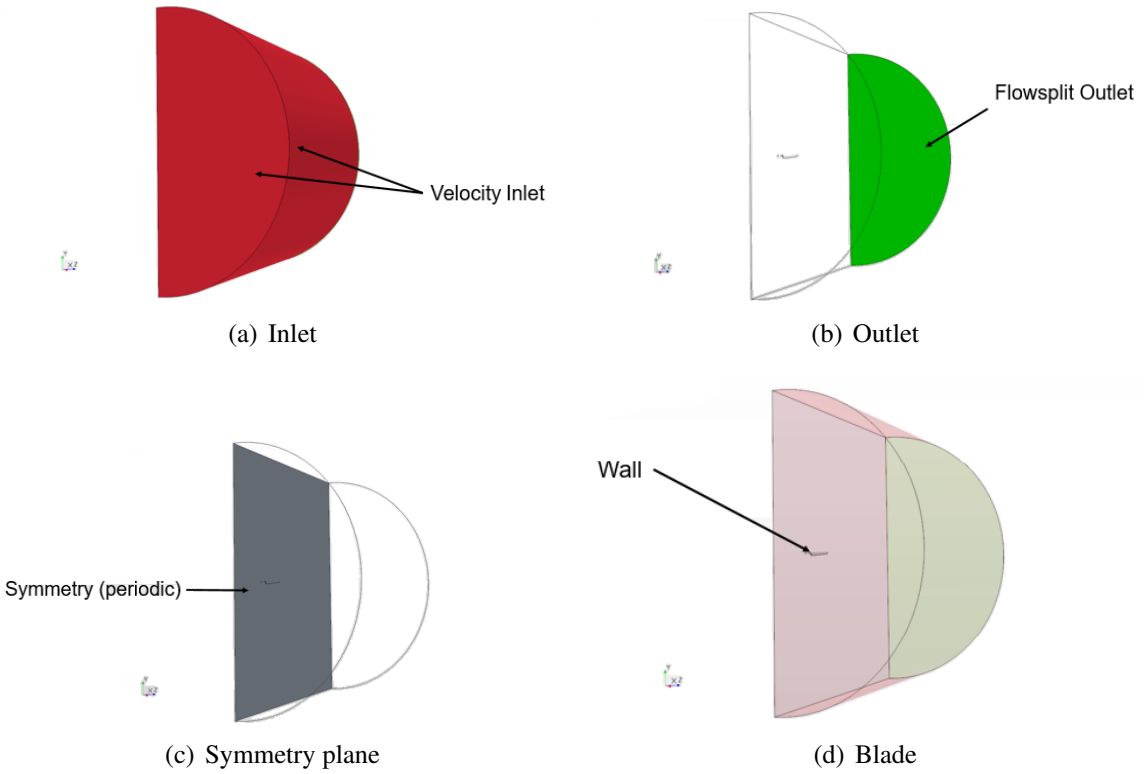

(a) Inlet (b) Outlet

(c) Symmetry plane (d) Blade

Figure 4.16: Boundary conditions of the fluid domain.

4.2.3.1 Validation

The same numerical settings described in the previous section have been applied to the validation process. As mentioned in Sec.4.2.1, the NREL Phase VI blade has been chosen as the baseline geometry since several experimental data are available from Hand *et al* [48]. In particular, the pressure coefficients at different blade span sections and the overall shaft torque have been validated.

The pressure coefficient is calculated using the following expression:

$$C_p = \frac{p - p_\infty}{\frac{1}{2}\rho\left(U_\infty^2 + (r\omega)^2\right)} \tag{4.16}$$

where p_∞ is the pressure of the free-stream flow, ρ is the air density, U_∞ is the free-stream velocity, r is the span location of the airfoil section considered, and ω is the rotational speed of the wind turbine blade. The pressure coefficient is calculated at five different span

locations (i.e., 30%, 47%, 63%, 80%, 95%), and considering four wind speeds (i.e., 5, 10, 15, 20 $\mathrm{m/s}$). The results are reported in Fig.4.17 - 4.20. For the lower wind speeds (i.e., 5 and 10 $\mathrm{m/s}$), a good agreement is found for all five spanwise sections (Fig.4.17,4.18). However, for higher wind speeds (i.e., 15 and 20 $\mathrm{m/s}$), the results do not seem to perfectly match the experimental data due to the stall behavior of the blade (Fig.4.19, and 4.20). At 10 $\mathrm{m/s}$, a flow separation starts at mid-span of the blade and this region of separation moves toward the tip as the wind speed increases. At 15 $\mathrm{m/s}$, the stall region grows and the RANS equations do not seem to be able to predict the pressure distribution over the blade (Fig.4.19), as already shown in previous research [5, 90, 101, 106]. Considering a wind speed of 20 $\mathrm{m/s}$ (Fig.4.20), the blade is in a deep stall and the flow is separated over the entire span; however, the RANS equations give a reasonably good prediction of the pressure distribution over the blade. Similar findings have been reported in prior studies [58, 72, 79, 90, 101, 106].

In Fig.4.21(a), the shaft torque of the baseline blade obtained from the CFD analysis is compared with the experimental data [48], and in Fig.4.21(b), the same values are plotted with results from previous works [5, 90, 101, 106]. These plots show that good agreement between the experimental data and CFD results has been achieved, with the latter lying inside the 1σ error bar provided by Hand *et al.* Ref.[48].

4.2.4 Performance Analysis

CFD results in terms of shaft torque, power, and annual energy production of tubercle configurations are compared with the baseline model. Before going into the details presented in Chapter 5, a brief description of the equations used is given in this section.

The power (P) is evaluated by multiplying the shaft torque (T) coming from the CFD simulations with the rotational speed ($\omega = 7.54\ \mathrm{rad/s}$). The values of P as a funtion of six wind speeds ($U = 5, 7, 10, 13, 15, 20\ \mathrm{m/s}$) are compared with the baseline values. More details about shaft torque and power results are reported in Chapter 5.

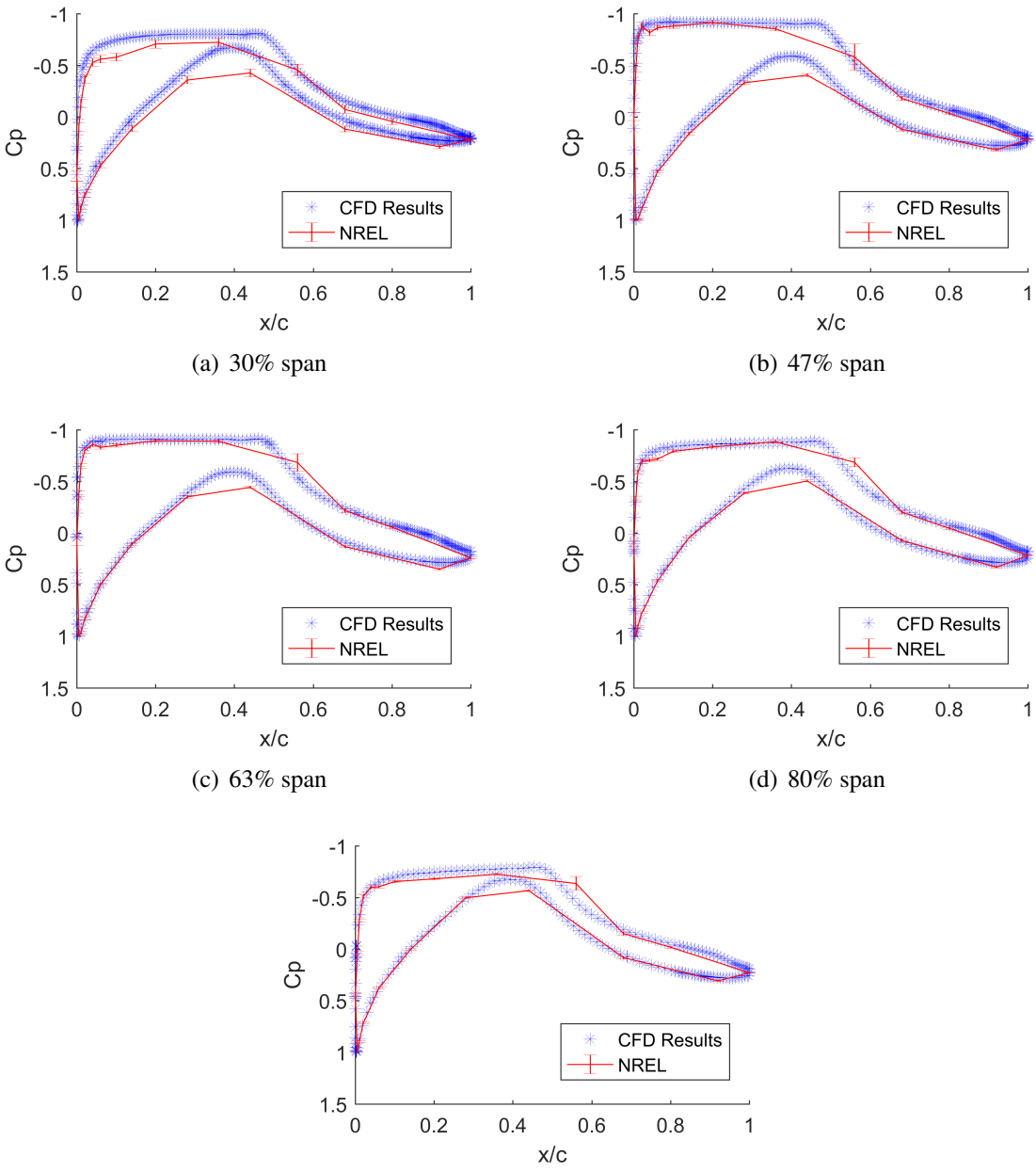

(a) 30% span

(b) 47% span

(c) 63% span

(d) 80% span

(e) 95% span

Figure 4.17: Pressure coefficient at five different span locations of the blade with 5 $\mathrm{m/s}$ of wind speed.

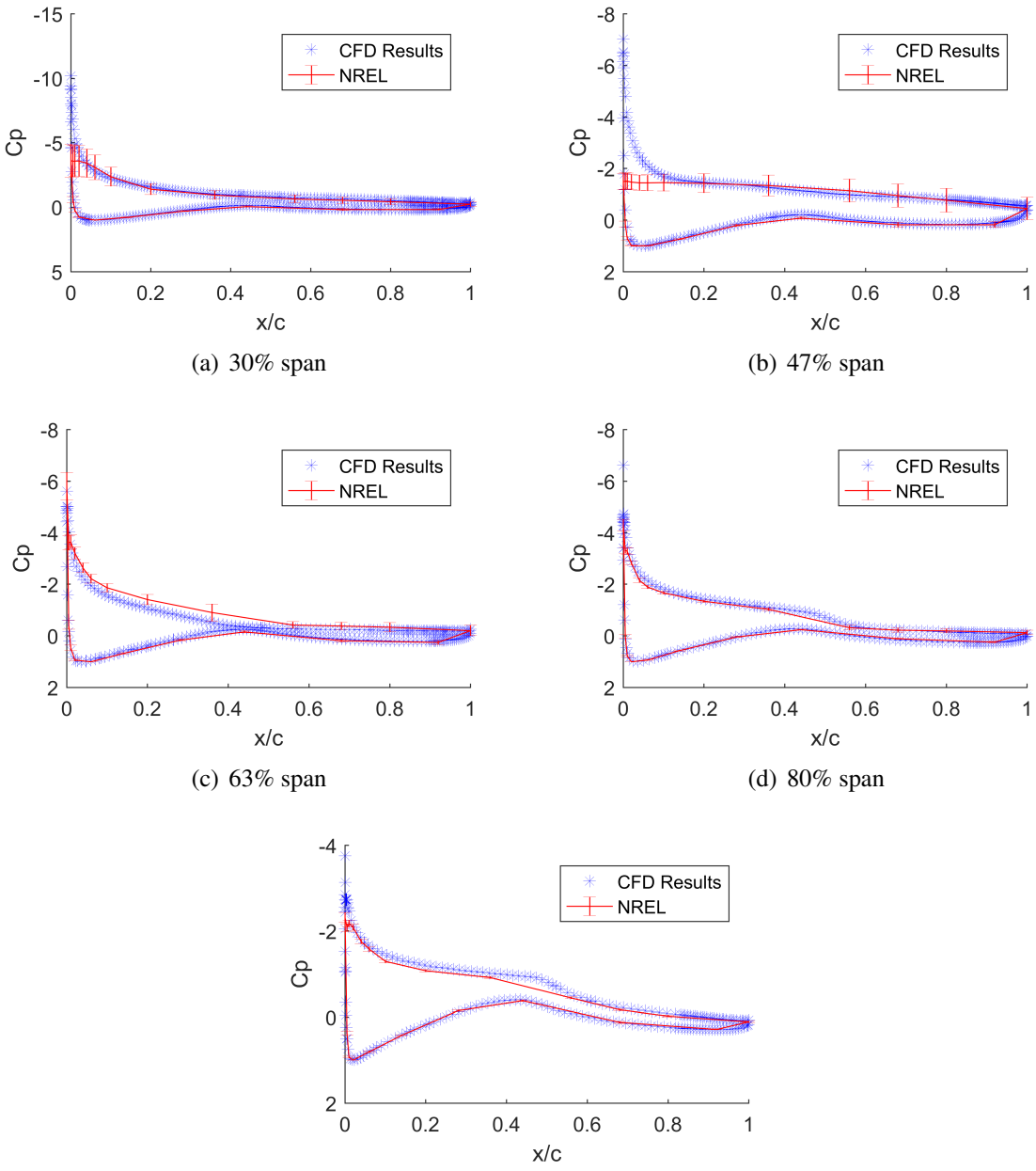

(a) 30% span

(b) 47% span

(c) 63% span

(d) 80% span

(e) 95% span

Figure 4.18: Pressure coefficient at five different span locations of the blade with 10 $\mathrm{m/s}$ of wind speed.

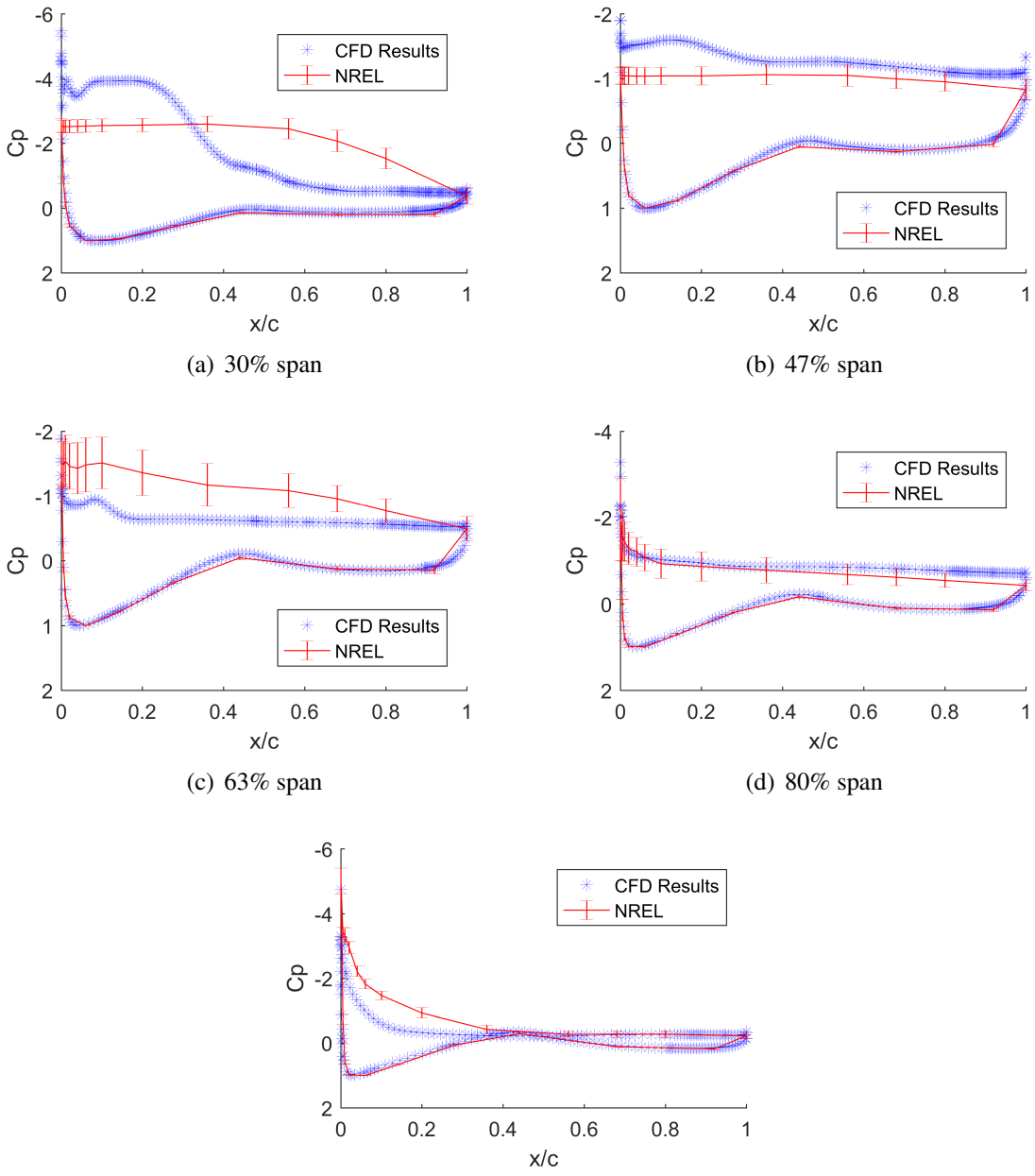

(a) 30% span

(b) 47% span

(c) 63% span

(d) 80% span

(e) 95% span

Figure 4.19: Pressure coefficient at five different span locations of the blade with 15 $\mathrm{m/s}$ of wind speed.

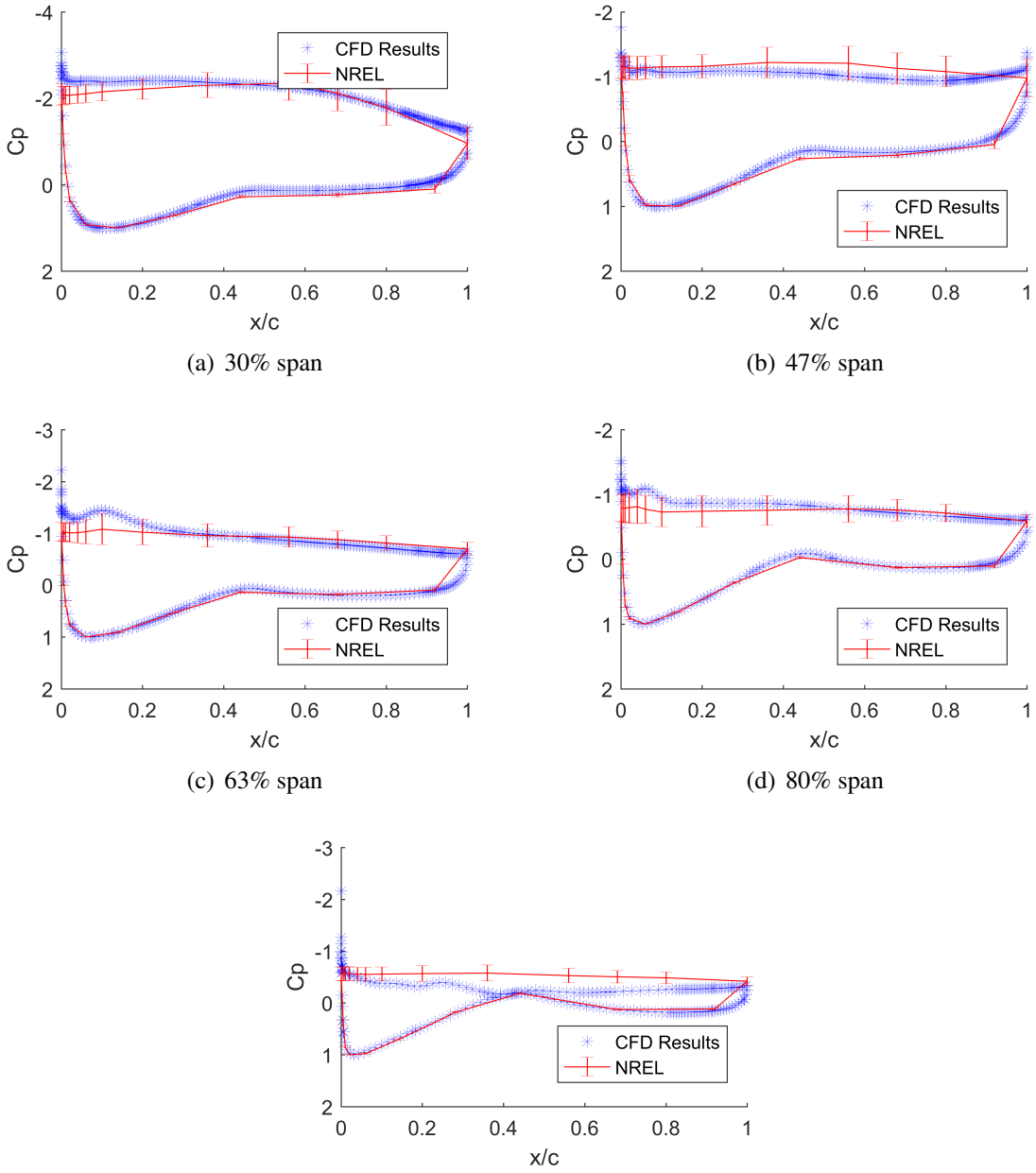

(a) 30% span

(b) 47% span

(c) 63% span

(d) 80% span

(e) 95% span

Figure 4.20: Pressure coefficient at five different span locations of the blade with 20 $\mathrm{m/s}$ of wind speed.

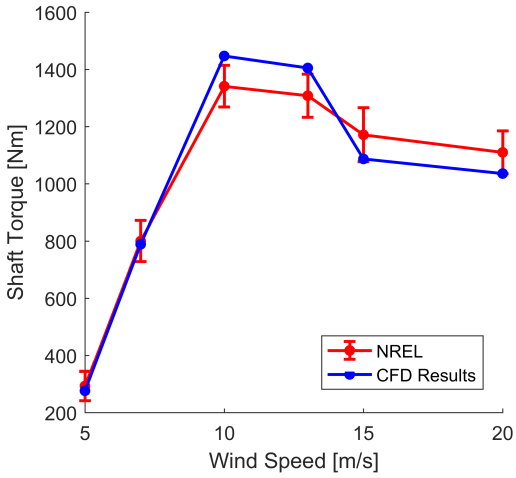

(a) Experimental data and CFD results.

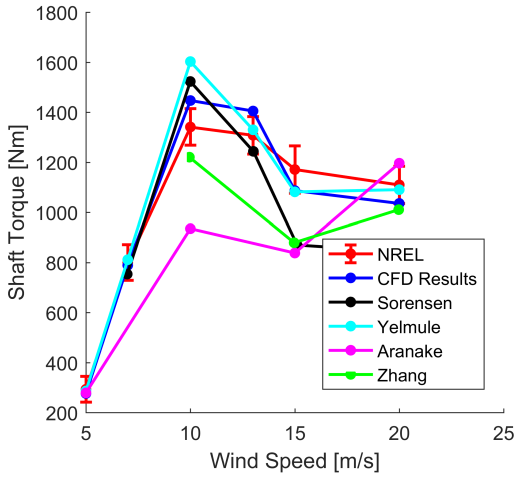

(b) Experimental data, CFD results and previous research results.

Figure 4.21: Shaft torque result comparison.

Another parameter for the performance evaluation of the NREL Phase VI blade with tubercles is the annual energy production. AEP is defined as the energy produced by a turbine in a whole year:

$$\text{AEP} = \overline{P} \cdot 365 \cdot 24 \tag{4.17}$$

where $\overline{P}$ is the average power produced by the wind turbine, 365 are the days in a year, and 24 are the hours per day. The average power ($\overline{P}$) is the integral of the power produced at a given wind speed ($P(U)$) multiplied by the probability ($p(U)$) of that wind speed (U):

$$\overline{P} = \int_0^\infty P\left(U\right) p\left(U\right) dU \tag{4.18}$$

The type of probability distribution used in this work is the Rayleigh distribution, which is defined as:

$$p(U) = \frac{\pi}{2}\left(\frac{U}{\overline{U}^2}\right) \exp\left[-\frac{\pi}{4}\left(\frac{U}{\overline{U}}\right)^2\right] \tag{4.19}$$

where U and $\overline{U}$ are the wind speed and the mean wind speed values, respectively. The Rayleigh probability function gives a reasonable approximation of the wind distribution,

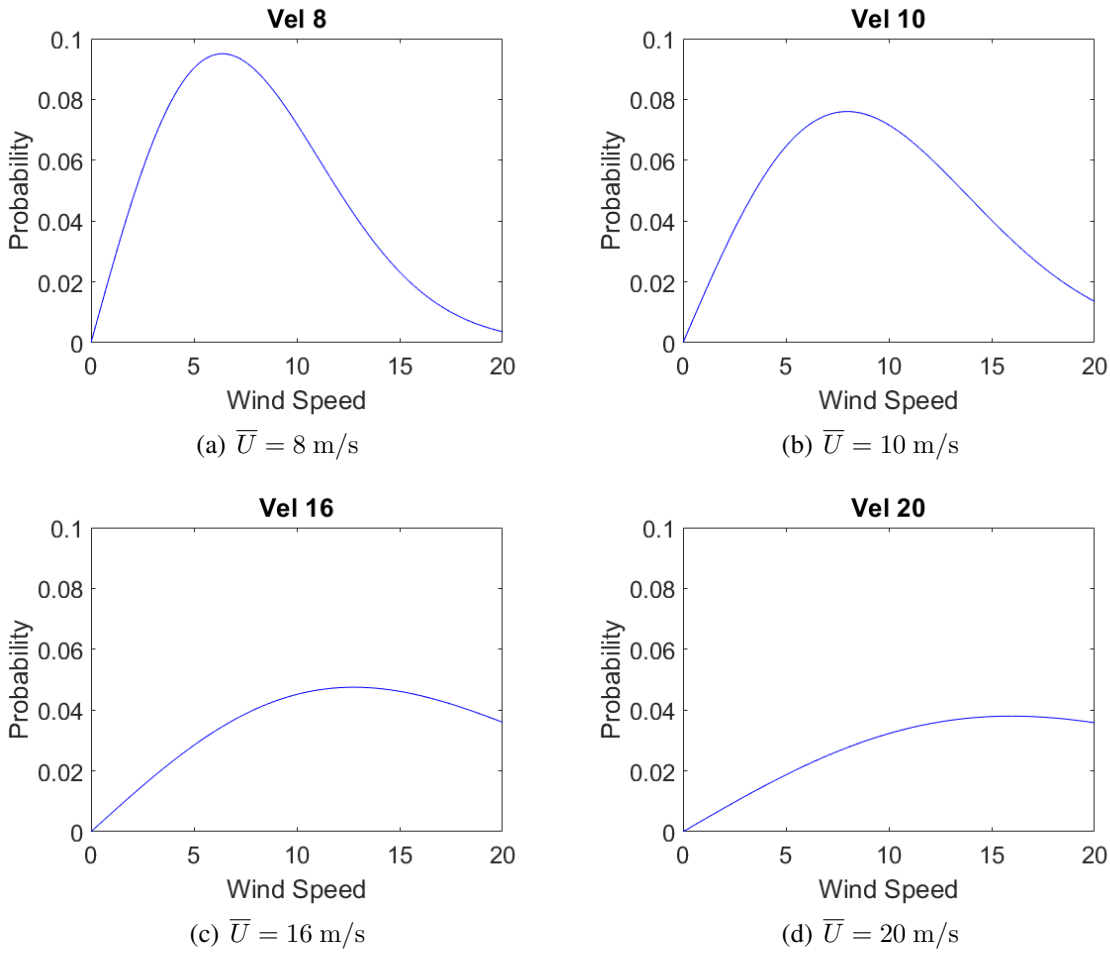

(a) $\overline{U} = 8\ \mathrm{m/s}$ (b) $\overline{U} = 10\ \mathrm{m/s}$

(c) $\overline{U} = 16\ \mathrm{m/s}$ (d) $\overline{U} = 20\ \mathrm{m/s}$

Figure 4.22: Wind probability distribution curve for different mean wind speeds.

centering its peak at low wind speeds (up to 15 $\mathrm{m/s}$), which are more realistic wind conditions. Examples of wind probability distribution curves at mean wind speeds of 8, 10, 16, and 20 $\mathrm{m/s}$ are given in Fig.4.22

The power $P(U)$ is given by the shaft torque $T(U)$ obtained by a spline interpolation of the discrete torque values resulting from the CFD analysis multiplied by the rotational speed ω (7.54 $\mathrm{rad/s}$):

$$P(U) = T\,(U)\,\omega \tag{4.20}$$

For the calculation of the AEP, eight values of the mean wind speed ($\overline{U}$) are considered in a range between 6 and 20 $\mathrm{m/s}$: 6, 8, 10, 12, 14, 16, 18, and 20 $\mathrm{m/s}$. The final results are

evaluated in terms of non-dimensional AEP improvement ($\overline{\Delta\text{AEP}}$):

$$\overline{\Delta\text{AEP}}_i = \frac{\text{AEP}_i - \text{AEP}_{\text{NREL}}}{\text{AEP}_{\text{NREL}}} \tag{4.21}$$

which is the difference between the AEP of the i-th case (AEP_i) and the value of the regular NREL Phase VI blade (AEP_{NREL}) divided by AEP_{NREL}.

4.2.5 Surrogate Modeling

Due to the scattered characteristic of data collected via CFD analysis, a surrogate modeling technique is used to investigate the behavior of performance parameters across the entire design space. In particular, this section reports the surrogate model formulations used for the analysis of results obtained with two-and three-dimensional DoEs (Sec.4.2.2).

4.2.5.1 Two-dimensional DoE

To better visualize the evolution in power improvement given by tubercles at different wind speeds, a surrogate model is generated. In particular, a second order polynomial response surface [17, 20, 84] is fitted on the CFD data to identify trends in the non-dimensonal power improvement ($\overline{\Delta P}$) as a function of non-dimensional amplitude and non-dimensional wavelength. The second order equation used is the following:

$$\hat{y}(\mathbf{x}_*) = C_1\bar{A}^2 + C_2\bar{\lambda}^2 + C_3\bar{A}\bar{\lambda} + C_4\bar{A} + C_5\bar{\lambda} + C_6 \tag{4.22}$$

where $\mathbf{x}_*$ is the evaluation point, and C_i are the polynomial coefficients. The function $\overline{\Delta P}_i$ is defined as:

$$\overline{\Delta P}_i = \frac{P(U)_i - P(U)_{\text{NREL}}}{P(U)_{\text{NREL}}} \tag{4.23}$$

which is the difference between the power of a CFD case ($P(U)_i$) and of the regular NREL ($P(U)_{\text{NREL}}$) at the same speed U normalized by the NREL power ($P(U)_{\text{NREL}}$). The 20

blades generated by the Latin hypercube DoE (Sec.4.2.2) are necessary to train the surrogate model, and the resulting coefficients C_i are used for the evaluation of $\overline{\Delta P}_i$. Five wind speeds (i.e., 7, 10, 13, 15, and 20 $\mathrm{m/s}$) are considered for the generation of five different surrogate models. Residuals (Res) are calculated as:

$$\text{Res}_i = \overline{\Delta P}_{\text{train}i} - \overline{\Delta P}_{\text{pred}_i} \tag{4.24}$$

where $\overline{\Delta P}_{\text{train}i}$ and $\overline{\Delta P}_{\text{pred}_i}$ are the $\overline{\Delta P}$ of each training case and the corresponding predicted value, respectively. As presented in Sec.4.1, the goodness of fit of the models is evaluated in terms of R^2 and normalized root mean square error (NRMSE), which in this case is defined as follows:

$$\text{NRMSE} = \frac{\text{RMSE}}{max(\overline{\Delta P}_{\text{train}}) - min(\overline{\Delta P}_{\text{train}})} \tag{4.25}$$

4.2.5.2 Three-dimensional DoE

The main goal of this work is to give insights into the application of tubercles on the NREL Phase VI blades to achieve performance enhancement. To reach this objective, a third order polynomial response surface [17, 20, 84] is fitted on the CFD data to reveal the evolution of the shaft torque as a function of three design variables: non-dimensional amplitude ($\bar{A}$), non-dimensional wavelength ($\bar{\lambda}$), and non-dimensional span coverage ($\bar{z}_{\text{tub}}$). The following third order polynomial equation is considered:

$$\begin{aligned}\hat{y}(\mathbf{x}_*) =& C_1\bar{A}^3 + C_2\bar{\lambda}^3 + C_3\bar{z}_{\text{tub}}^3 + C_4\bar{A}^2\bar{\lambda} + C_5\bar{A}^2\bar{z}_{\text{tub}} + \\ &+ C_6\bar{A}\bar{\lambda}^2 + C_7\bar{A}\bar{z}_{\text{tub}}^2 + C_8\bar{\lambda}^2\bar{z}_{\text{tub}} + C_9\bar{\lambda}\bar{z}_{\text{tub}}^2 + C_{10}\bar{A}\bar{\lambda}\bar{z}_{\text{tub}} + \\ &+ C_{11}\bar{A}^2 + C_{12}\bar{\lambda}^2 + C_{13}\bar{z}_{\text{tub}}^2 + C_{14}\bar{A}\bar{\lambda} + C_{15}\bar{A}\bar{z}_{\text{tub}} + \\ &+ C_{16}\bar{\lambda}\bar{z}_{\text{tub}} + C_{17}\bar{A} + C_{18}\bar{\lambda} + C_{19}\bar{z}_{\text{tub}} + C_{20}\end{aligned} \tag{4.26}$$

where $\mathbf{x}_*$ is the evaluation point, and C_i are the polynomial coefficients. The 57 cases generated by Latin hypercube and full factorial DoEs (Sec.4.2.2) are considered training points for the surrogate model, and the resulting polynomial coefficients are used for the evaluation of the predicted non-dimensional torque variation ($\overline{\Delta T}$):

$$\overline{\Delta T}_i = \frac{T_i(U) - T_{\text{NREL}}(U)}{T_{\text{NREL}}(U)} \tag{4.27}$$

where T_i is the shaft torque value of a tubercle configuration evaluated by the surrogate model, and T_{NREL} is the torque of the regular NREL blade. Similar to what has been done for the two-dimensional DoE (Sec.4.2.5.1), the same five wind speeds (i.e., 7, 10, 13, 15, and 20 $\mathrm{m/s}$) are considered for the generation of five surrogate models. The wind speed could be considered as the fourth design variable, but that approach would have led to a four-dimensional design space, which is extremely challenging to visualize. Residuals (Res) are calculated as:

$$\text{Res}_i = \overline{\Delta T}_{\text{train}i} - \overline{\Delta T}_{\text{pred}_i} \tag{4.28}$$

where $\overline{\Delta T}_{\text{train}i}$ and $\overline{\Delta T}_{\text{pred}_i}$ are the $\overline{\Delta T}$ of each training case and the corresponding predicted value, respectively. Two of the training cases with maximum and minimum Res are excluded for the surrogate model generation, and the model is trained again for the goodness of fit evaluation in terms of R^2 and NRMSE. R^2 is calculated as described in Sec.4.1, and the RMSE is normalized considering the difference between maximum and minimum values of $\overline{\Delta T}_{\text{train}}$:

$$\text{NRMSE} = \frac{\text{RMSE}}{max(\overline{\Delta T}_{\text{train}}) - min(\overline{\Delta T}_{\text{train}})} \tag{4.29}$$

4.3 Simulation Framework

The steps listed and described in Sec.4.2 are combined and coded in a simulation framework as illustrated in Fig.4.23. First, a DoE is used to generate the cases ($\mathbf{x}_i$) that will be

tested to sample the design space. Then, each tubercle configuration $\mathbf{x}_i$ is passed to the simulation framework, which involves a geometry creation, a mesh computation, and the CFD simulation. The generation of each blade geometry requires several minutes, depending on the complexity of tubercle configuration, and it is saved in an STL file. Before deciding to use the STL format to handle blade geometries, several computer-aided design (CAD) software packages were considered: SolidWorks©, SolidEdge©, CATIA©, AutoCAD©, and Blender©. All the geometry formats available in these software packages were affected by several issues when imported into the mesher (specifically the Star-CCM+© mesher), as summarized in Table 4.4. The only way to overcome this geometry file incompatibility was to write a custom MATLAB© script that is able to generate the blade geometry STL file from the given geometric parameters (including also the design variables).

Once the geometry creation process has been completed, the resulting STL file is imported into Star-CCM+ for mesh generation. This step is highly computationally expensive since the resulting meshes consist of about 21 million cells (Sec.4.2.3); on average, it requires more than 30 minutes for each case, depending on the geometry complexity. Star-CCM+ software is used because it embodies both the mesh generation and the CFD simulation in a single code. This aspect reduces the risk of format incompatibility when handling the mesh file, resulting in a faster and more efficient procedure.

Each three-dimensional CFD simulation requires around 24 hours, meaning that since each case has to be evaluated at six wind speeds (i.e., 5, 7, 10, 13, 15, and 20 $\mathrm{m/s}$), the total simulation time per DoE sample is around 144 hours. Considering that the three design variable DoE consists of 57 samples (Sec.4.2.2), running these simulations on a single desktop computer would have required a total of 340 days. To reduce this enormous amount of computational time, the framework has been adapted to work with the HPC (high-performance computing) resources available through the Georgia Tech Partnership for Advanced Performance Computing (PACE) cluster, as represented in Fig.4.24. With the

Table 4.4: Summary of errors when different CAD formats have been imported in Star-CCM+.

CAD File Format	Star-CCM+ errors
.stl	problems in importing the geometry
.iges	problems in mesh generation
.step	problems in importing geometries with low wavelength values

parallel implementation it is possible to run an average of three simulations simultaneously by using 3 cluster nodes of 12 processors each. In this way, the total computational time required to simulate an entire DoE is considerably reduced (to about three months for the specific three design variable DoE). Figure 4.24 presents a schematic representation of the master (local) machine where the DoEs are generated, and how the simulation framework is replicated in each node of the Georgia Tech cluster. The final simulation files have been moved to the local machine for the post-processing phase, where by using MATLAB, Star-CCM+, and Paraview© it was possible to analyze the results and create plots to easily visualize them.

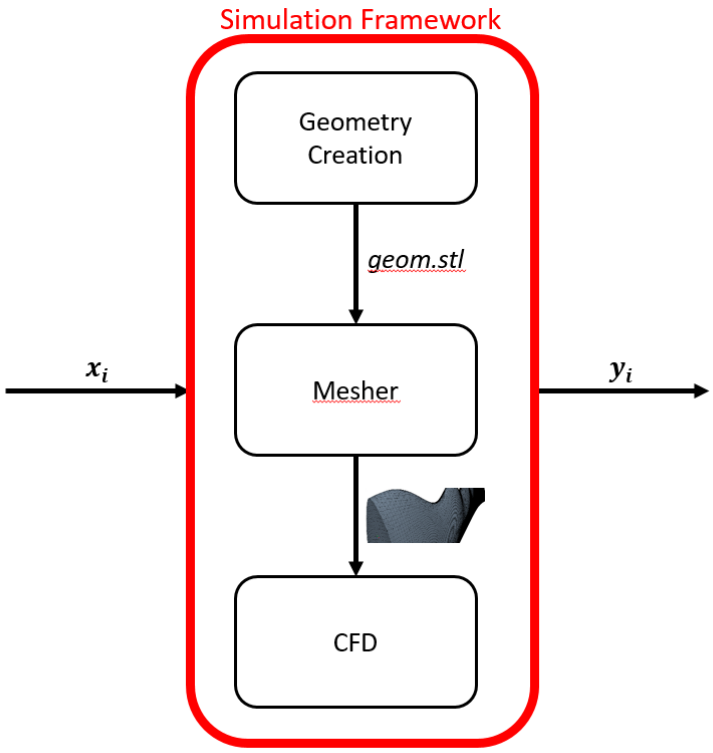

Figure 4.23: Simulation framework.

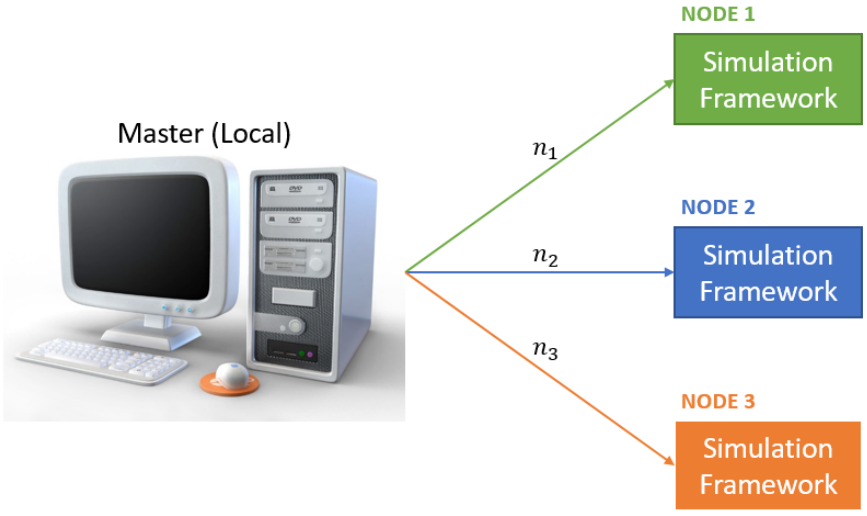

Figure 4.24: Local computer and Georgia Tech PACE cluster.

CHAPTER 5

RESULTS

5.1 Introduction

This chapter analyzes the CFD results in terms of shaft torque and annual energy production by comparing them with the baseline blade. Physical phenomena involved in the tubercle working principle are also described to better understand performance improvement or degradation given by the application of tubercles on the NREL Phase VI blade. The result analysis is divided into three steps, depending on the number of design variables involved in the DoE generation:

- two design variables (tubercle amplitude and wavelength);
- one design variable (starting spanwise location); and
- three design variables (amplitude, wavelength, and span coverage).

5.2 Two Design Variable DoE

In the first phase of this work, a Latin hypercube design of experiments (Sec.4.2.2) with two design variables (i.e., non-dimensional amplitude and non-dimensional wavelength) has been considered for the generation of 20 tubercle configurations to test by a three-dimensional CFD analysis. The ranges of the design variables are reported in Table 4.1, and the resulting sample points in the design space are represented in Fig.4.8.

Results of the 20 blades in terms of shaft torque are plotted in Fig.5.1 and compared with the baseline blade. All the cases generated by the DoE show a negligible difference in the shaft torque at 5 and 7 $\mathrm{m/s}$ of wind speed; at 10 $\mathrm{m/s}$, tubercles have a strong

negative effect, which decreases with movement toward the off-design condition (i.e., 20 $\mathrm{m/s}$). In particular, between 13 and 15 $\mathrm{m/s}$, the shaft torque values start to approach those of the baseline until having reached 20 $\mathrm{m/s}$, they significantly increase. Similar trends are noticible in the power comparison represented in Fig.5.2, where the power is calculated by multiplying the shaft torque for the constant rotational speed of the wind turbine (i.e., 7.54 $\mathrm{rad/s}$). As mentioned in Sec.4.2.5.1, due to the scattered characteristic of the CFD data, a surrogate model is generated to better visualize the evolution in power improvement ($\overline{\Delta P}$) given by tubercles at different wind speeds. Five surrogate models are generated, corresponding to five different wind speeds (i.e., 7, 10, 13, 15, and 20 $\mathrm{m/s}$). Each model is trained by using the 20 DoE cases (Sec.4.2.2), and the goodness of fit is evaluated in terms of R^2 and NRMSE (Sec.4.2.5.1). Table 5.1 reports the resulting values of R^2 and NRMSE for the five surrogate models. Most of the R^2 values are very close to 1 with low NRMSE. At 13 and 15 $\mathrm{m/s}$, the surrogate model does not seem to work perfectly since R^2 moves away from 1, resulting in 0.88 at 13 $\mathrm{m/s}$ and 0.91 at 15 $\mathrm{m/s}$; moreover, the NRMSE is slightly higher than the other wind speeds (around 7%). The reason for that is probably linked to the complexity of flow conditions at those two wind speeds, since they correspond to a transitional region between design and off-design regimes.

Looking at the overall R^2 and NRMSE values, it is possible to affirm the goodness of the surrogate models generated that is confirmed by some plots representing the actual versus predicted (Fig.5.3(a)) and residual versus predicted (Fig.5.3(b)) values. In Fig.5.3, those plots refer to a wind speed of 10 $\mathrm{m/s}$; in particular, Fig.5.3(a) represents the DoE cases (black dots) distributed along the fit line (red line) without any relevant clumping; Fig.5.3(b) shows how they are randomly spread without any particular pattern. These two characteristics (i.e., no clumping, no pattern) confirm the good prediction of the non-dimensional power improvement ($\overline{\Delta P}$) given by the generated surrogate models. Contour plots of $\overline{\Delta P}$ (Sec.4.2.5.1) predicted at 7, 10, 13, 15, and 20 $\mathrm{m/s}$ of wind speed are reported in Fig.5.4. As expected, the best tubercle configuration at the design condition (i.e., 10

Table 5.1: R^2 and NRMSE for the five surrogate models with two design variables.

Wind Speed	R^2	NRMSE
7	0.9842	0.0302
10	0.9644	0.0510
13	0.8897	0.0752
15	0.9129	0.0798
20	0.9220	0.0732

$\mathrm{m/s}$; Fig.5.4(b)) is close to the baseline blade geometry with an amplitude approaching 0 and the wavelength going to infinity. Moving from the design to off-design conditions, there is an opposite trend with a transition phase at 15 $\mathrm{m/s}$. In particular, at 20 $\mathrm{m/s}$ of wind speed, the highest power improvement (more than 40%) seems to be achieved in the area of the design space where tubercles are characterized by high amplitude (between 0.045 and 0.05) and low wavelength (between 0.016 and 0.025), meaning pronounced tubercles very close to each other.

The reason for these results can be explained looking at the physical phenomenon behind tubercles. Previous studies [33, 49, 50, 51, 78] showed how leading edge sinusoidal modifications redirect and accelerate the oncoming flow to their troughs, where vorticity of alternate sign leads to the development of counter-rotating vortices that re-energize the boundary layer, delaying flow separation. The deviation of the flow due to tubercles is visible in Fig.5.5 where the streamlines on the regular NREL blade are compared with a representative blade with leading edge bumps (Case 7). Figure 5.6 shows the limiting streamlines on the suction sides of both blades at the design condition (i.e., 10 $\mathrm{m/s}$), underlying the presence of vortices generated by tubercles. The regular blade (Fig.5.6(a)) is characterized by a transitional region in the first half of the span with some flow moving from root to midspan; on the second half of the blade, the flow is unperturbed and attached to the surface. Looking at the blade with tubercles (Fig.5.6(b)), the development of counter-rotating

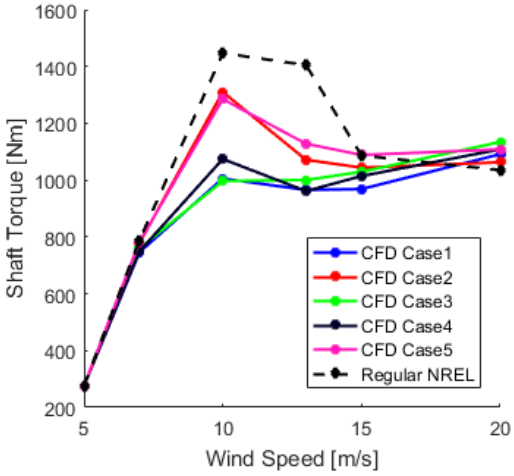

(a) Cases 1-5

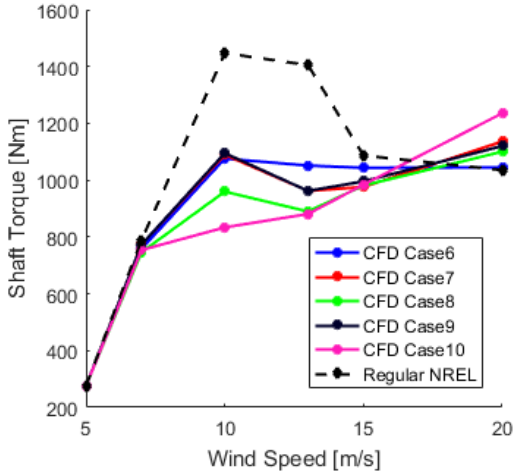

(b) Cases 6-10

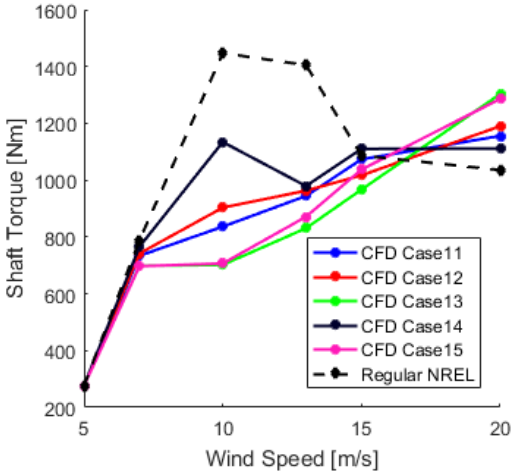

(c) Cases 11-15

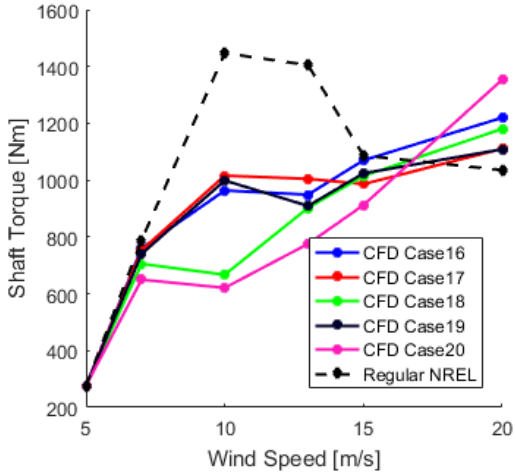

(d) Cases 16-20

Figure 5.1: Torque comparison of the 20 CFD cases with the baseline blade.

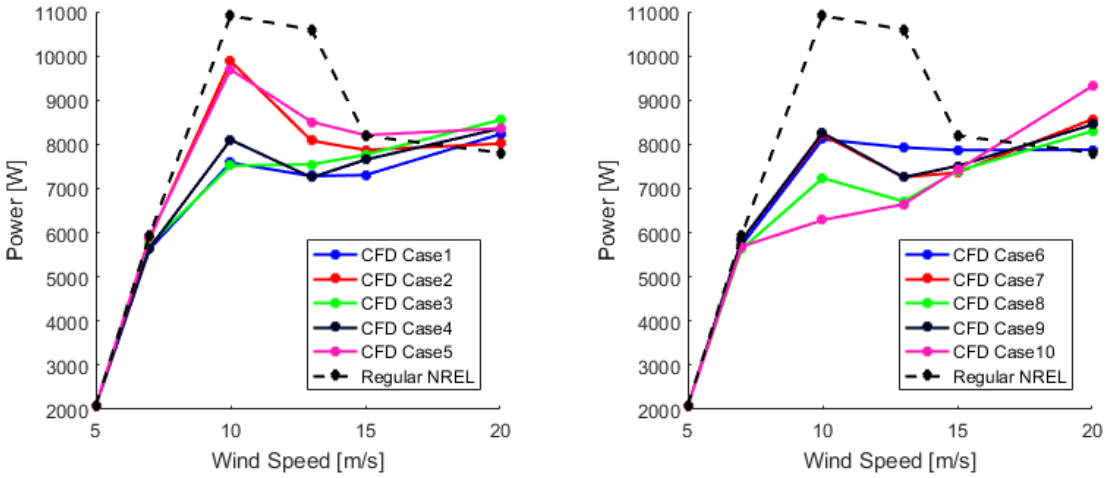

(a) Cases 1-5

(b) Cases 6-10

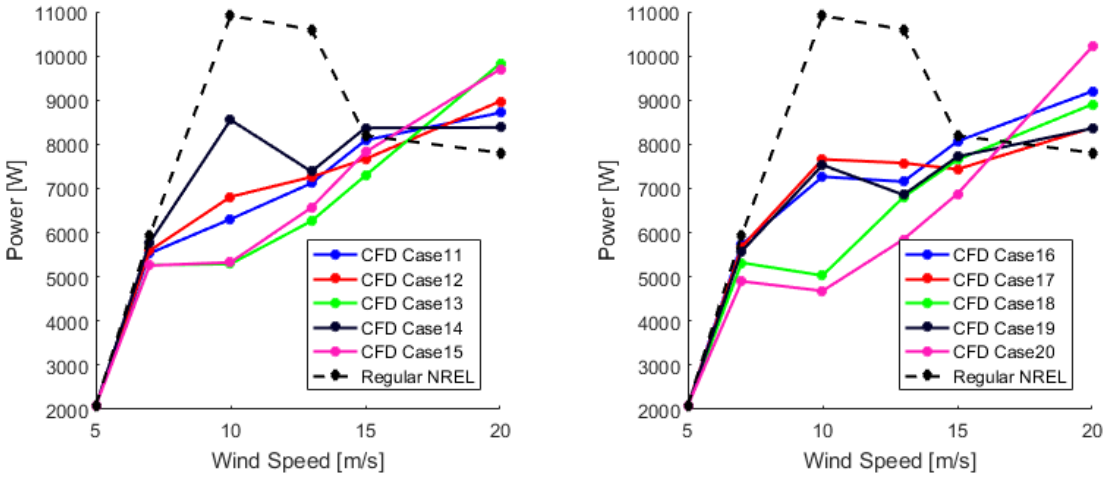

(c) Cases 11-15

(d) Cases 16-20

Figure 5.2: Power comparison of the 20 CFD cases with the baseline blade.

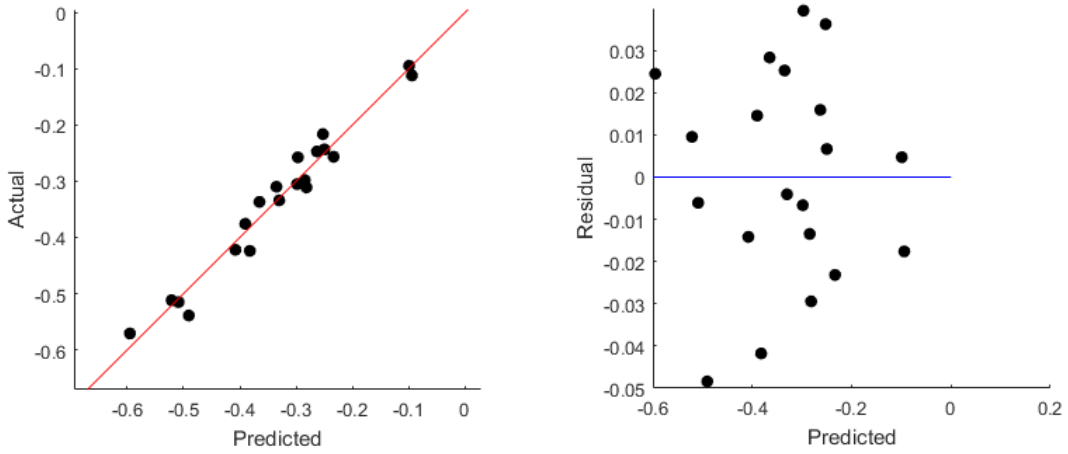

(a) Actual vs Predicted (b) Residual vs Predicted

Figure 5.3: Goodness of fit of the surrogate model with two design variables considering 10 $\mathrm{m/s}$ of wind speed.

vortices, which seem to have stronger intensity moving toward the blade tip, is probably due to the increase of the flow's relative velocity. These vortices affect the original laminar flow in the second half of the blade, leading to a degradation in performance. To better capture the effects of tubercles on blade aerodynamics, this study considers an off-design condition at which the blade is in a full stall; in fact, at 20 $\mathrm{m/s}$ of wind speed, the blade is characterized by a visible strong spanwise flow going from the root to the tip (Fig.5.7). In this particular condition, the vortices generated by tubercles seem to prevent the spanwise flow diffusion, leading to a reduction in the stall strength and to an improvement in the aerodynamic performance. This phenomenon is more visible in Fig.5.8, where the spanwise relative velocity is plotted on a cross section of the regular blade and of Case 7. There is a strong deceleration of the spanwise flow, especially close to the leading edge due to the effects of the counter-rotating vortices, which seem to act like a wall slowing down a portion of the spanwise flow. This phenomenon leads to a reduction in the blade stall strength and to an improvement in the aerodynamic performance.

Another important element to consider in the physical analysis of tubercles is the tip vortex. Looking at the comparison between the tip vortices generated by the regular NREL

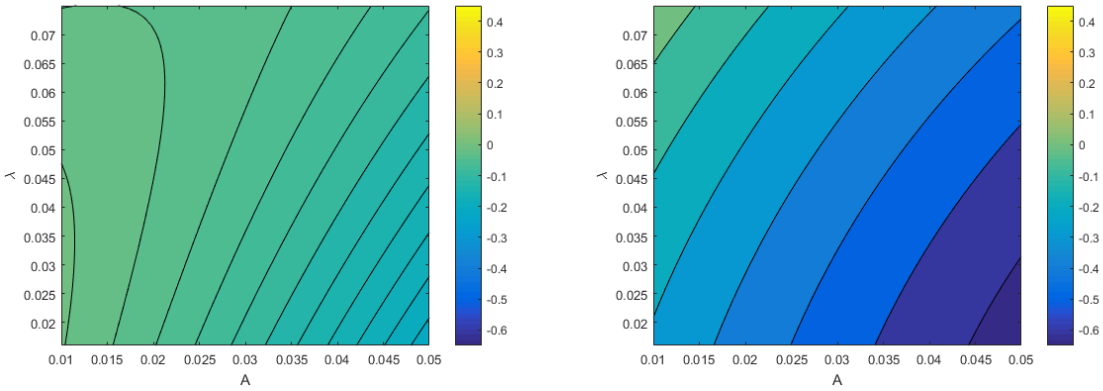

(a) 7 m/s (b) 10 m/s

(c) 13 m/s (d) 15 m/s

(e) 20 m/s

Figure 5.4: $\overline{\Delta P}$ contour plots at different wind speeds.

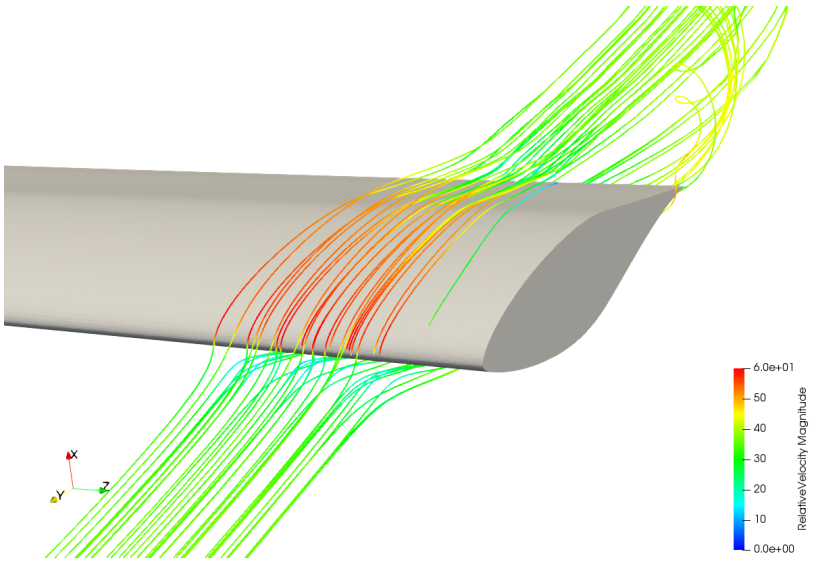

(a) NREL Phase VI

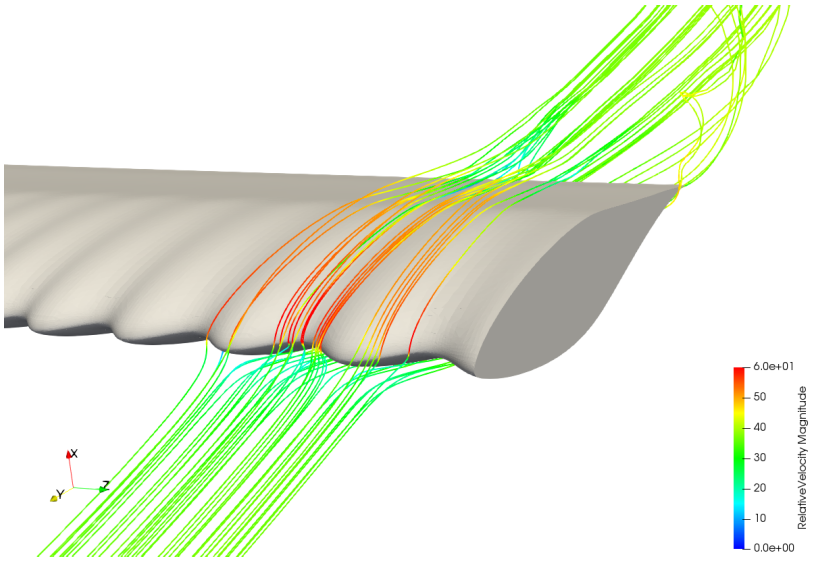

(b) Case 7

Figure 5.5: Streamlines on regular and modified blades.

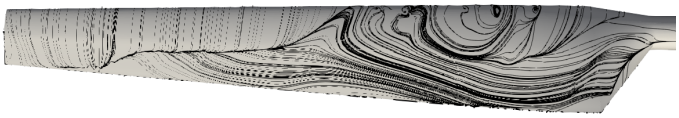

(a) NREL Phase VI

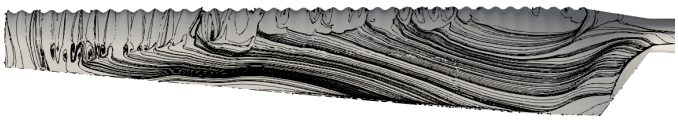

(b) Case 7

Figure 5.6: Limiting streamlines on the suction side at 10 $\mathrm{m/s}$ of wind speed.

(a) NREL Phase VI

(b) Case 7

Figure 5.7: Limiting streamlines on the suction side at 20 $\mathrm{m/s}$ of wind speed.

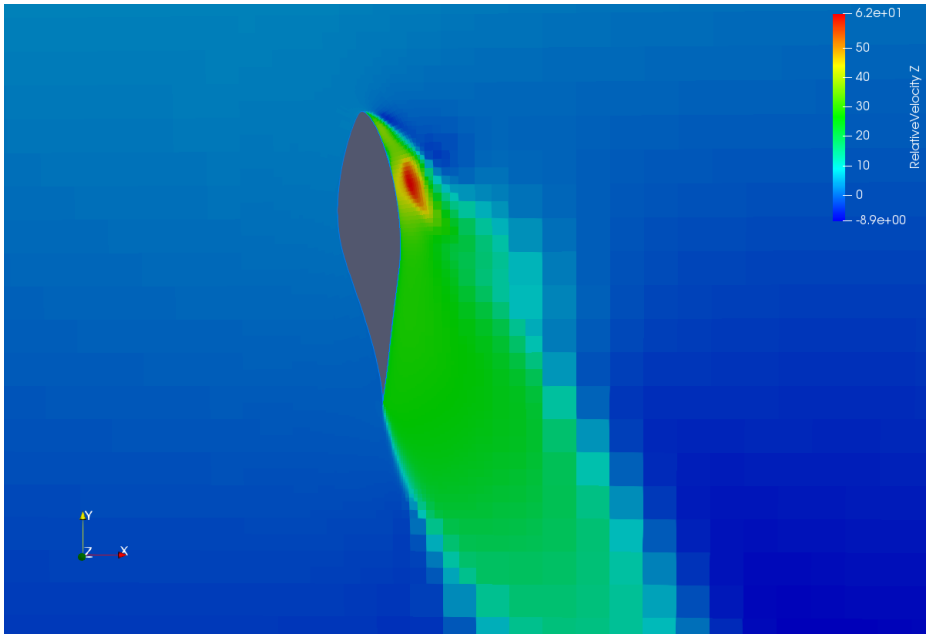

(a) NREL Phase VI

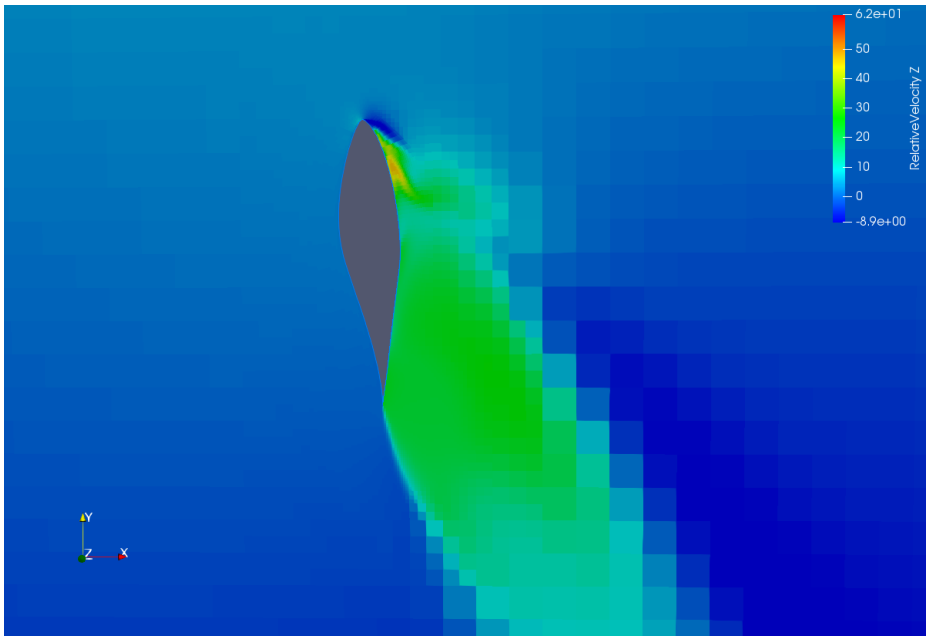

(b) Case 7

Figure 5.8: Spanwise relative velocity on a cross-section at 20 $\mathrm{m/s}$ of wind speed.

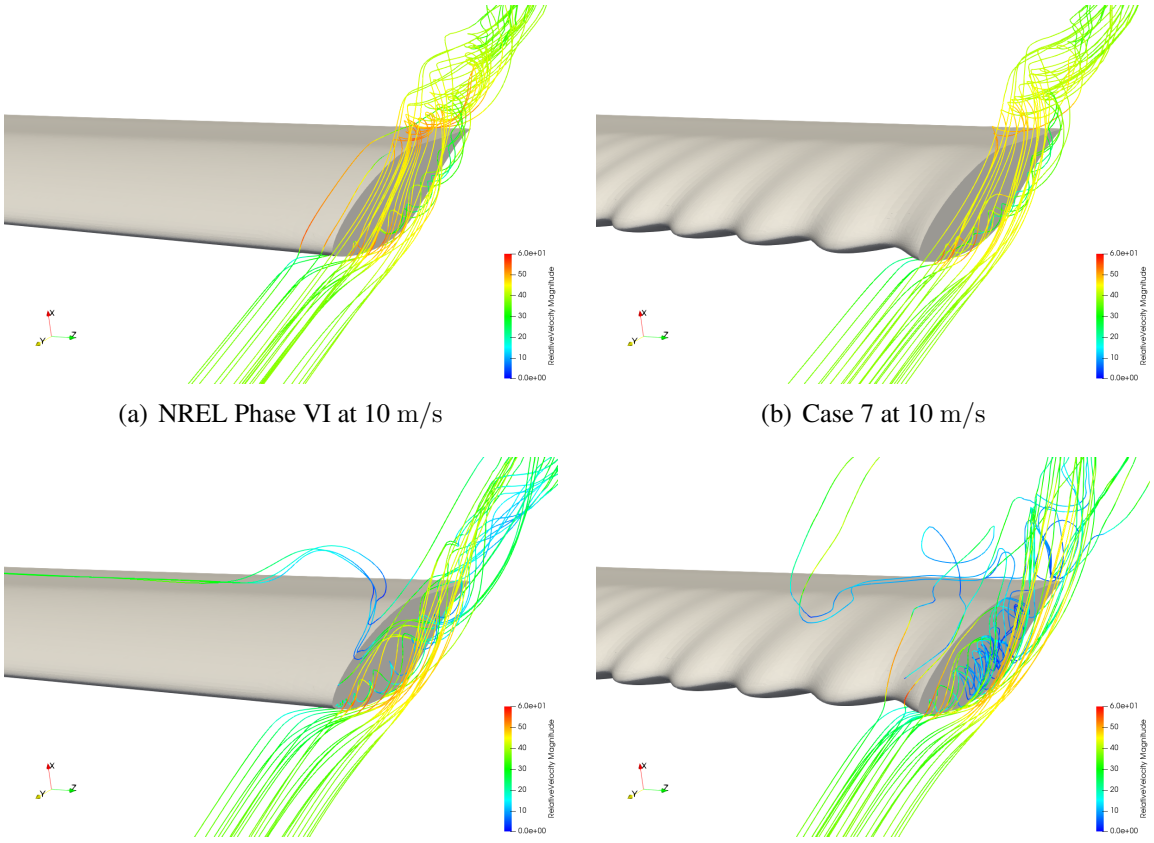

(a) NREL Phase VI at 10 $\mathrm{m/s}$ (b) Case 7 at 10 $\mathrm{m/s}$

(c) NREL Phase VI at 20 $\mathrm{m/s}$ (d) Case 7 at 20 $\mathrm{m/s}$

Figure 5.9: Tip vortex on the regular and modified blades.

blade and the blade with tubercles (Fig.5.9), the presence of leading edge bumps affects the tip vortex intensity, especially in the off-design conditions (i.e., 20 $\mathrm{m/s}$) (Fig.5.9(d)). This phenomenon is confirmed by looking at the vorticity behind the regular blade and the two representative CFD cases (i.e., Cases 7 and 15) (Fig.5.10): the strength of the tip vortex is affected by the presence of tubercles, and depending on the shape of the last tubercle (i.e., ending with a peak, Fig.5.10(b), or a trough, Fig.5.10(c)), the effect can be different. The reason is probably linked to the direction of the last counter-rotating vortex that can have a positive or a negative effect on the tip vortex interaction. A better understanding of the tip vortex effect and its relation with the geometry of the last tubercle requires a deeper analysis.

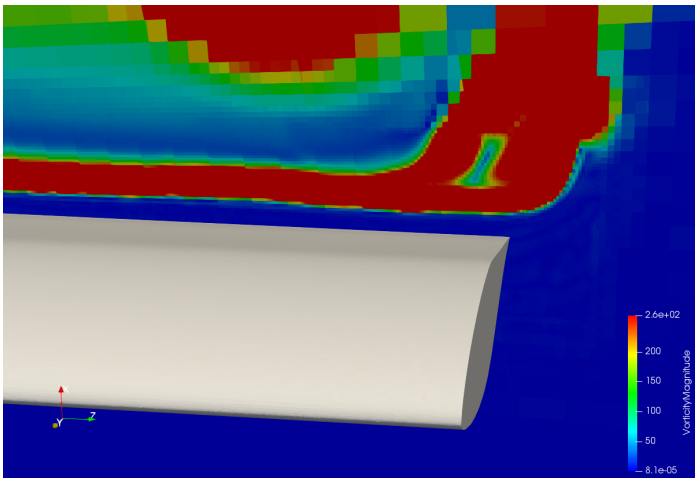

(a) NREL Phase VI

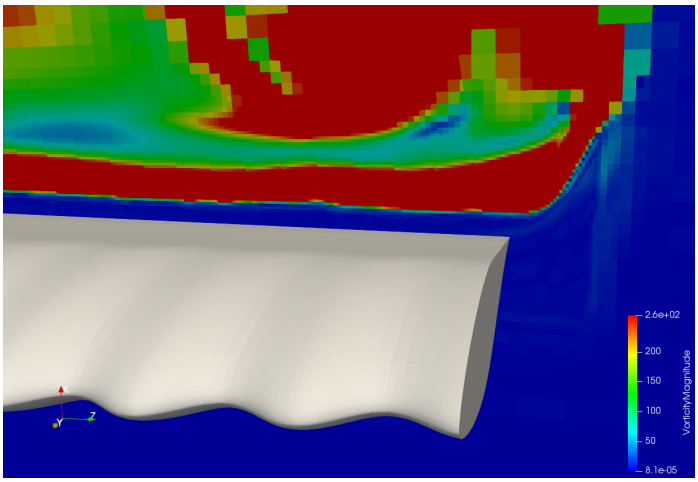

(b) Case 7

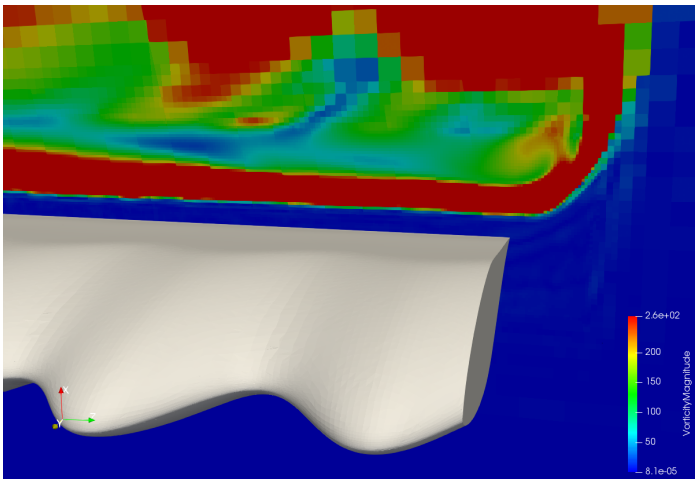

(c) Case 15

Figure 5.10: Vorticity behind the blade tip at 20 $\mathrm{m/s}$ of wind speed.

Results in terms of annual energy production for mean wind speeds of 8, 10, 16, and 20 $\mathrm{m/s}$ are reported in Fig.5.11, where each dot represents a negative value of $\overline{\Delta \mathrm{AEP}}$ (Sec.4.2.4), and the dot size is a function of its magnitude: the bigger the dot, the higher the AEP reduction (more details about these results are presented in Table D.1 in Appendix D). The reason there is an AEP degradation across the entire design space can be linked to the type of wind turbine considered in this work (i.e., NREL Phase VI) combined with the Rayleigh distribution used in the AEP calculation (Sec.4.2.4). In particular, the NREL Phase VI has its design condition at 10 $\mathrm{m/s}$; therefore, to reach the off-design regime at which tubercles work better, the wind speed must be close to 20 $\mathrm{m/s}$ for that specific wind turbine. Unfortunately, in the AEP calculation, the Rayleigh wind distribution gives more relevance to lower wind speeds (up to 15 $\mathrm{m/s}$) – considered more realistic values – rather than very high wind speeds such as 20 $\mathrm{m/s}$ (Fig.4.22). This means that in the AEP calculation for the NREL Phase VI blade, the shaft torque improvement reached in the off-design condition is penalized and considered less relevant than the degradation at 10 $\mathrm{m/s}$. The Rayleigh probability function gives a reasonable approximation of the wind distribution, because it is centered to low wind speeds considered more realistic conditions; therefore, the main reason of the AEP negative results is related to the specific wind turbine considered in this work (i.e., NREL Phase VI), and its design and off-design wind speed conditions.

5.3 One Design Variable DoE

The humpback whale flippers have a non-uniform distribution of tubercles, as visible in Fig.1.11; they start at around 33% of the span and are more concentrated close to the tip. An interesting question derives from this observation: does the position of tubercles along the blade span affect wind turbine performance? To answer this question, six tubercle locations are considered with non-dimensional amplitude and wavelength fixed at 0.0144 and 0.0191, respectively (corresponding to Case 7 in the DoE in Sec.5.2). In particular,

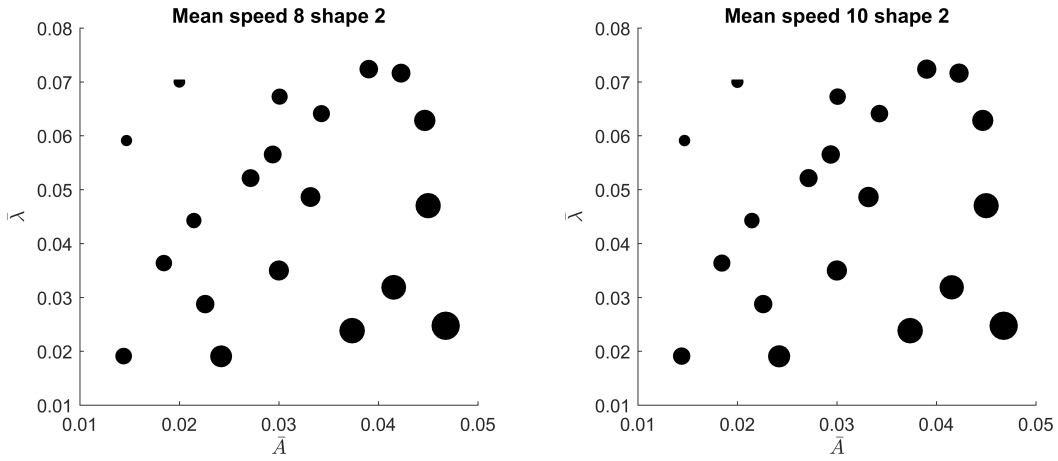

(a) $\overline{U} = 8\ \mathrm{m/s}$ (b) $\overline{U} = 10\ \mathrm{m/s}$

(c) $\overline{U} = 16\ \mathrm{m/s}$ (d) $\overline{U} = 20\ \mathrm{m/s}$

Figure 5.11: $\overline{\Delta \mathrm{AEP}}$ improvement.

six blades are tested with different non-dimensional starting spanwise location $\bar{z_0}$ (Fig.4.9, Sec.4.2.2): 0.4, 0.51, 0.62, 0.74, 0.85, and 0.95. The six blades generated are represented in Fig.5.12.

In Fig.5.13, CFD results are compared with the regular NREL and with the full-blade tubercle configuration, which is the baseline blade with tubercles on the entire span. In terms of shaft torque, there is a similarity in trends found in Sec.5.2: tubercles improve performance in the off-design condition, meaning very high wind speeds (20 $\mathrm{m/s}$), but they have negative effects with movement toward the design point (10 $\mathrm{m/s}$). This observation is correct for all the blades tested except for Case 6, which shows a positive peak at 10 $\mathrm{m/s}$ and similar values to the regular blade at the other wind speeds. As described in Sec.5.2, there are two main phenomena affecting the performance of wind turbine blades with leading edge tubercles: spanwise flow blockage and tip vortex effect. To better understand these two phenomena, it is necessary to analyze limiting streamlines (Fig.5.14, Fig.5.21), and pressure distribution (Fig.5.15, Fig.5.22) on the blade surface.

The blockage effect is more relevant when the blade is fully stalled, meaning when a strong spanwise flow moves from the root to the blade tip. Therefore, since the NREL Phase VI blade has its design condition at 10 $\mathrm{m/s}$ of wind speed, it is necessary to reach 20 $\mathrm{m/s}$ to better capture tubercle effects. The limiting streamlines at 20 $\mathrm{m/s}$ (Fig.5.14) indicate a strong spanwise flow over the entire blade in all the tubercle configurations considered, but to better capture tubercle effects it is necessary to look at the static pressure distribution on the suction side of the blades (Fig.5.15). All the cases tested (except Case 6) are characterized by low pressure regions exactly where tubercles begin due to the immediate blockage of the spanwise flow. This leads to a positive effect in the shaft torque in the off-design condition, as shown in Fig.5.13. Conversely, Case 6 (Fig.5.15(h)) that has tubercles only at the tip does not exhibit a relevant spanwise flow blockage effect, resulting in a pressure distribution very similar to the regular wind turbine blade with an insignificant difference at the blade tip. This similarity is the reason that shaft torque values

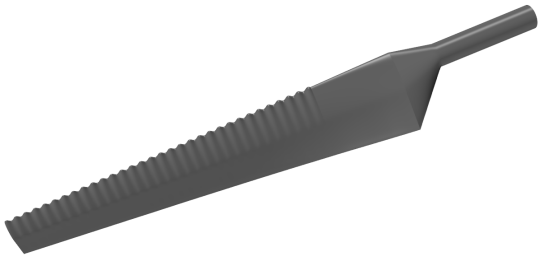

(a) Case 1: 40% of R

(b) Case 2: 51% of R

(c) Case 3: 62% of R

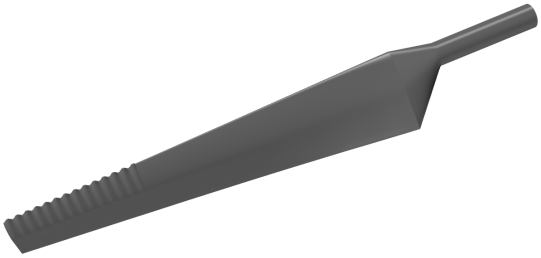

(d) Case 4: 74% of R

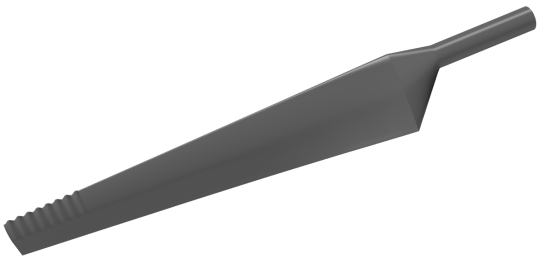

(e) Case 5: 85% of R

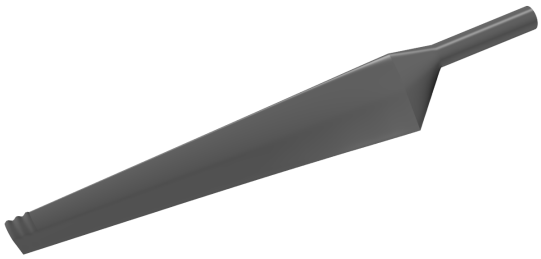

(f) Case 6: 95% of R

Figure 5.12: Tubercle configurations with different z_0.

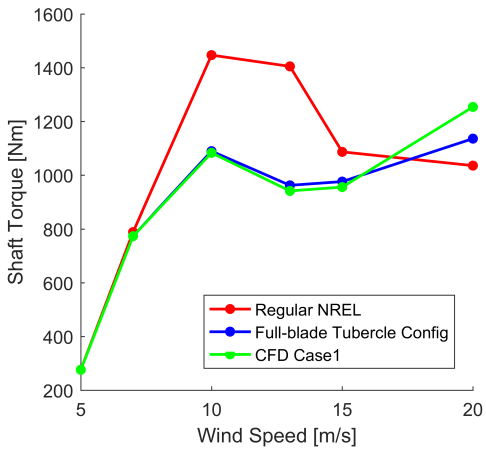

(a) Case 1: 40% of R

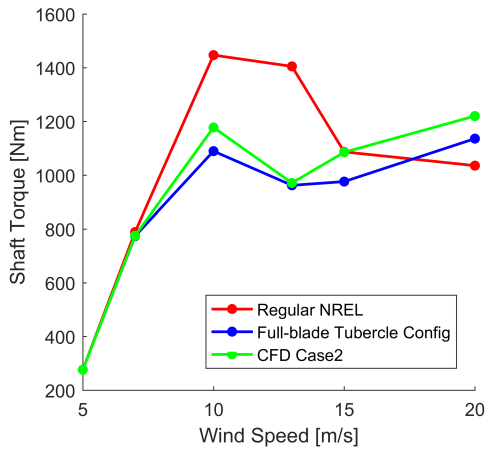

(b) Case 2: 51% of R

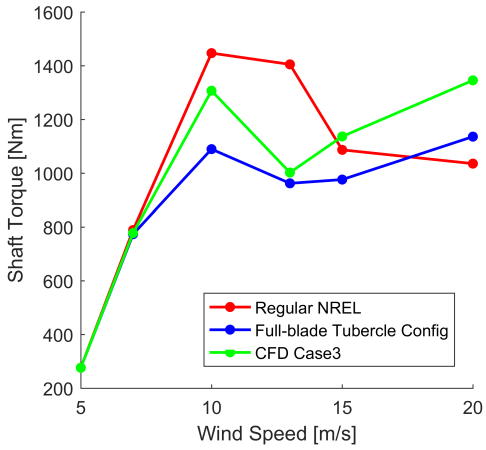

(c) Case 3: 62% of R

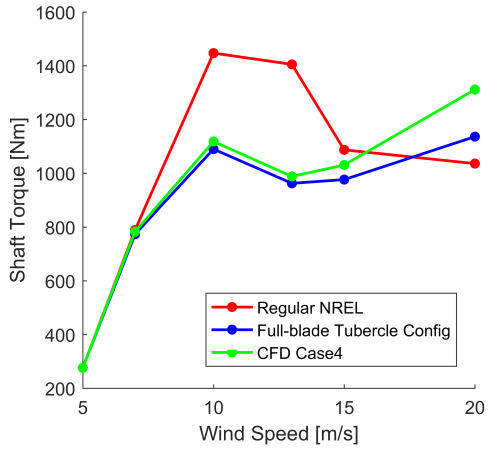

(d) Case 4: 74% of R

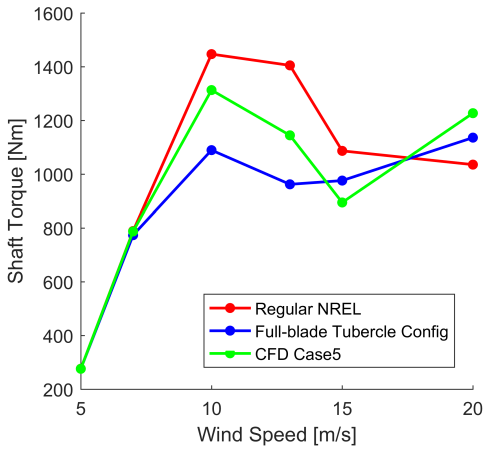

(e) Case 5: 85% of R

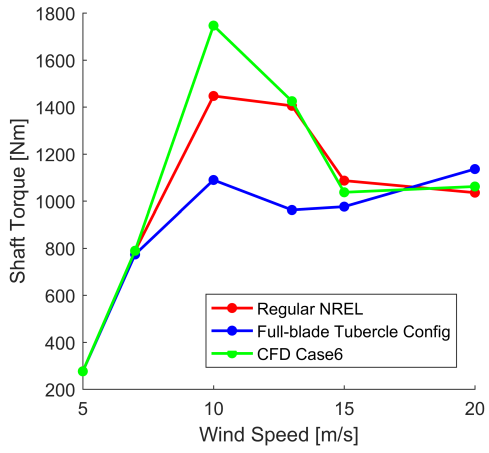

(f) Case 6: 95% of R

Figure 5.13: Shaft torque comparison between the regular NREL blade, the baseline tubercle configuration, and the six simulated blades.

for that specific case are very close to those of the baseline at high wind speed conditions (Fig.5.13(f)). A better visualization of blockage effects can be shown by plotting the spanwise flow at different blade sections (Fig.5.16−Fig.5.20). In particular, looking at the comparison between a representative tubercle configuration (Case 2) and the regular blade (Fig.5.16−Fig.5.20), tubercles have a strong effect on the spanwise flow immediately after the exact point where they are placed, and also at around 85−90% of the blade length. In Fig.5.16, there is a comparison between the cross-sectional spanwise flow of a representative CFD case (Case 2) and the regular NREL blade at the exact point where tubercles start (51% of blade length). The flow has a strong deceleration in Case 2 due to the presence of tubercles; after that point (Fig.5.17), the spanwise flow accelerates again until it has reached the 85−95% of the blade length (Fig.5.18, Fig.5.19), where the tubercle blockage effect appears again. Moving closer to the blade tip (Fig.5.20), the influence of tip vortex becomes stronger and more visible, negatively affecting the blockage effect. At lower wind speeds (e.g., 10 $\mathrm{m/s}$), the NREL Phase VI blade is at the design condition; therefore, the spanwise flow affects only a small portion of the blade root shown in Fig.5.21(a). In this case, the blockage effect results are less powerful and less visible compared to that in the off-design condition where the blade is fully stalled. The limiting streamlines in Fig.5.21 show that the presence of tubercles affects, in particular, the second half of the blade by generating counter-rotating vortices that perturb the original flow (Fig.5.21(a)). Moreover, when tubercles are placed between 51% and 62% of the span (Cases 2 and 3, Fig.5.21(d) and (e)), or close to the tip (Case 6, Fig.5.21(h)), the recirculation area on the first half of the blade disappears. Tubercle perturbation effects on the second half of the blade are more visible in the pressure distribution plotted in Fig.5.22. From the comparison with the baseline model, it is possible to observe that all the tubercle configurations except Case 6 show a higher pressure, especially in the area where tubercles start. Conversely, the presence of tubercles only at the tip (Case 6) positively affects flow (Fig.5.21(h)) and static pressure (Fig.5.15(h)) of the whole blade, resulting in a wider pressure area (Fig.5.15(h)).

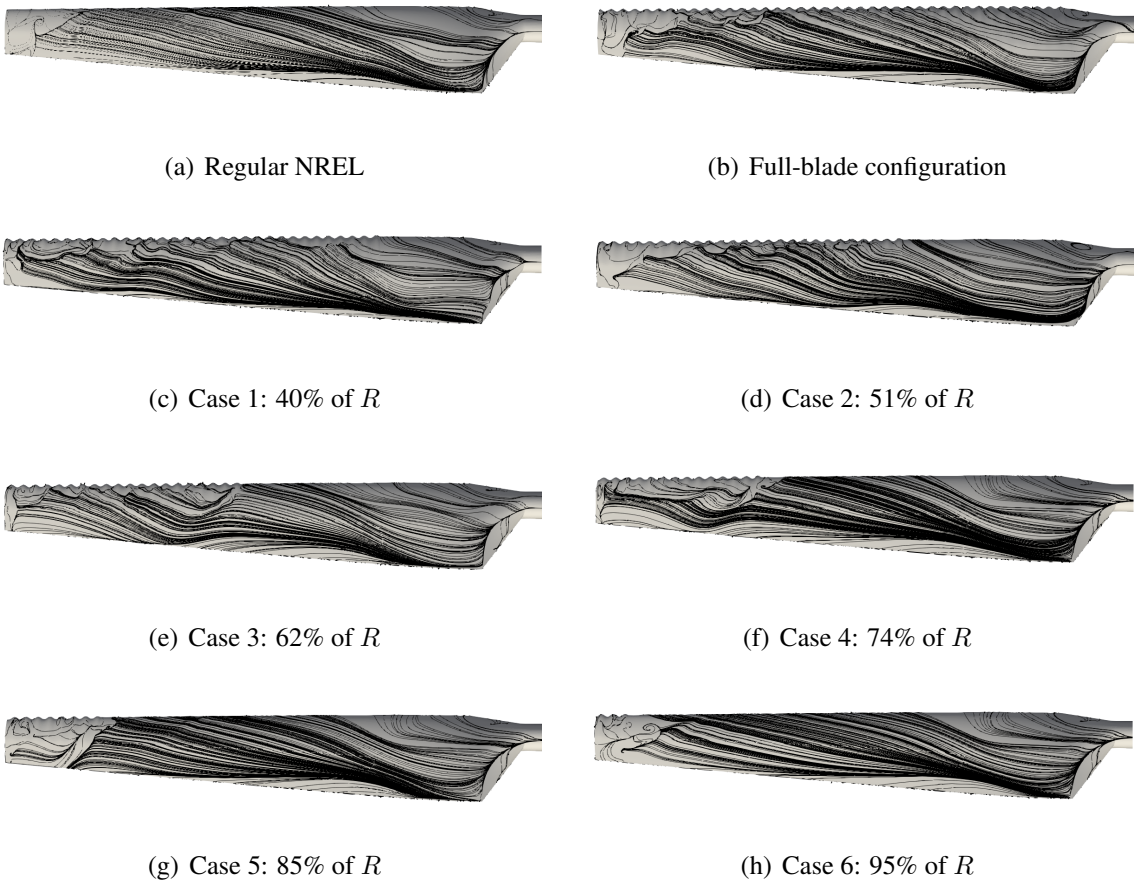

(a) Regular NREL

(b) Full-blade configuration

(c) Case 1: 40% of R

(d) Case 2: 51% of R

(e) Case 3: 62% of R

(f) Case 4: 74% of R

(g) Case 5: 85% of R

(h) Case 6: 95% of R

Figure 5.14: Limiting streamlines at 20 $\mathrm{m/s}$ of wind speed.

This effect seems to be related to the interaction between tubercles and tip vortex, which is also affected by the geometry of the last tubercle, as described in Sec.5.2.

From the AEP improvement point of view, $\overline{\Delta \mathrm{AEP}}$ (Sec.4.2.4) results are reported in Table 5.2, while plots in Fig.5.23 and Fig.5.24 compare the AEP of the regular NREL Phase VI blade (red line) with the AEP of the six cases tested in this work (black dots). Only Case 6 (tubercles only at the blade tip) shows an AEP improvement for all the mean wind speeds considered in the calculation, with a peak at 8 $\mathrm{m/s}$. These AEP results are completely different compared to those obtained in Sec.5.2, which shows only AEP degradation. This means that to reach an improvement in the annual energy production it is necessary to consider also the position of tubercles along the blade span, with particular attention to the second half of the blade and close to the blade tip. This aspect is investigated in the

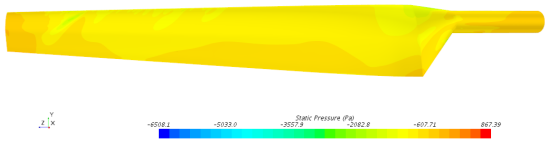

(a) NREL Phase VI

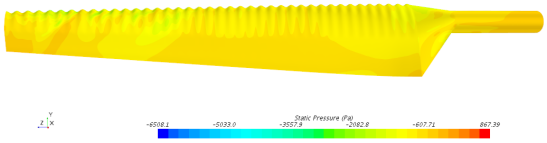

(b) Full-blade configuration

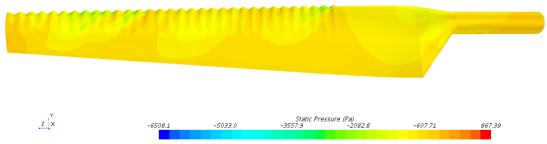

(c) Case 1: 40% of R

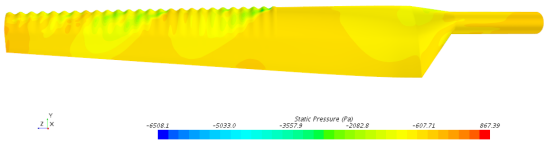

(d) Case 2: 51% of R

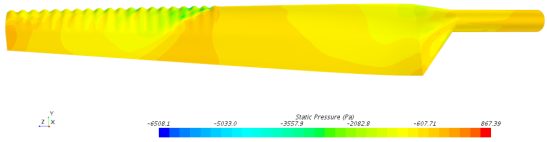

(e) Case 3: 62% of R

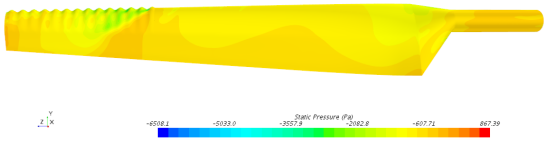

(f) Case 4: 74% of R

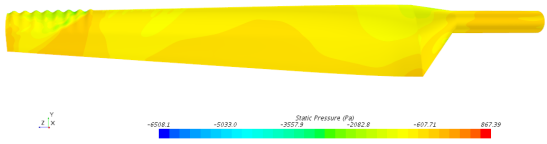

(g) Case 5: 85% of R

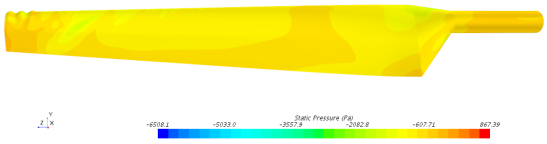

(h) Case 6: 95% of R

Figure 5.15: Static pressure on the suction side of the blades at 20 $\mathrm{m/s}$.

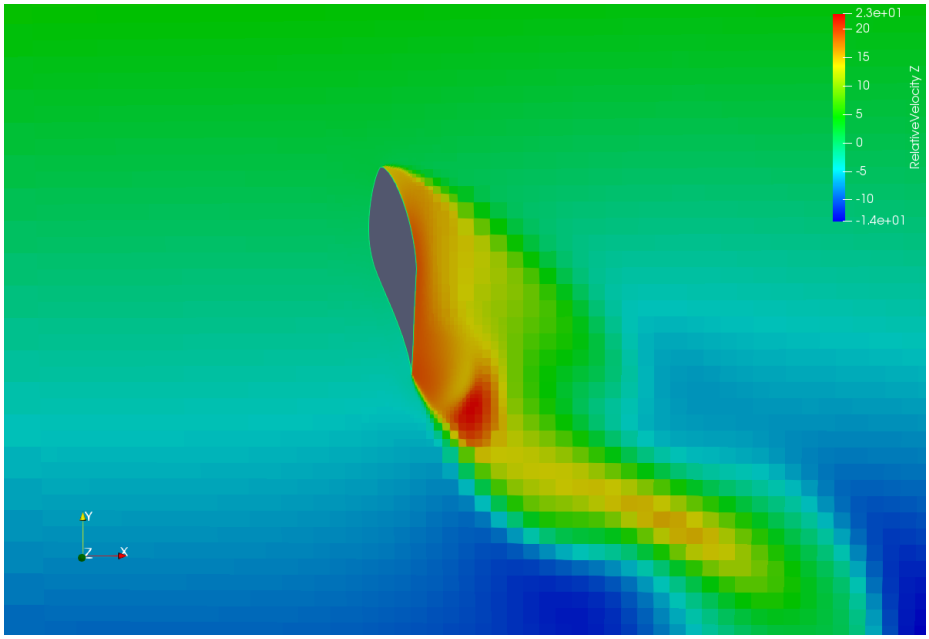

(a) NREL

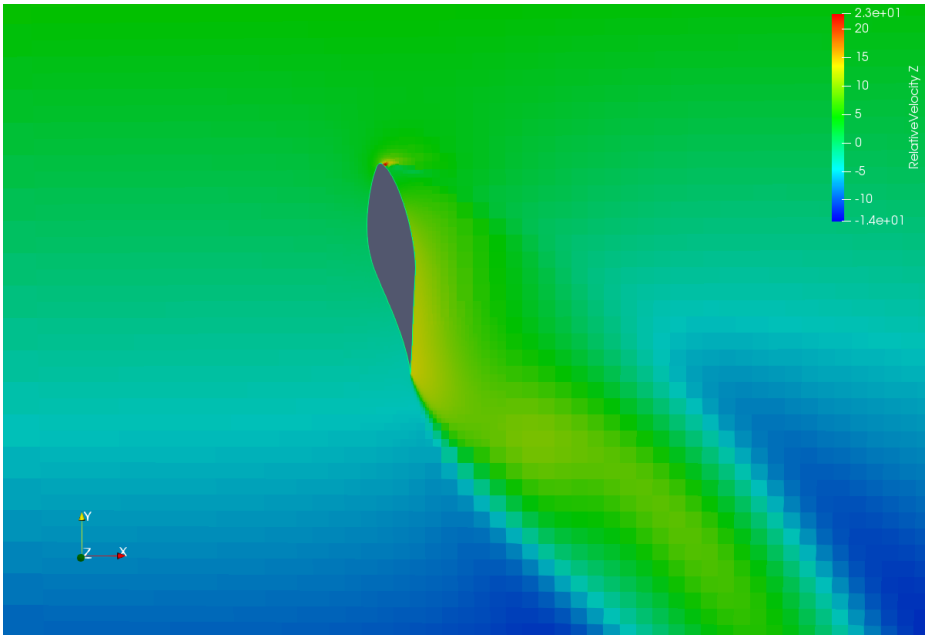

(b) Case 2

Figure 5.16: Cross-sectional spanwise flow at around 51% of blade length for a wind speed of 20 $\mathrm{m/s}$.

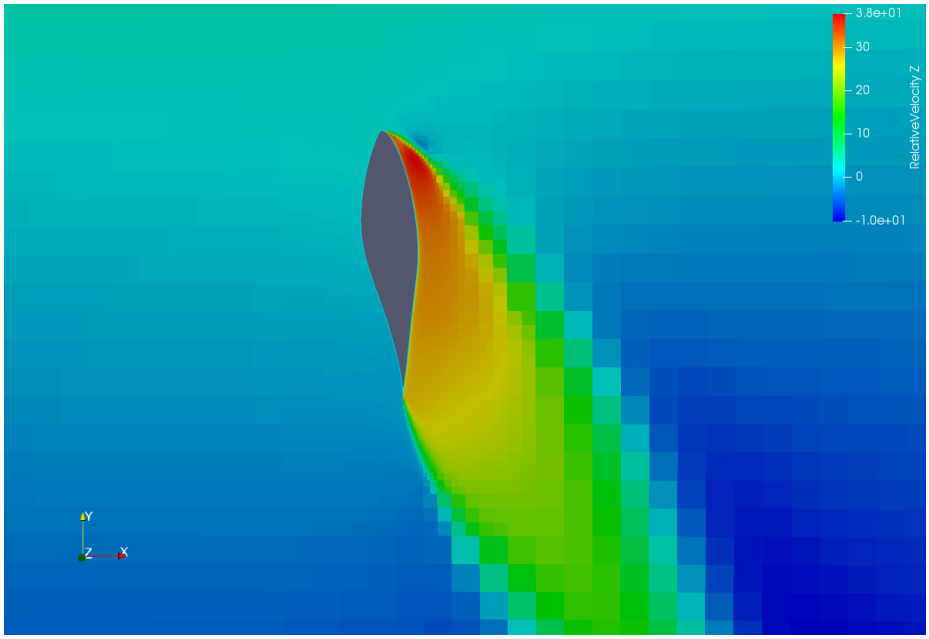

(a) NREL

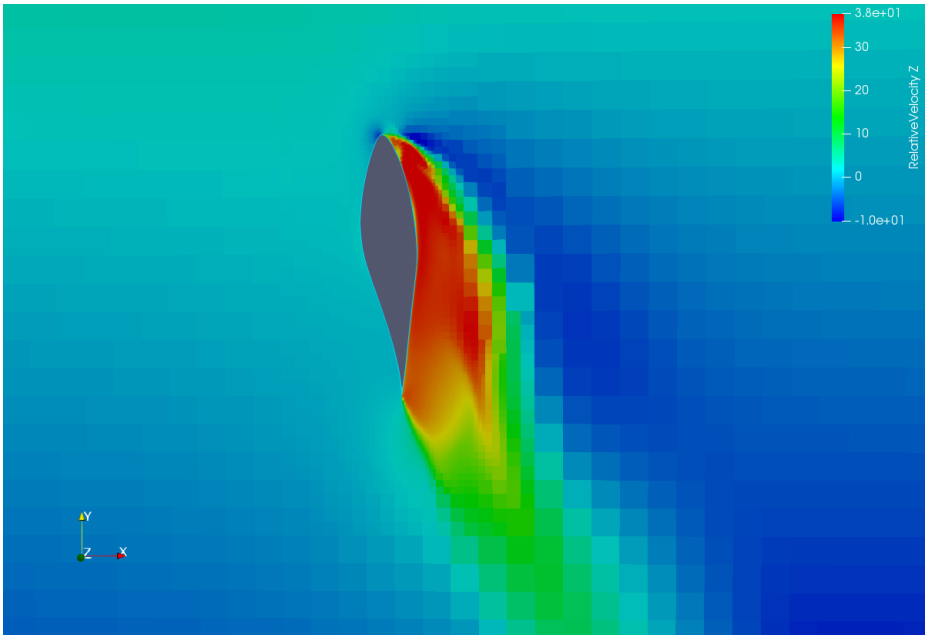

(b) Case 2

Figure 5.17: Cross-sectional spanwise flow at around 80% of blade length for a wind speed of 20 $\mathrm{m/s}$.

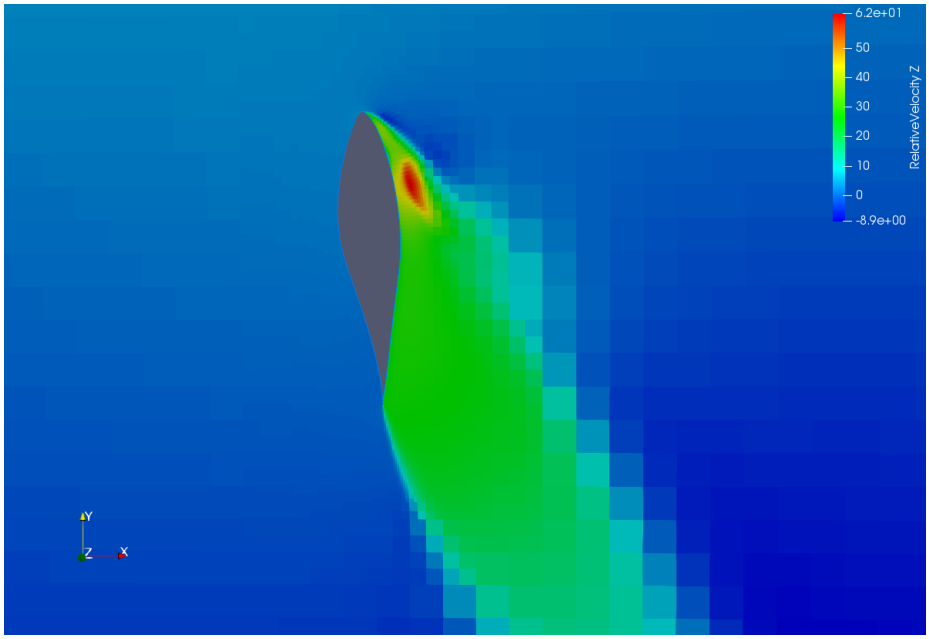

(a) NREL

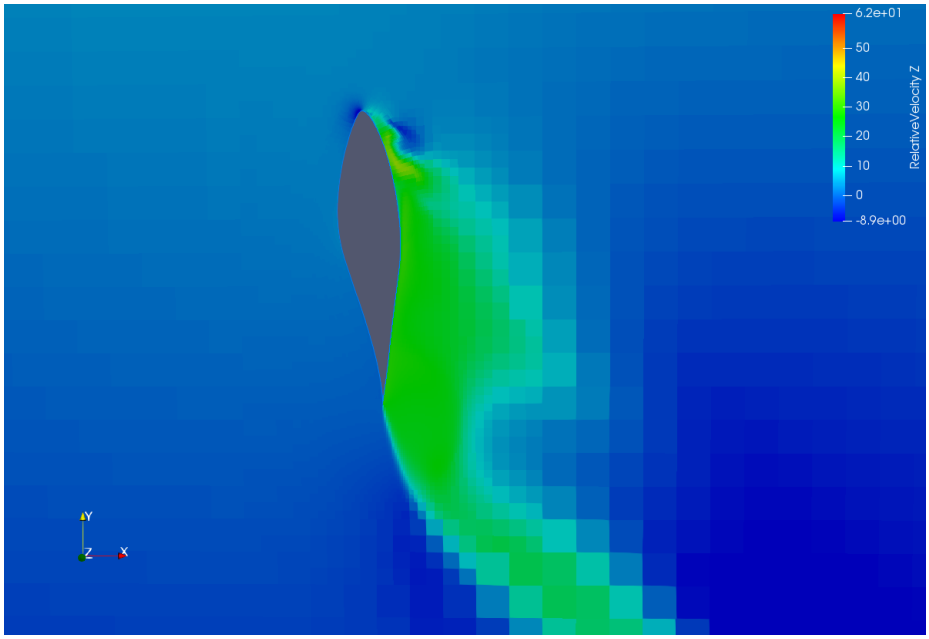

(b) Case 2

Figure 5.18: Cross-sectional spanwise flow at around 85% of blade length for a wind speed of 20 $\mathrm{m/s}$.

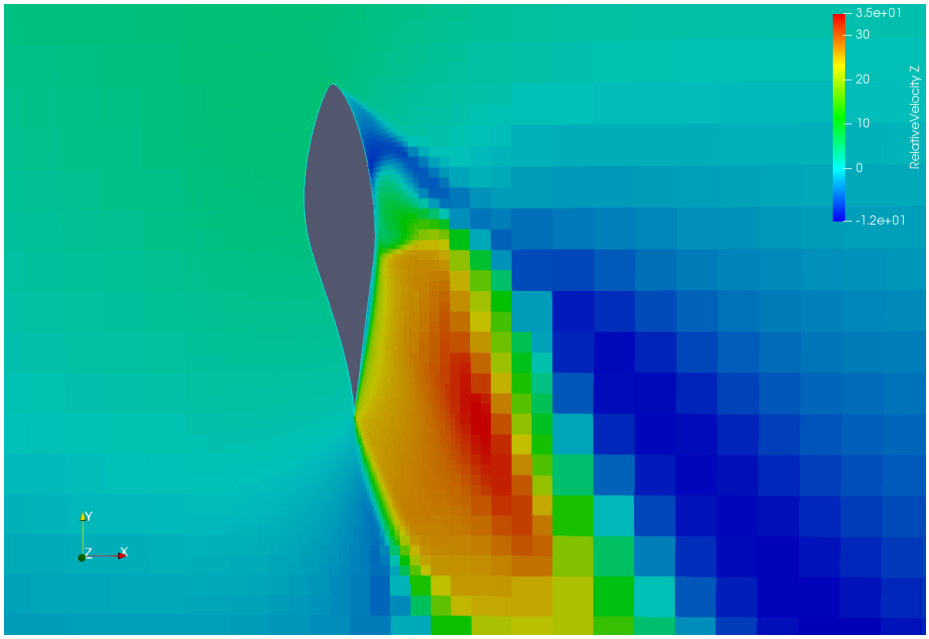

(a) NREL

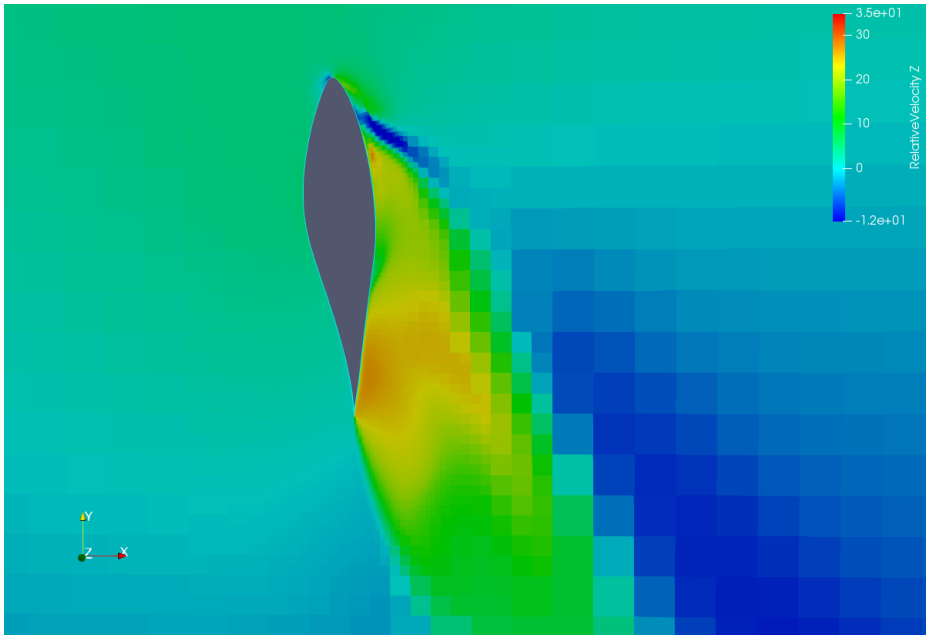

(b) Case 2

Figure 5.19: Cross-sectional spanwise flow at around 95% of blade length for a wind speed of 20 $\mathrm{m/s}$.

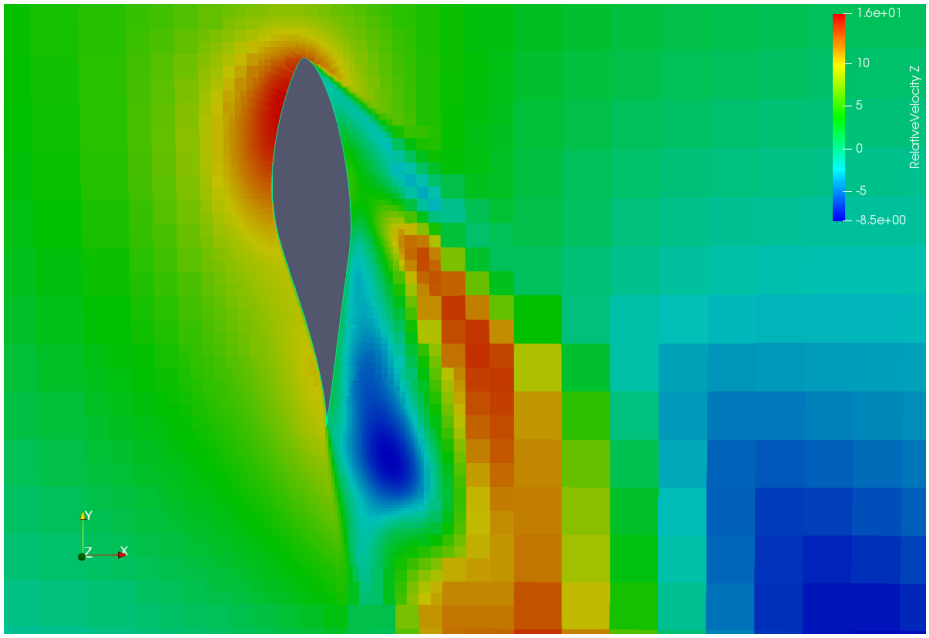

(a) NREL

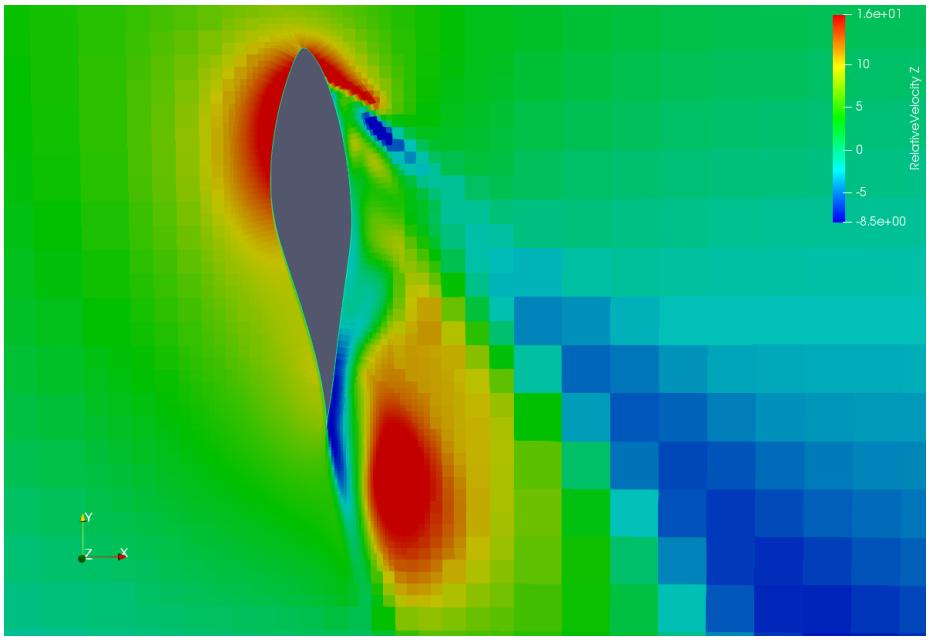

(b) Case 2

Figure 5.20: Cross-sectional spanwise flow close to the tip for a wind speed of 20 $\mathrm{m/s}$.

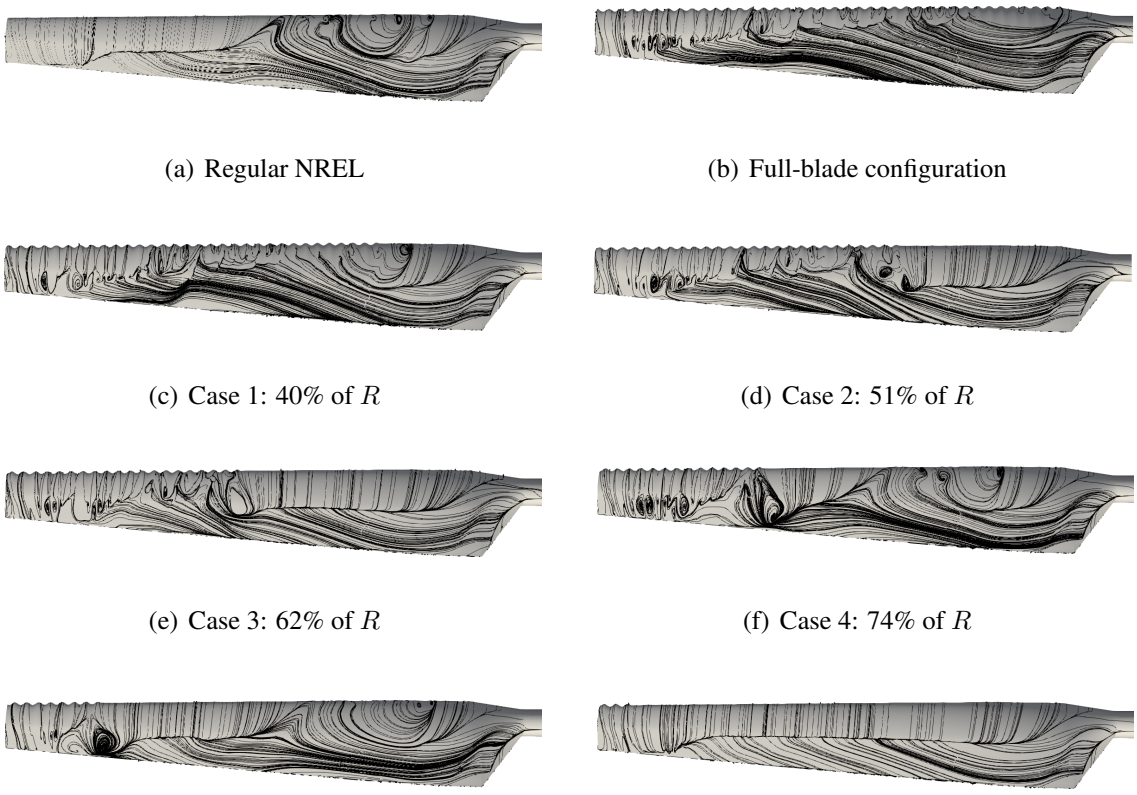

(a) Regular NREL

(b) Full-blade configuration

(c) Case 1: 40% of R

(d) Case 2: 51% of R

(e) Case 3: 62% of R

(f) Case 4: 74% of R

(g) Case 5: 85% of R

(h) Case 6: 95% of R

Figure 5.21: Limiting streamlines at 10 $\mathrm{m/s}$ of wind speed.

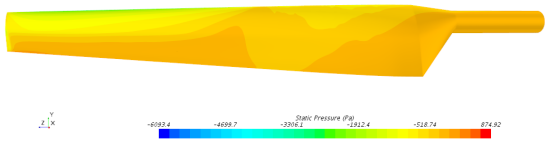

(a) NREL Phase VI

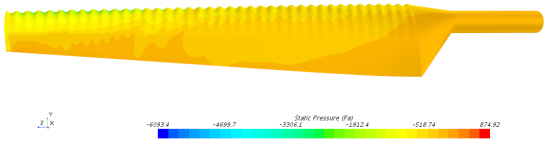

(b) Full-blade configuration

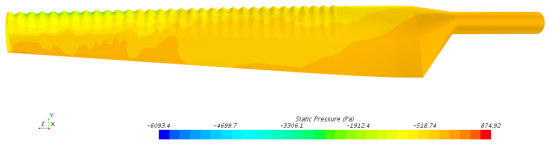

(c) Case 1: 40% of R

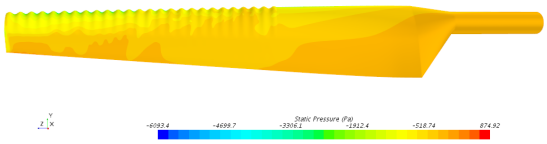

(d) Case 2: 51% of R

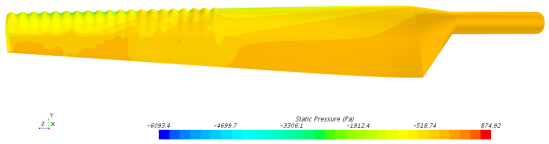

(e) Case 3: 62% of R

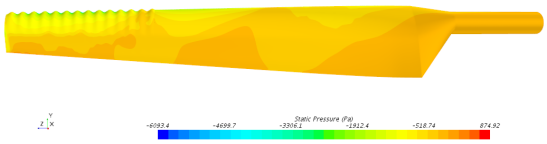

(f) Case 4: 74% of R

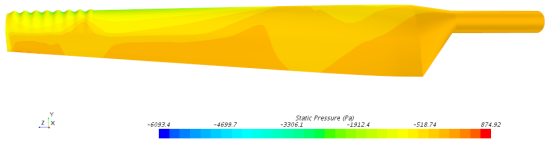

(g) Case 5: 85% of R

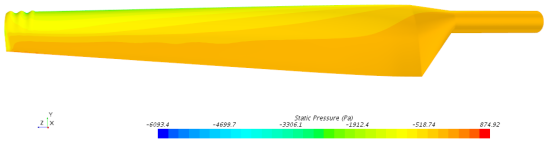

(h) Case 6: 95% of R

Figure 5.22: Static pressure on the suction side of the blades at 10 $\mathrm{m/s}$.

Table 5.2: $\overline{\Delta \text{AEP}}$.

$\overline{U}$ [m/s]	Full-blade Model	Case 1	Case 2	Case 3	Case 4	Case 5	Case 6
6	-0.1380	-0.1416	-0.1102	-0.0708	-0.1232	-0.0586	**0.0826**
8	-0.1707	-0.1753	-0.1322	-0.0847	-0.1488	-0.0858	**0.0848**
10	-0.1730	-0.1765	-0.1258	-0.0744	-0.1434	-0.0975	**0.0751**
12	-0.1671	-0.1687	-0.1135	-0.0594	-0.1310	-0.1015	**0.0665**
14	-0.1605	-0.1603	-0.1024	-0.0464	-0.1196	-0.1025	**0.0603**
16	-0.1549	-0.1533	-0.0936	-0.0363	-0.1105	-0.1023	**0.0559**
18	-0.1505	-0.1478	-0.0870	-0.0286	-0.1035	-0.1019	**0.0529**
20	-0.1470	-0.1435	-0.0819	-0.0228	-0.0982	-0.1013	**0.0507**

three design variable study (Sec.4.2.2) for which results are presented in the next section (Sec.5.4).

5.4 Three Design Variable DoE

It is interesting now to analyze the effects of tubercles when amplitude, wavelength, and spanwise location are considered as three design variables. In particular, as described in Sec.4.2.2, the non-dimensional starting spanwise location $\bar{z}_0$ in Sec.5.3 has been substituted by the number of tubercle peaks (N_{peaks}), which are counted starting from the blade tip since that area is considered the most influential in power production (Sec.5.3). Moreover, the blade geometries are generated such that each blade starts and ends with a peak to have comparable aerodynamic performance (Fig.5.25). The three design variables and their ranges are listed in Table 4.2, and the representations of the two DoEs used (Sec.4.2.2) are in Fig.4.11. Thirty cases are generated by a Latin hypercube DoE, and 27 more by a full factorial, resulting in a total of 57 tubercle configurations. In the following sections, results in terms of shaft torque and AEP will be presented with a surrogate model generation (Sec.4.2.5.2) to better capture performance trends in the design space considered.

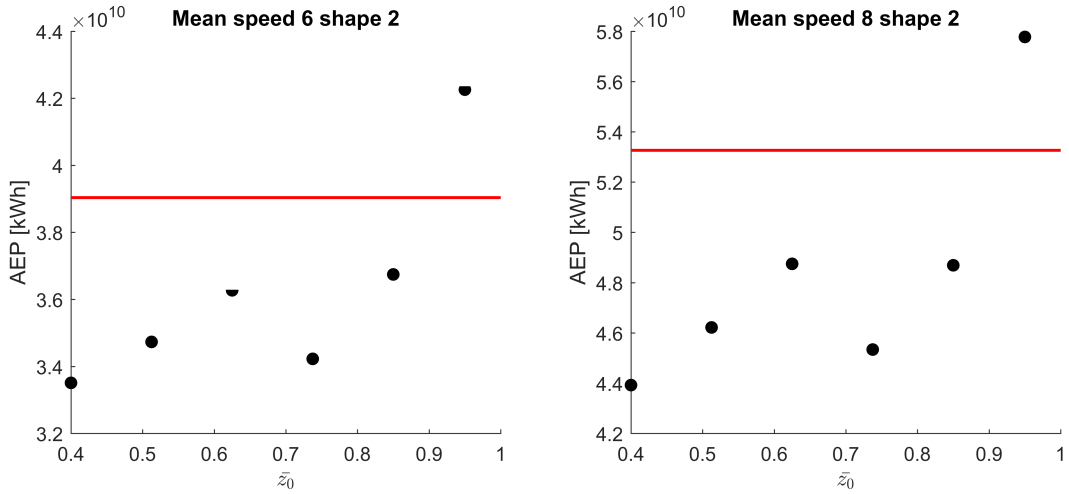

(a) $\overline{U} = 6\ \mathrm{m/s}$

(b) $\overline{U} = 8\ \mathrm{m/s}$

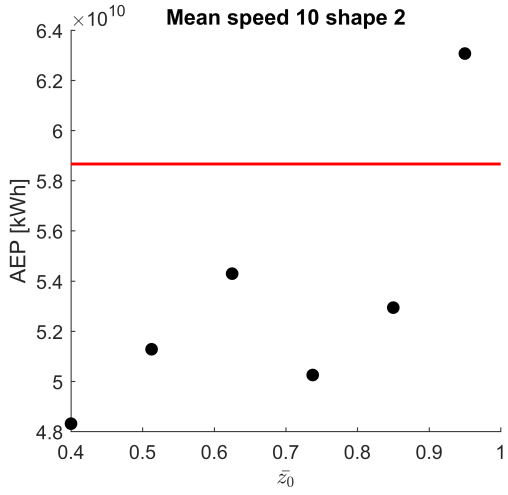

(c) $\overline{U} = 10\ \mathrm{m/s}$

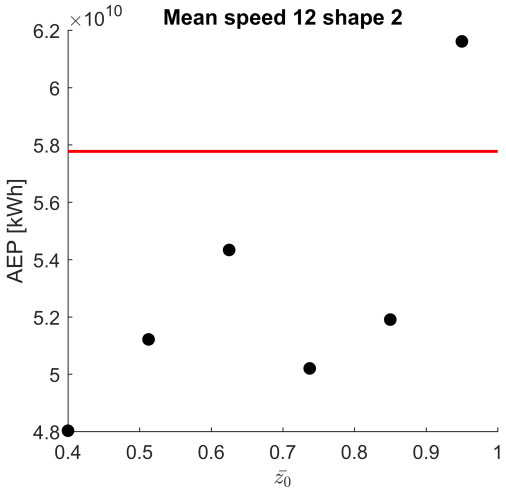

(d) $\overline{U} = 12\ \mathrm{m/s}$

Figure 5.23: AEP vs $\bar{z}_0$ for mean wind speeds of 6, 8, 10, and 12 $\mathrm{m/s}$.

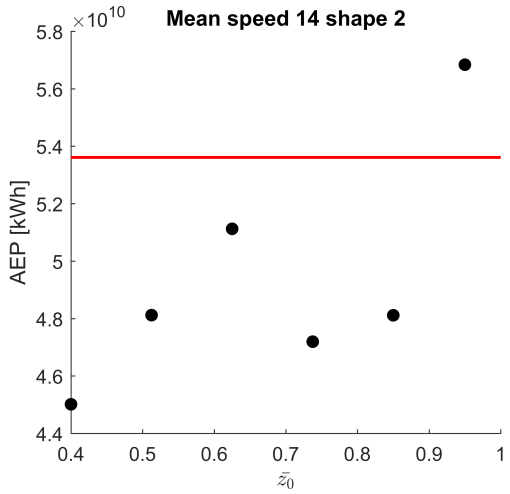

(a) $\overline{U} = 14\ \mathrm{m/s}$

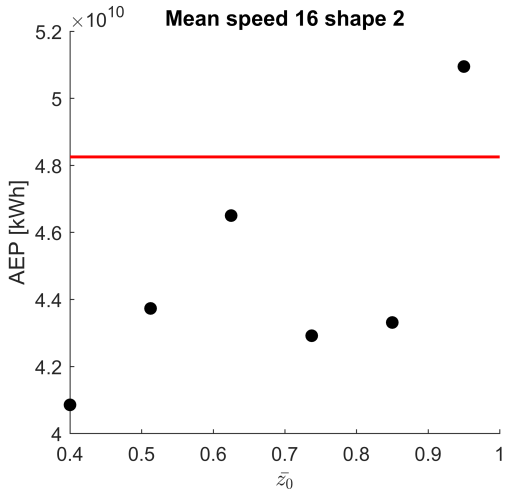

(b) $\overline{U} = 16\ \mathrm{m/s}$

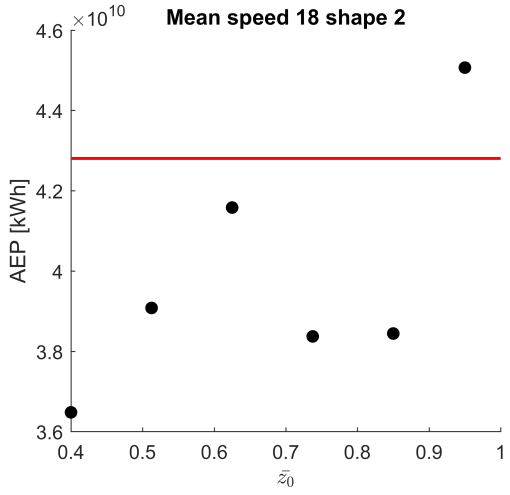

(c) $\overline{U} = 18\ \mathrm{m/s}$

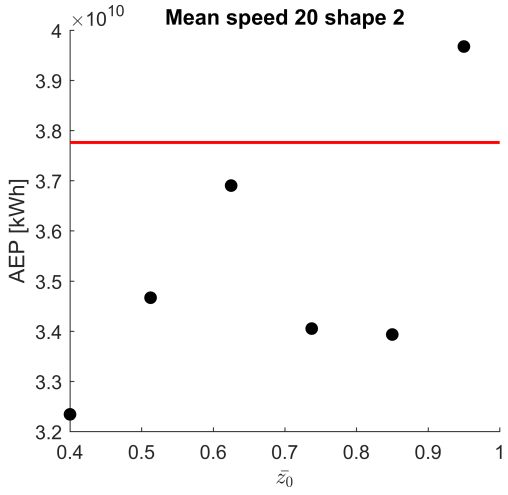

(d) $\overline{U} = 20\ \mathrm{m/s}$

Figure 5.24: AEP vs $\bar{z}_0$ for mean wind speeds of 14, 16, 18, and 20 $\mathrm{m/s}$.

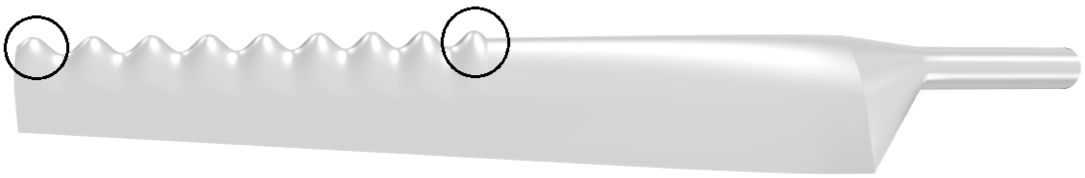

(a) Blade geometry example

(b) Detail of first tubercle

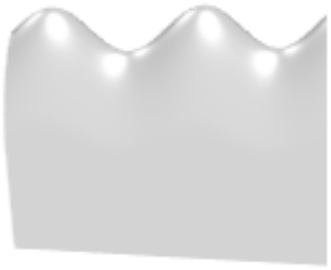

(c) Detail of last tubercle

Figure 5.25: Geometry of first and last tubercle.

5.4.1 Shaft Torque

The shaft torque of all 57 cases is represented in Fig.5.26 and Fig.5.27, where the same trends found in Sec.5.2 and Sec.5.3 are evident. All the tested blades show a shaft torque improvement in the off-design conditions (i.e., 20 $\mathrm{m/s}$) since tubercles affect the spanwise flow by blocking a portion of it and reducing the stall strength. Only a few tubercle configurations exhibit also a peak torque at 10 $\mathrm{m/s}$, and they correspond to blades with tubercles placed closer to the tip (as shown in Sec.5.3). Due to the scattered appearance of the collected data, a surrogate model has been created to better visualize the results across the entire design space. Therefore, as described in Sec.4.2.5.2, the 57 cases simulated by a CFD analysis are used as training points and five surrogate models are generated, depending on the wind speed considered (i.e., 7, 10, 13, 15, and 20 $\mathrm{m/s}$). The goodness of fit is evaluated in terms of R^2 and NRMSE (Sec.4.2.5.2), and the corresponding values for the five surrogate models are reported in Table 5.3. As described in Sec.4.2.5, R^2 values close to 1 and low NRMSE point out a good fit of the models. This result is also confirmed by looking at the plots representing actual versus predicted values (Fig.5.28(a)) and residual versus predicted values (Fig.5.28(b)) for a representative wind speed of 10 $\mathrm{m/s}$: they show the DoE cases (black dots) uniformly distributed close to the perfect fit line (red line) (Fig.5.28(a)), and in the residual versus predicted plot (Fig.5.28(b)), they are randomly scattered without having a particular pattern.

At this point, it is possible to analyze more generally the effects of tubercles on the NREL Phase VI blade aerodynamics and performance. Considering the same design variable ranges in Sec.5.4 and 50 points for each edge of the design space, the non-dimensional torque difference ($\overline{\Delta T}$) (Sec.4.2.5.2) can be predicted for each point by using the generated surrogate models. Moreover, by slicing the design space into five sections and plotting the resulting values, it is possible to visualize the evolution of $\overline{\Delta T}$. Contour plots of the predicted torque variation ($\overline{\Delta T}_{\text{pred}}$) are represented in Fig.5.29 for different values of the wind speed considered. These results confirm that the highest improvement in the shaft torque

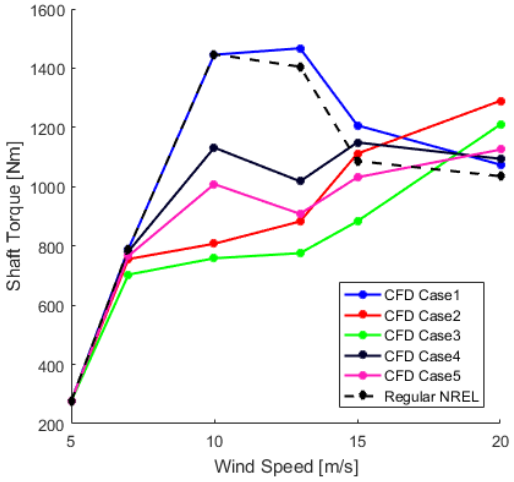

(a) Cases 1-5

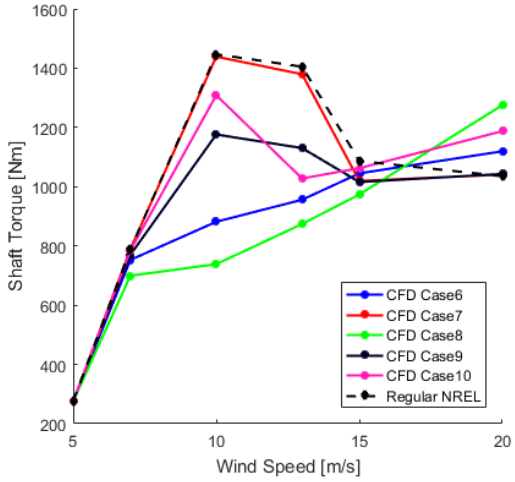

(b) Cases 6-10

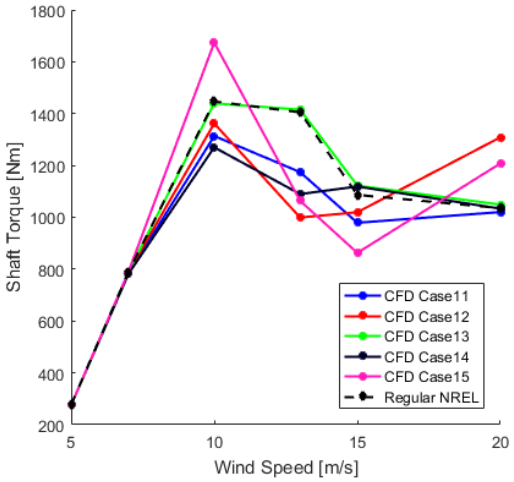

(c) Cases 11-15

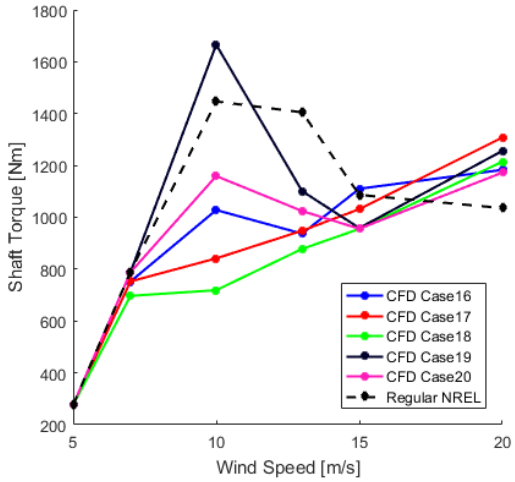

(d) Cases 16-20

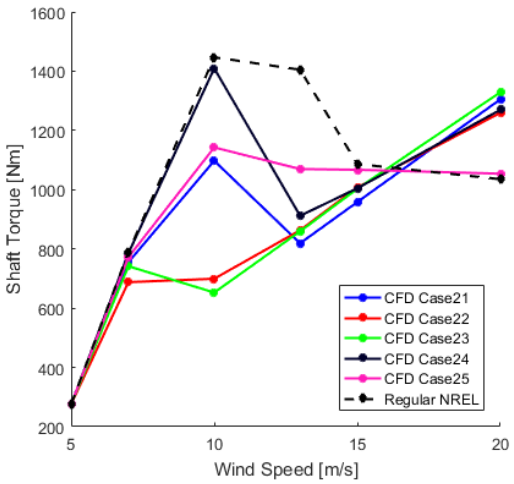

(e) Cases 21-25

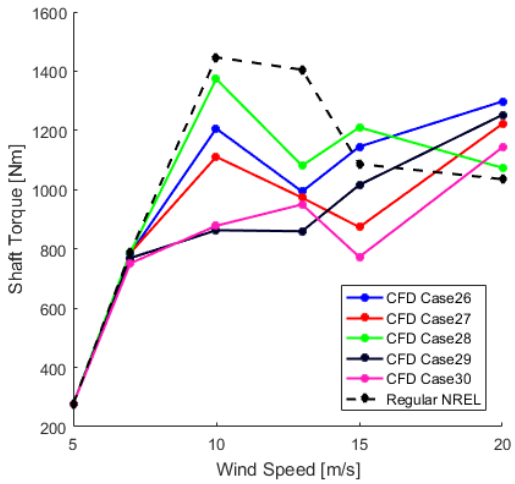

(f) Cases 26-30

Figure 5.26: Torque comparison for the Latin hypercube DoE.

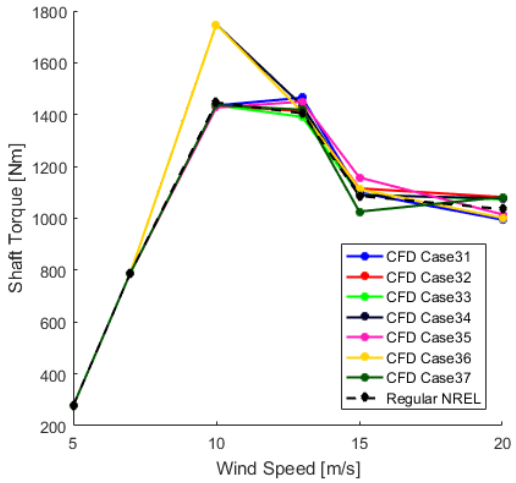

(a) Cases 31-37

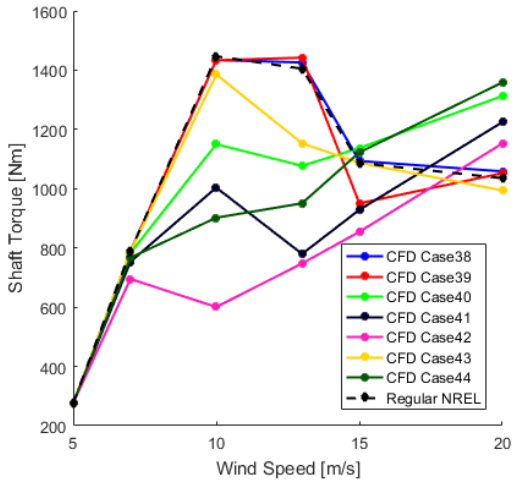

(b) Cases 38-44

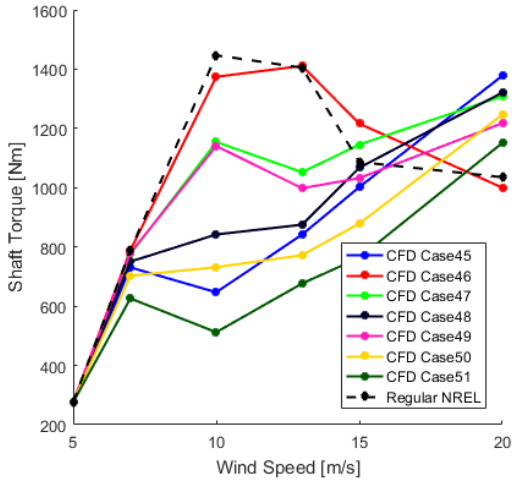

(c) Cases 45-51

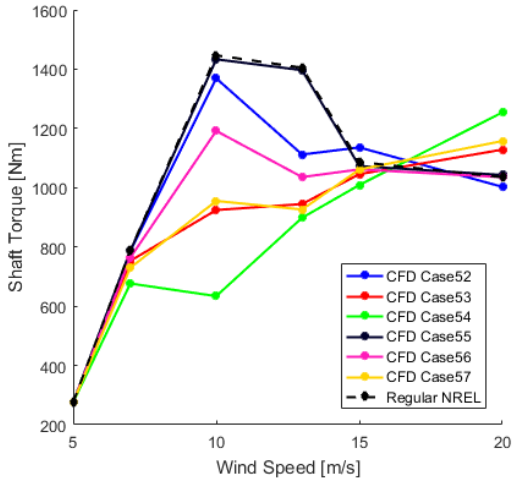

(d) Cases 52-57

Figure 5.27: Torque comparison for the full factorial DoE.

Table 5.3: R^2 and NRMSE values of the five surrogate models with three design variables.

Wind Speed	R^2	NRMSE
7	0.9960	0.0169
10	0.9127	0.0747
13	0.9714	0.0489
15	0.9261	0.0820
20	0.9137	0.0878

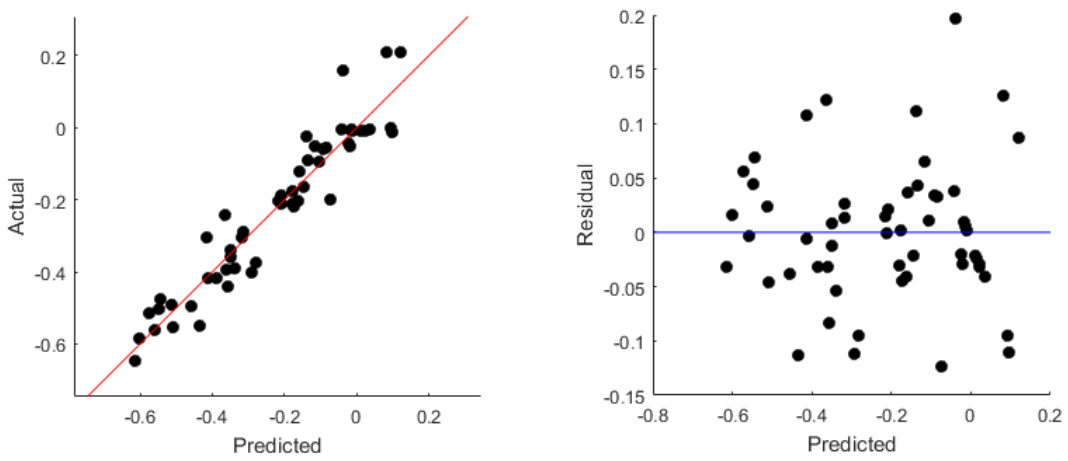

(a) Actual vs Predicted (b) Residual vs Predicted

Figure 5.28: Goodness of fit of the surrogate model considering 10 $\mathrm{m/s}$ of wind speed.

can be achieved in the off-design conditions (i.e., 20 $\mathrm{m/s}$) (Fig.5.29(e)) when the blade is fully stalled. Analyzing the plots in more detail in Fig.5.29, at 7 $\mathrm{m/s}$ the presence of tubercles does not positively affect the shaft torque, which actually decreases when the span coverage of tubercles goes beyond 50% and tubercle amplitude increases (Fig.5.29(a)). At 10 $\mathrm{m/s}$ (Fig.5.29(b)), the NREL Phase VI blade is on its design condition, showing a torque enhancement of 10% only when tubercle coverage is less than 20% of the span, and amplitude and wavelength fall in a defined area of the design space delimited by $\bar{\lambda}$ between 0.03 and 0.06. Degradation in performace reappears at 13 $\mathrm{m/s}$ (Fig.5.29(c)), probably because the blade is in a transitional region between the design and off-design conditions. Going beyond that wind speed and reaching 15 $\mathrm{m/s}$ (Fig.5.29(d)), again a region of torque improvement is evident, which becomes more defined with movement toward 20 $\mathrm{m/s}$ (Fig.5.29(e)) where the blade reaches the full stall condition. At this point, the positive effects of tubercles are visible, since the shaft torque increases up to 30% when high values of amplitude (between 0.03 and 0.05), wavelength within $0.02-0.04$, and a span coverage between 20% and 60% are considered. The shaft torque improvement trends at 10 and 20 $\mathrm{m/s}$ are apparent in the surface plots of $\overline{\Delta T}_{\text{pred}}$ in Fig.5.30 and Fig.5.31, respectively. Each

curve represents the shaft torque trend on each "slice" of the design space visualized in Fig.5.29(b) and Fig.5.29(e). These results confirm previous findings (Sec.5.3):

- in the off-design condition, tubercles are able to reach a high shaft torque improvement (30%) when placed on the second half of the blade, which is considered the most influential region in torque generation;
- at the design regime, it is reasonable to concentrate tubercles in a limited area close to the blade tip because the blade is already designed to work optimally at 10 $\mathrm{m/s}$, therefore, significant changes in the geometry can cause negative effects on performance;
- at the design condition, the spanwise flow does not exist and the only effect that tubercles can have on the blade aerodynamics is related to the tip vortex interaction.

5.4.2 Annual Energy Production

Annual energy production results are represented in Fig.5.32, where the non-dimensional AEP improvement ($\overline{\Delta\mathrm{AEP}}$) is plotted considering four different mean wind speeds: 8, 10, 16, and 20 $\mathrm{m/s}$. In these plots, the size of the dots represents the magnitude of $\overline{\Delta\mathrm{AEP}}$, and the color indicates a positive (red) or a negative (black) value. Therefore, as the figure shows, an AEP improvement has been achieved in a very limited area of the design space, and as mentioned in Sec.5.2, the reason for that is related to both the specific wind turbine considered in this work (i.e., NREL Phase VI) that has 10 $\mathrm{m/s}$ of wind speed as its design condition, and the Reyleigh wind distribution used for the AEP calculation. AEP results are reported in more detail in Appendix E.

It is important to understand in what area of the design space performance enhancement can be achieved; in particular, shaft torque is the most important parameter to consider since its values affect the computation of annual energy production (Sec.4.2.4). To visualize AEP trends in the design space, the $\overline{\Delta T}_{\text{pred}}$ found in Sec.5.4.1 are used to calculate the predicted

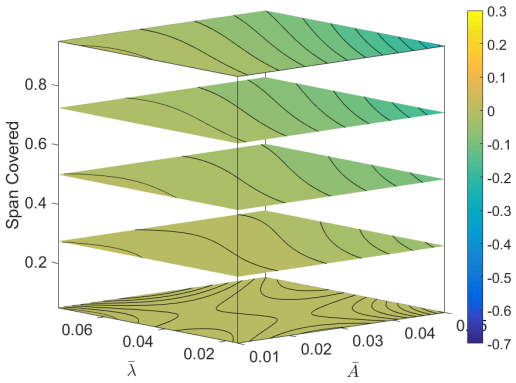

(a) 7 m/s

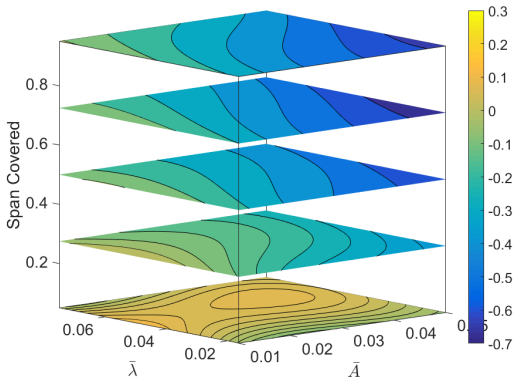

(b) 10 m/s

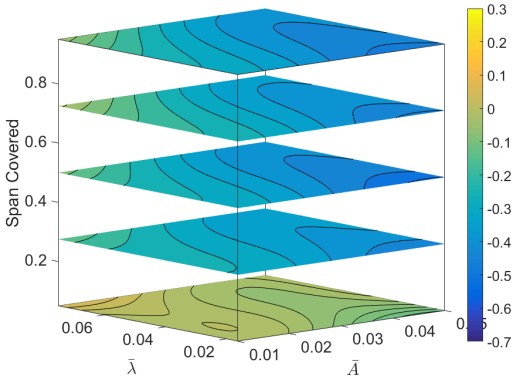

(c) 13 m/s

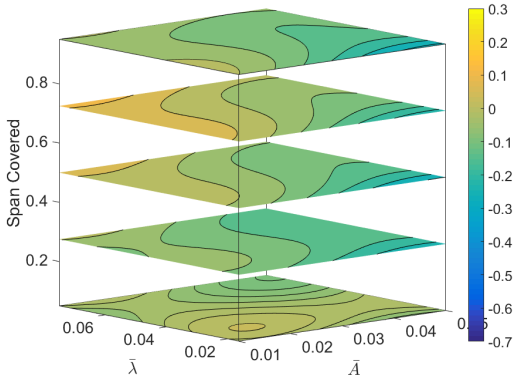

(d) 15 m/s

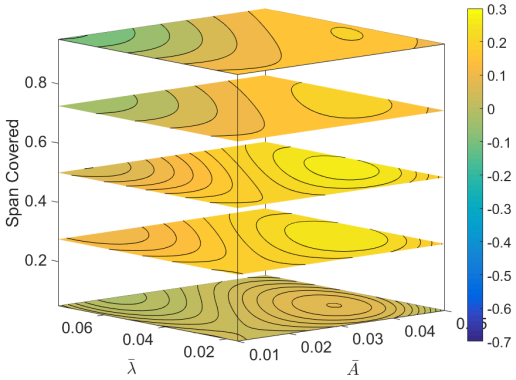

(e) 20 m/s

Figure 5.29: Contour plots of $\overline{\Delta T}_{\text{pred}}$ at different wind speeds.

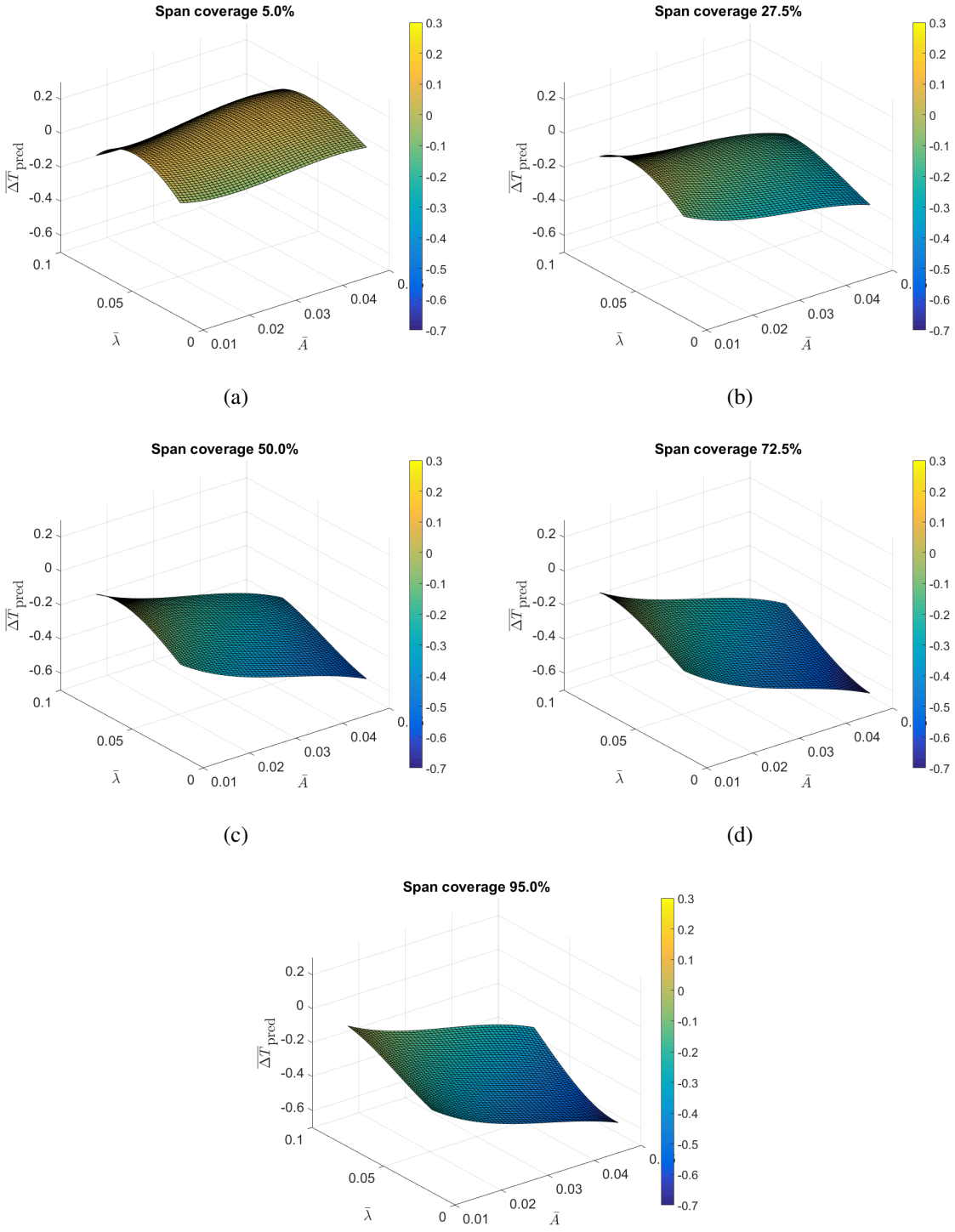

Figure 5.30: Surface plots of $\overline{\Delta T}_{\text{pred}}$ for a wind speed of 10 $\mathrm{m/s}$ at different sections of the design space.

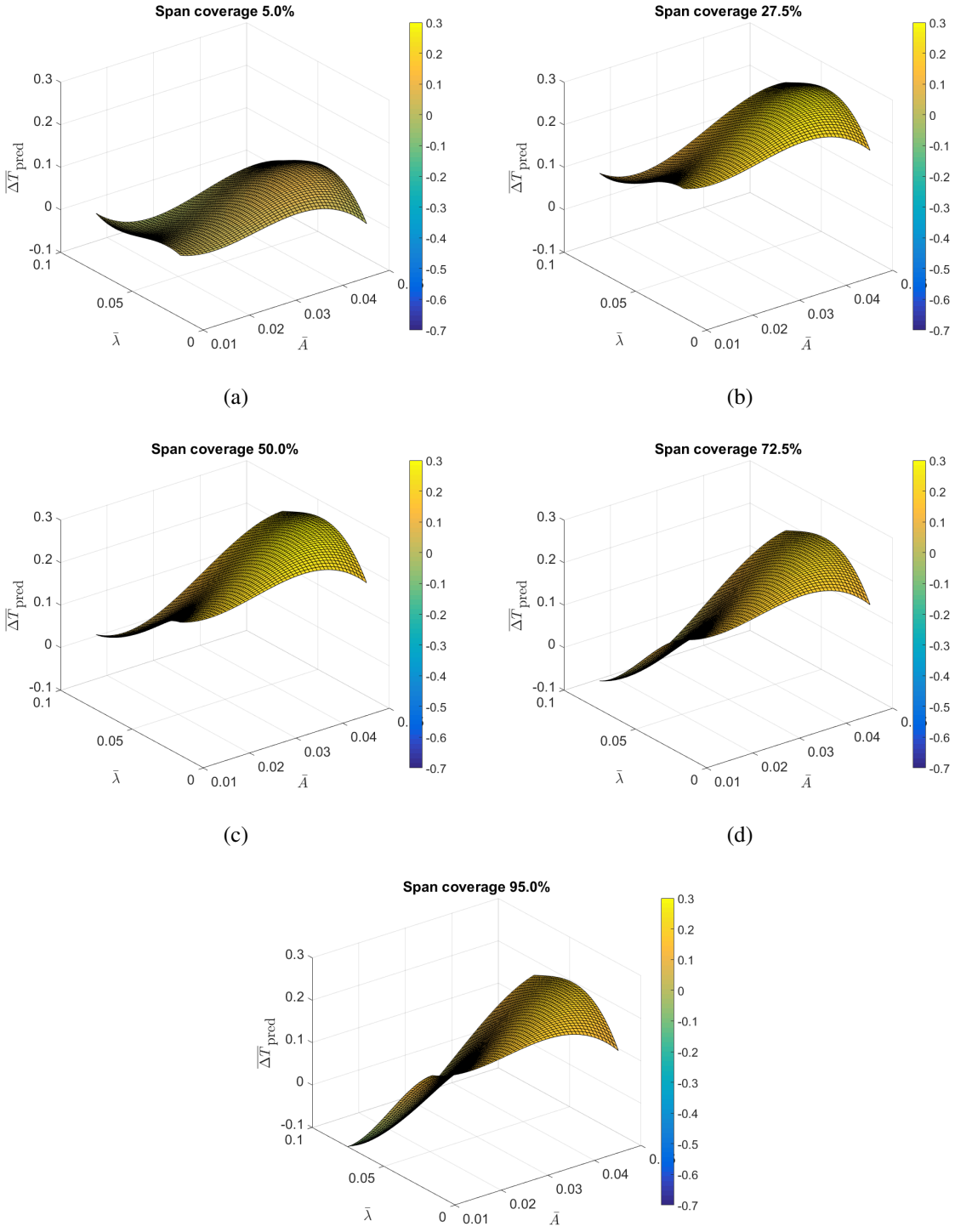

Figure 5.31: Surface plots of $\overline{\Delta T}_{\text{pred}}$ for a wind speed of 20 $\mathrm{m/s}$ at different sections of the design space.

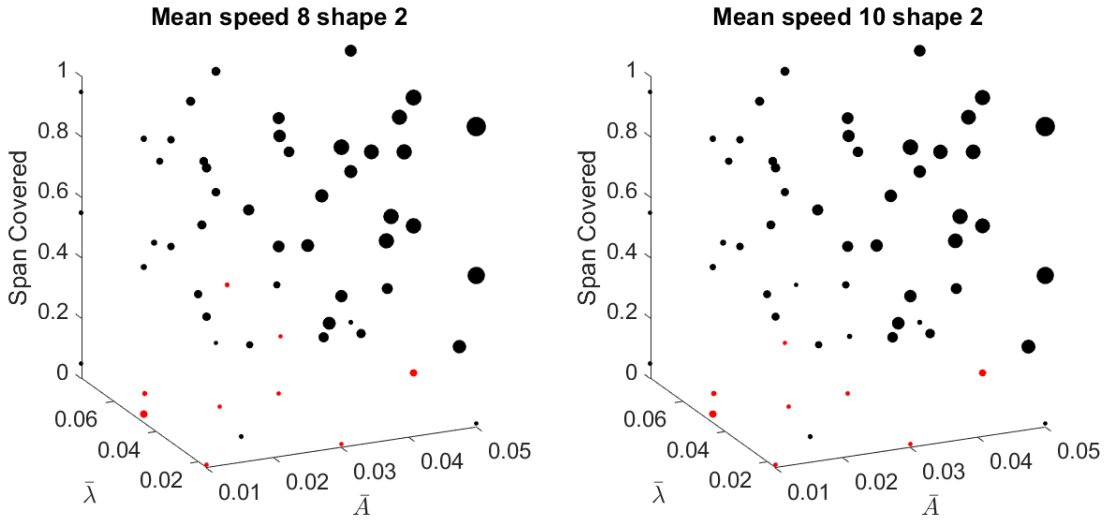

(a) $\overline{U} = 8$ m/s

(b) $\overline{U} = 10$ m/s

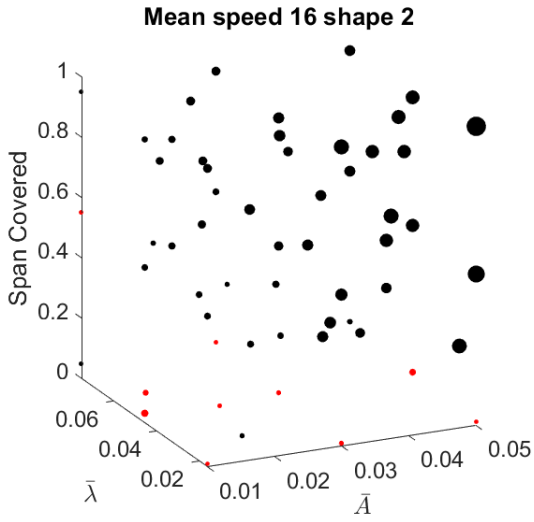

(c) $\overline{U} = 16$ m/s

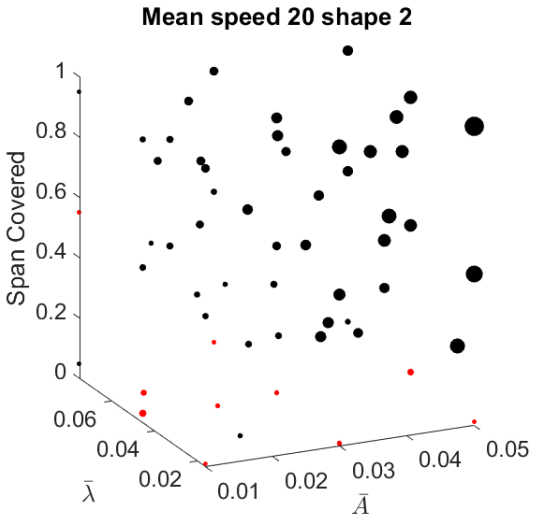

(d) $\overline{U} = 20$ m/s

Figure 5.32: $\overline{\Delta \text{AEP}}$ results at four different mean wind speeds.

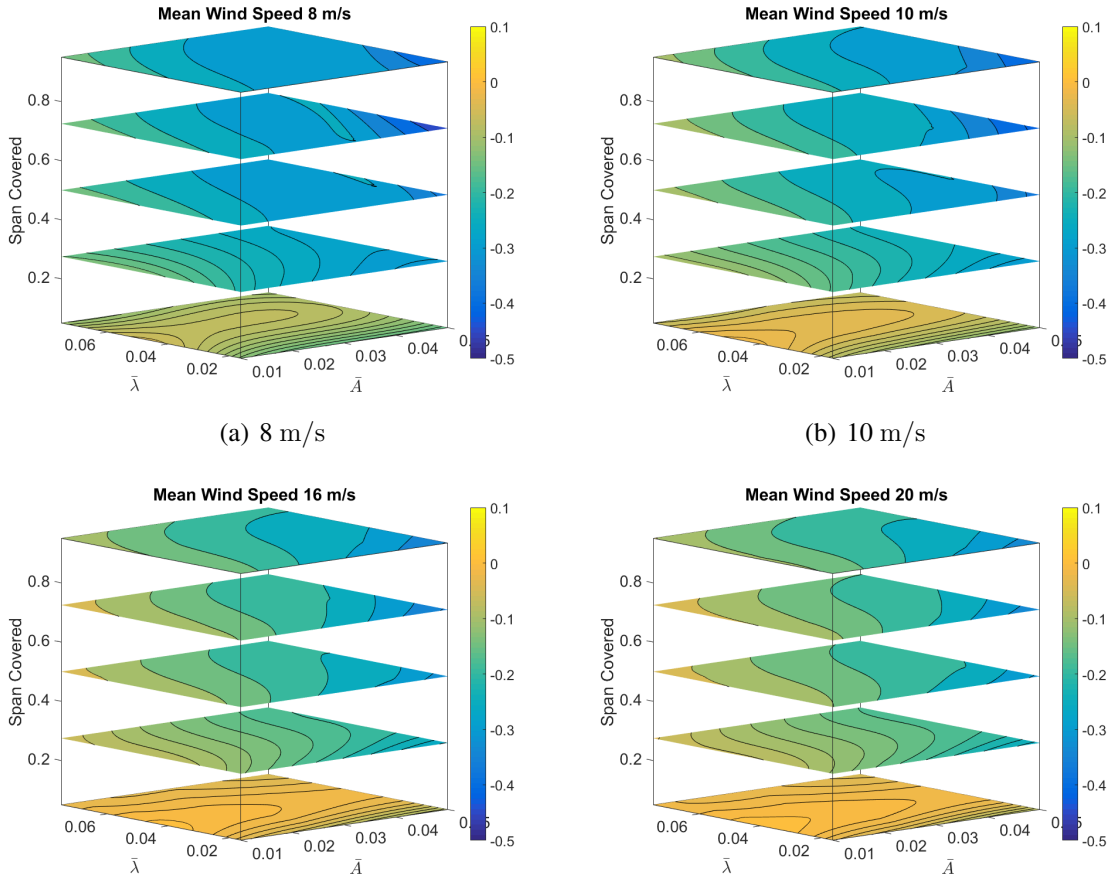

(a) 8 m/s

(b) 10 m/s

(c) 16 m/s

(d) 20 m/s

Figure 5.33: Contour plots of $\overline{\Delta \text{AEP}}_{\text{pred}}$ calculated at different mean wind speeds.

$\overline{\Delta \text{AEP}}$. Results are reported in contour plots (Fig.5.33), showing an AEP improvement for all the mean wind speeds above 8 $\mathrm{m/s}$ when tubercles are placed only at the tip (span coverage around 5%). As explained in Sec.5.2, the NREL Phase VI wind turbine has a design condition of 10 $\mathrm{m/s}$, which unfortunately, corresponds to the peak of the wind probability ditribution used for the AEP calculation (Fig.4.22). This means that shaft torque degradation, resulted at the design condition (i.e., 10 $\mathrm{m/s}$) is more relevant than the improvement in the off-design regime (i.e., 20 $\mathrm{m/s}$) due to the Rayleigh wind probability distribution (Fig.4.22) in the AEP calculation. Therefore, the positive effects of tubercles are limited in the annual energy production for the specific NREL Phase VI wind turbine.

5.5 Summary of the Results

Results in Sec.5.4 have been found using the NREL Phase VI blade as the baseline model, but they can be reasonably generalized by focusing the attention on tubercles' physical phenomena. Looking at the results in Sec.5.4.1 and considering the physical principles driving tubercle effects (i.e., spanwise flow blockage and tip vortex effect), it is possible to give insights into the application of tubercles on the leading edge of wind turbine blades. In particular, at the design condition (Fig.5.30), it has been discovered that tubercles have a relevant effects in power production when placed only close to the tip. The reasons of that are mainly two: first, the blade is already designed to optimally work at that wind speed, therefore, a relevant change in the geometry could have negative performance effects; second, there is no spanwise flow characterizing the blade at the design condition, therefore, the only effect that tubercles can have is linked to the interaction with the tip vortex.

In the off-design regime (Fig.5.31), tubercles always improve the wind turbine power generated, but it is possible to limit their position from midspan to the blade tip since that is the area providing more power production. Moreover, the blade is in a full stall condition and the strong spanwise flow going from the root to the tip can be blocked by tubercles (spanwise flow blockage effect), leading to stall strength reduction and aerodynamic performance improvement.

Comparing tubercle effects in the design and off-design regimes, it is noticible how leading edge bumps have more relevant effects when the blade is completely stalled due to the combination of both the spanwise flow blockage effect and the tip vortex interaction. Similar observations cannot be done for the annual energy production results because the AEP is strictly related to the wind turbine considered, its design condition, and the wind probability distribution used in the calculation, as demonstrated in Sec.5.2.

CHAPTER 6

CONCLUSIONS

The present work intends to study the effects on performance of sinusoidal modifications (i.e., tubercles) applied to the leading edge of wind turbine blades. Tubercles characterize humpback whale flippers and provide aerodynamic advantages by generating counter-rotating vortices that re-energize the boundary layer and delay flow separation. Since these same positive effects have been found in wing application, this study considers the use of tubercle technology also on wind turbine blades. In particular, the NREL Phase VI blade has been chosen as the baseline model since several experimental data are available in literature. The main objective of this work was to give insights into the application of tubercles on the leading edge of wind turbine blades such that performance enhancement can be achieved. To reach this result, three sub-objectives have been formulated with corresponding research questions and hypotheses.

6.1 Objectives and Results

The main research question of this work was:
What are the main aerodynamic effects of tubercles applied to wind turbine blades such that it is possible to achieve performance enhancement?
To answer this question, the work has been divided into three phases leading to three sub-objectives and the corresponding research questions and hypotheses.

Tubercles are characterized by two geometric parameters: amplitude and wavelength. How those parameters affect wind turbine perfomance has not been discovered yet; therefore, the first sub-objective of this work was to analyze amplitude and wavelength influence on shaft torque and annual energy production of the NREL Phase VI wind turbine. The re-

search question related to this first sub-objective was:

How do amplitude and wavelength of tubercles affect wind turbine performance?

A preliminary hypothesis has been formulated:

Specific values – at least ranges – of amplitude and wavelength exist such that wind turbine performance improvement can be reached.

To confirm or reject this hypothesis, an analysis of the effects of tubercle geometric parameters on wind turbine performance has been conducted. In particular, amplitude and wavelength have been considered as two design variables for the generation of a two-dimensional design of experiments able to identify 20 tubercle configurations to test by a three-dimensional CFD analysis.

Results showed that all the tested blades demonstrate shaft torque improvement in the off-design condition when the blade is fully stalled and the turbine typically becomes inefficient. To understand the reason for this positive result, a physical analysis of the phenomenon has been conducted. Previous research identified that leading edge tubercles generate counter-rotating vortices able to re-energize the boundary layer, leading to a flow separation delay. In the physical analysis conducted in the present work, the generation of counter-rotating vortices has been confirmed; moreover, two other main tubercle effects have been identified: spanwise flow blockage and tip vortex effect. In the off-design regime, the blade is fully stalled and a strong spanwise flow characterizes its surface; at this condition, vortices generated by tubercles are able to block a portion of the spanwise flow, resulting in a stall strength reduction. This effect is the main reason that blades with tubercles improve the shaft torque at high wind speeds (i.e., off-design conditions). Another tubercle effect on blade aerodynamics is the interaction with the tip vortex. It has been discovered that depending on the geometry of the last tubercle (i.e., ending with a peak or a trough) and, therefore, on the direction of the last counter-rotating vortex, the tip vortex strength can increase or decrease its intensity. An in-depth analysis on this interaction is necessary to

better understand the relationship between the last tubercle geometry and the tip vortex strength.

As mentioned in Sec.2.5.6, tubercles are usually compared to vortex generators since they generate counter-rotating vortices that help to delay flow separation. However, in view of what has been found in this work, tubercles can be considered also similar to boundary layer fences. As presented in Sec.2.5.4, boundary layer fences are small plates that wrap the blade surface to prevent the creation of spanwise flow. According to the observation outlined in Chapter 5, the counter-rotating vortices generated by tubercles act like a wall, blocking a portion of the spanwise flow and leading to a reduction in stall strength. Therefore, sinusoidal modifications placed at the leading edge of wind turbine blades can be considered a mix between two flow control devices: vortex generators, since they produce counter-rotating vortices, and boundary layer fences due to their effects on spanwise flow.

From the first phase of the present work, it has been discovered that tubercles improve shaft torque in off-design conditions as a result of the spanwise flow blockage effect. However, the same positive trend was not visible in the annual energy production, due to the specific wind turbine (i.e., NREL Phase VI) considered in this work. Indeed, the NREL Phase VI is designed to optimally work at 10 $\mathrm{m/s}$ of wind speed, which is a high wind value in the real world. Therefore, since tubercles work better in off-design conditions, it is necessary to reach very high wind speeds (i.e., 20 $\mathrm{m/s}$) to see positive relevant effects, but such high wind speed values are not common in the real life and for this reason, they are penalized by the wind probability distribution function (i.e., Rayleigh) used for the AEP calculation. This results in a negligible impact of the positive effects of tubercles in the annual energy production calculation.

Recalling the hypothesis formulated for the first research question, *Specific values – at least ranges – of amplitude and wavelength exist such that wind turbine performance improvement can be reached*, it was possible to recognize the difficulties in identifying

specific values of amplitude and wavelength that are able to improve wind turbine performance. However, using surrogate models generated from the 20 DoE cases, it was possible to identify a region in the design space where tubercles reach a power improvement up to 40%. This area is delimited by high values of amplitude ($0.045-0.05$) and low values of wavelength ($0.016-0.02$) considering a wind speed of 20 $\mathrm{m/s}$ (i.e., the off-design condition).

In the second phase of the present work, an investigation of the effects of only tubercle spanwise location has been conducted. As observed in previous studies (Sec.2.1), tubercles on whale flippers are unevenly distributed, with a greater concentration close to the tip. For this reason, it was interesting to analyze the performance of different tubercle configurations by changing the location of tubercles along the blade span and keeping fixed amplitude and wavelength. The research question formulated for this second sub-objective was:
How does tubercle spanwise location affect wind turbine performance?
The resulting hypothesis was:
Tubercle spanwise location will have relevant effects in wind turbine power improvement; in particular, tubercles located from midspan to the tip will have more positive effects since the second half of the blade is the most influential in the energy production.
To verify this hypothesis, amplitude and wavelength have been considered fixed and only tubercle spanwise location has been changed as a single design variable. The regular NREL blade has been divided into six sections representing six spanwise locations, and the resulting six blades have been simulated by a CFD software package. Five of six tubercle configurations showed a shaft torque improvement in the off-design regime, while the blade with tubercles only at the tip exhibited a positive peak torque at 10 $\mathrm{m/s}$ (i.e., the design condition) and similar values to the regular blade at higher wind speeds. This result is likely related to the fact that the NREL Phase VI is designed for a wind speed of 10 $\mathrm{m/s}$, and therefore a relevant change in the geometry can cause detrimental performance, as seen in five of the six tubercle configurations tested. On the other hand, placing sinusoidal modificati-

ons just at the tip permits an increase to the shaft torque even at design condition, probably because vortices generated by tubercles positively interact with the tip vortex. Based on the hypothesis previously formulated, it is possible to confirm the importance of tubercle spanwise location, and placing tubercles on the second half of the blade and, in particular, close to the tip has more relevant positive effects in the power generation than covering the entire blade span.

Once the importance of tubercle spanwise location has been discovered, the last phase of the work consisted in the performance analysis of amplitude, wavelength, and tubercle location together. The research question formulated to achieve this objective was:

What happens to turbine performance if amplitude, wavelength, and spanwise location are considered as three design variables?

and the corresponding hypothesis:

Considering amplitude, wavelength, and spanwise location as three design variables, it will be possible to identify a limited region in the design space where performance improvements can be achieved.

To demonstrate this hypothesis, a three-dimensional hybrid DoE (i.e., Latin hypercube + full factorial) has been used to generate 57 tubercle configurations. The single Latin hypercube was not able to sufficiently cover the areas of the design space close to the edges, therefore, a full factorial with three points per dimension has been added. Results revealed similar trends in shaft torque and AEP as those found in the first two phases of the study. A relevant increase in torque was visible in the off-design condition for all the blades tested, and only the geometries with tubercles just at the tip showed improvements also at 10 $\mathrm{m/s}$. CFD shaft torque results have been used as training points for surrogate model generation to identify performance trends in the design space considered. In particular, the shaft torque improvement has been evaluated by five surrogate models (one for each wind speed considered: 7, 10, 13, 15, and 20 $\mathrm{m/s}$) using a third order polynomial equation. Contour plots of the predicted shaft torque improvement showed an enhancement up to 10% at the design

condition when tubercles were placed only close to the tip, while by increasing the wind speed and reaching the off-design regime, a shaft torque increase up to 30% was reached when tubercles were placed on the second half of the blade between 20% and 60% of the blade span, and with values of non-dimensional amplitude between 0.03 and 0.05. From the predicted values of shaft torque resulting from the surrogate models, it was possible to calculate the annual energy production. Contour plots of non-dimensional AEP improvement showed that to reach an AEP enhancement of about 10% for any mean wind speed considered above 8 $\mathrm{m/s}$, it was necessary to place tubercles only close to the tip. Unlike what has been observed for the shaft torque, AEP results are strictly related to the NREL Phase VI wind turbine that reaches the off-design condition at 20 $\mathrm{m/s}$ of wind speed, which is considered a high value and is penalized by the Rayleigh probability distribution function used in the AEP calculation.

Based on the results described above, it was possible to get insights into the application of tubercles on the leading edge of wind turbine blades. In particular, it has been found that tubercles have two main aerodynamic effects: they block a portion of the spanwise flow when the blade is fully stalled (i.e, off-design condition), and affect the tip vortex strength. These two physical phenomena have a positive impact in the wind turbine power generation. At the design condition, the blade is characterized by an optimal geometry, and therefore, a relevant change in the shape by placing tubercles could have negative performance effects. For this reason, sinusoidal modifications must be placed in a limited blade area close to the tip such that they are able to positively affect the tip vortex without causing a significant change in the blade geometry. Moving toward the off-design regime, tubercles at the tip are still beneficial, but when the blade reaches a complete stall, they must be extended to the entire second half of the blade such that they can block a portion of the spanwise flow, leading to a reduction in stall strength and a shaft torque enhancement.

6.2 Conclusions and Recommendations

Research on tubercle application to wind turbine blades is very limited; therefore, the present study focused on providing more information on this new type of flow control device by giving physical decriptions of working principles and insights for wind turbine applications. The results obtained from the present study underline the important effects that tubercles have in the blade aerodynamics, especially in off-design regime, when the blade is fully stalled and the turbine is usually inefficient. Tubercles generate vortices able to block a portion of the strong spanwise flow characterizing the blade, resulting in a reduction of the stall strength, in an increase in the operative wind speed range, and in a power production improvement under difficult wind speed conditions. But wind turbines work at the design condition for most of the time, therefore, it is important to analyze and discuss also the positive effects that tubercles have when the blade works at design regime. It has been noticed that placing tubercles only close to the blade tip results in a positive peak in the power generation at the design wind condition due to their positive effects on the tip vortex strength.

In conclusion, the application of tubercles on the leading edge of the NREL Phase VI gives promising results in terms of power enhancement, but the question to ask is: why should I use tubercles rather than other flow control devices in wind turbine application? To answer this question, it is necessary to study more in-depth tubercles on wind turbine blades, analyzing also other aspects neglected in this work as noise, vibration, aeroelasticity, manufacturing, and cost. Based on an aerodynamic point of view, tubercles have the advantages of two of the flow control devices commonly used in wind turbine applications: vortex generators and boundary layer fences. They are able to generate counter-rotating vortices that affect the boundary layer and delay flow separation (similar to VGs), and at the same time when the blade is fully stalled, these vortices can block a portion of the spanwise flow (similar to boundary layer fences) leading to a stall strength reduction. An

interesting study to conduct could be related to a comparison between these three flow control devices focusing on different areas of interest (i.e., noise, vibration, aeroelasticity, manufacturing, and cost) to have a global view on tubercle pros and cons with respect to vortex generators and boundary layer fences.

The present work focused on the aerodynamic study and performance analysis of tubercles applied to wind turbine blades, leading to:

- a better understanding of the effects of tubercle geometric parameters (i.e., amplitude and wavelength) on wind turbine performance;
- an analysis of the influence of tubercle spanwise location by keeping fixed amplitude and wavelength;
- a study on performance effects given by three design variables: amplitude, wavelength, and tubercle spanwise location (or span coverage); and
- an analysis of physical phenomena behind the positive performance effects of tubercles.

A methodology incorporated in a simulation framework has been also developed to simulate wind turbine blades with tubercles, and to analyze the aerodynamics and the performance enhancement. The most difficult part of this work was related to the blade parametrization and the geometry generation. Due to several errors occurred when the CAD geometry file was imported in Star-CCM+ for the mesh creation (incompatibility issues), it has been decided to write a Matlab code for the generation of the STL geometry file. The second problem to deal with during the present study was related to the mesh creation. Due to the complexity of the blade geometries with tubercles, it was difficult to generate a smooth mesh close to the leading edge; therefore, it was necessary to change the mesh size values several times to achieve a satisfying result in terms of grid resolution required by the three-dimensional CFD simulations.

The present work is just a preliminary study on the application of tubercles on wind turbine blades. Their effects can be analyzed more in-depth by considering other aspects that have been neglected in this work. For example, an interesting study to conduct to complete the present research consists in the performance analysis when tubercle amplitude and wavelength are considered as a function of the spanwise location. It is well known that flow conditions over a wind turbine blade vary when moving from root to tip; therefore, the simplified assumption adopted in the present work to consider constant values of amplitude and wavelength along the blade span can be removed to analyze their variation effect on performance.

Another interesting aspect to investigate more in-depth is tubercle effect on tip vortex. In particular, as discovered in this research, the last tubercle geometry seems to influence the tip vortex strength. Depending if tubercles end with a peak or a trough, the direction of the resulting last counter-rotating vortex can affect differently the tip vortex strength. Therefore, a suggestion for future works is to compare the vorticity at the blade tip for different tubercle configurations that have the same amplitude and wavelength but that end differently (i.e., with a peak or a trough). From that analysis, it will be possible to study the interaction between the last counter-rotating vortex and the tip vortex.

Another extension of the present study could be to implement transient CFD simulations, such as detached eddy simulations (DES). They will be better able to capture the turbulent flow, leading to more accurate aerodynamic results; unfortunately, they will increase the computational time typically by 5 to 10 times.

Finally, the study of tubercles applied to wind turbine blades can be extended to other research areas than aerodynamics such as structures, aeroelasticity, and noise reduction.

Based on the results from previous research and the present work, it is difficult to draw conclusions about the impact that tubercles can have on the actual wind turbine market. There are a lot of missing aspects in the study on the positive effects that tubercles can have in wind turbine performance. For example, it could be interesting to analyze their

effects in modern multi-megawatt wind turbines (e.g., 2 MW and rotor diameter greater than 60 m) by conducting CFD analysis and wind tunnel tests. In case a pitch-regulated wind turbine is considered, it would be necessary to include some changes in the blade parametrization and tubercle implementation, thereby coupling the effects of both pitch control and tubercle technology as power control mechanisms. Finally, it is important also to analyze advantages and disadvantages of tubercles in the manufacturing process, and analyze their effects in other research areas as noise and vibrations, which are other two important problems to solve for wind turbines. By extending tubercle research, it will be possible to have a general view of their pros and cons in wind turbine application, resulting in a more clear idea of the impact that this technology can have in the wind energy field.

Appendices

APPENDIX A

TWO DESIGN VARIABLE DOE

The following table lists the non-dimensional amplitude and non-dimensional wavelength values of the 20 tubercle configurations generated by the two-dimensional DoE.

Table A.1: Two-dimensional DoE tubercle configurations.

Case	$\bar{A}$	$\bar{\lambda}$
1	0.0390	0.0724
2	0.0200	0.0700
3	0.0272	0.0521
4	0.0343	0.0641
5	0.0147	0.0591
6	0.0301	0.0673
7	0.0144	0.0191
8	0.0332	0.0486
9	0.0184	0.0364
10	0.0242	0.0191
11	0.0447	0.0628
12	0.0300	0.0350
13	0.0374	0.0238
14	0.0215	0.0443
15	0.0415	0.0319
16	0.0226	0.0288
17	0.0294	0.0565

18	0.0450	0.0470
19	0.0423	0.0716
20	0.0468	0.0247

APPENDIX B

ONE DESIGN VARIABLE DOE

The following table lists the non-dimensional starting spanwise location values of the 6 tubercle configurations generated by the one-dimensional DoE.

Table B.1: One-dimensional DoE tubercle configurations.

Case	$\bar{z}_0$
1	0.4000
2	0.5125
3	0.6250
4	0.7375
5	0.8500
6	0.9500

APPENDIX C

THREE DESIGN VARIABLE DOE

The following table lists the non-dimensional amplitude, non-dimensional wavelength, and number of tubercle peaks of the 57 tubercle configurations generated by the three-dimensional DoE.

Table C.1: Three-dimensional DoE tubercle configurations.

Case	$\bar{A}$	$\bar{\lambda}$	N_{peaks}
1	0.0133	0.0555	1
2	0.0404	0.0584	8
3	0.0392	0.0216	25
4	0.0255	0.0674	6
5	0.0212	0.0316	18
6	0.0329	0.0542	12
7	0.0162	0.0195	3
8	0.0369	0.0233	30
9	0.0263	0.0693	8
10	0.0102	0.0334	15
11	0.0171	0.0606	10
12	0.0240	0.0400	5
13	0.0183	0.0362	2
14	0.0146	0.0473	15
15	0.0325	0.0526	3
16	0.0407	0.0748	7

17	0.0292	0.0292	16
18	0.0496	0.0510	13
19	0.0283	0.0645	4
20	0.0433	0.0492	3
21	0.0426	0.0344	9
22	0.0466	0.0390	16
23	0.0454	0.0435	9
24	0.0349	0.0623	4
25	0.0233	0.0657	11
26	0.0121	0.0266	15
27	0.0361	0.0438	4
28	0.0197	0.0719	5
29	0.0313	0.0256	11
30	0.0477	0.0163	13
31	0.0100	0.0160	1
32	0.0300	0.0160	1
33	0.0500	0.0160	1
34	0.0100	0.0455	1
35	0.0300	0.0455	1
36	0.0500	0.0455	1
37	0.0100	0.0750	1
38	0.0300	0.0750	1
39	0.0500	0.0750	1
40	0.0100	0.0160	24
41	0.0300	0.0160	24
42	0.0500	0.0160	24
43	0.0100	0.0455	9

44	0.0300	0.0455	9
45	0.0500	0.0455	9
46	0.0100	0.0750	6
47	0.0300	0.0750	6
48	0.0500	0.0750	6
49	0.0100	0.0160	47
50	0.0300	0.0160	47
51	0.0500	0.0160	47
52	0.0100	0.0455	16
53	0.0300	0.0455	16
54	0.0500	0.0455	16
55	0.0100	0.0750	10
56	0.0300	0.0750	10
57	0.0500	0.0750	10

APPENDIX D

AEP RESULTS OF TWO DESIGN VARIABLE DOE

The following table lists the values of the design variables and the AEP results considering four mean wind speeds of the 20 tubercle configurations generated by the two-dimensional DoE.

Table D.1: $\overline{\Delta \text{AEP}}$ for different mean wind speeds

Case	$\bar{A}$	$\bar{\lambda}$	$\overline{U}$			
			8 m/s	10 m/s	16 m/s	20 m/s
1	0.0390	0.0724	-0.2024	-0.2022	-0.1811	-0.1728
2	0.0200	0.0700	-0.0882	-0.0924	-0.0858	-0.0822
3	0.0272	0.0521	-0.1904	-0.1843	-0.1537	-0.1428
4	0.0343	0.0641	-0.1788	-0.1754	-0.1508	-0.1415
5	0.0147	0.0591	-0.0812	-0.0798	-0.0650	-0.0593
6	0.0301	0.0673	-0.1621	-0.1590	-0.1381	-0.1305
7	0.0144	0.0191	-0.1707	-0.1730	-0.1549	-0.1470
8	0.0332	0.0486	-0.2231	-0.2205	-0.1917	-0.1807
9	0.0184	0.0364	-0.1674	-0.1685	-0.1487	-0.1405
10	0.0242	0.0191	-0.2569	-0.2469	-0.2015	-0.1853
11	0.0447	0.0628	-0.2477	-0.2316	-0.1818	-0.1654
12	0.0300	0.0350	-0.2276	-0.2169	-0.1760	-0.1619
13	0.0374	0.0238	-0.3165	-0.2989	-0.2378	-0.2170
14	0.0215	0.0443	-0.1467	-0.1415	-0.1143	-0.1046
15	0.0415	0.0319	-0.3044	-0.2813	-0.2137	-0.1915

16	0.0226	0.0288	-0.2002	-0.1880	-0.1435	-0.1282
17	0.0294	0.0565	-0.1907	-0.1891	-0.1668	-0.1582
18	0.0450	0.0470	-0.3129	-0.2939	-0.2352	-0.2159
19	0.0423	0.0716	-0.2074	-0.2022	-0.1708	-0.1594
20	0.0468	0.0247	-0.3631	-0.3433	-0.2762	-0.2534

APPENDIX E

AEP RESULTS FOR THREE DESIGN VARIABLE DOE

The following table lists the values of the design variables and the AEP results considering four mean wind speeds of the 57 tubercle configurations generated by the three-dimensional DoE.

Table E.1: $\overline{\Delta \text{AEP}}$ for different mean wind speeds of the three design variable DoE

Case	$\bar{A}$	$\bar{\lambda}$	N_{peaks}	$\bar{z}_{\text{tub}}$	$\overline{U}$			
					8 m/s	10 m/s	16 m/s	20 m/s
1	0.0133	0.0555	1	0.0370	**0.0167**	**0.0258**	**0.0374**	**0.0400**
2	0.0404	0.0584	8	0.5838	-0.2516	-0.2302	-0.1656	-0.1442
3	0.0392	0.0216	25	0.7049	-0.3141	-0.3080	-0.2659	-0.2502
4	0.0255	0.0674	6	0.4944	-0.1344	-0.1267	-0.0968	-0.0865
5	0.0212	0.0316	18	0.7383	-0.1967	-0.1926	-0.1618	-0.1503
6	0.0329	0.0542	12	0.8305	-0.2308	-0.2201	-0.1797	-0.1660
7	0.0162	0.0195	3	0.0650	-0.0104	-0.0141	-0.0182	-0.0190
8	0.0369	0.0233	30	0.9182	-0.3003	-0.2835	-0.2269	-0.2077
9	0.0263	0.0693	8	0.6928	-0.1224	-0.1233	-0.1121	-0.1075
10	0.0102	0.0334	15	0.6451	-0.0892	-0.0895	-0.0723	-0.0650
11	0.0171	0.0606	10	0.7679	-0.0776	-0.0853	-0.0882	-0.0877
12	0.0240	0.0400	5	0.2398	-0.0798	-0.0827	-0.0667	-0.0591
13	0.0183	0.0362	2	0.0724	**0.0021**	**0.0048**	**0.0087**	**0.0097**
14	0.0146	0.0473	15	0.9150	-0.0902	-0.0883	-0.0727	-0.0670

15	0.0325	0.0526	3	0.1753	**0.0012**	-0.0247	-0.0541	-0.0596
16	0.0407	0.0748	7	0.6484	-0.1835	-0.1720	-0.1308	-0.1167
17	0.0292	0.0292	16	0.6032	-0.2415	-0.2254	-0.1717	-0.1535
18	0.0496	0.0510	13	0.8496	-0.3087	-0.2944	-0.2429	-0.2253
19	0.0283	0.0645	4	0.3008	**0.0122**	-0.0044	-0.0193	-0.0210
20	0.0433	0.0492	3	0.1639	-0.1399	-0.1454	-0.1347	-0.1291
21	0.0426	0.0344	9	0.3896	-0.1895	-0.1881	-0.1558	-0.1427
22	0.0466	0.0390	16	0.8062	-0.3130	-0.2922	-0.2286	-0.2075
23	0.0454	0.0435	9	0.4925	-0.3106	-0.2910	-0.2251	-0.2029
24	0.0349	0.0623	4	0.2907	-0.0800	-0.0863	-0.0734	-0.0663
25	0.0233	0.0657	11	0.9197	-0.1352	-0.1329	-0.1140	-0.1071
26	0.0121	0.0266	15	0.5136	-0.1118	-0.1000	-0.0586	-0.0442
27	0.0361	0.0438	4	0.2044	-0.1669	-0.1768	-0.1695	-0.1642
28	0.0197	0.0719	5	0.4312	-0.0517	-0.0457	-0.0237	-0.0162
29	0.0313	0.0256	11	0.3583	-0.2422	-0.2316	-0.1837	-0.1667
30	0.0477	0.0163	13	0.2711	-0.2581	-0.2682	-0.2601	-0.2547
31	0.0100	0.0160	1	0.0107	**0.0033**	**0.0041**	**0.0021**	**0.0010**
32	0.0300	0.0160	1	0.0107	**0.0012**	**0.0051**	**0.0121**	**0.0141**
33	0.0500	0.0160	1	0.0107	-0.0031	-0.0012	**0.0035**	**0.0049**
34	0.0100	0.0455	1	0.0303	**0.0910**	**0.0853**	**0.0720**	**0.0683**
35	0.0300	0.0455	1	0.0303	**0.0042**	**0.0084**	**0.0123**	**0.0128**
36	0.0500	0.0455	1	0.0303	**0.0870**	**0.0784**	**0.0589**	**0.0531**
37	0.0100	0.0750	1	0.0500	-0.0056	-0.0072	-0.0084	-0.0085
38	0.0300	0.0750	1	0.0500	-1.5824e-4	**0.0021**	**0.0057**	**0.0067**
39	0.0500	0.0750	1	0.0500	-0.0113	-0.0182	-0.0289	-0.0315
40	0.0100	0.0160	24	0.5013	-0.1179	-0.1040	-0.0615	-0.0472
41	0.0300	0.0160	24	0.5013	-0.2253	-0.2259	-0.1956	-0.1830

42	0.0500	0.0160	24	0.5013	-0.3681	-0.3611	-0.3155	-0.2988
43	0.0100	0.0455	9	0.5157	-0.0512	-0.0564	-0.0568	-0.0559
44	0.0300	0.0455	9	0.5157	-0.2097	-0.1878	-0.1242	-0.1033
45	0.0500	0.0455	9	0.5157	-0.3167	-0.2950	-0.2244	-0.2007
46	0.0100	0.0750	6	0.5500	-0.0117	-0.0042	**0.0057**	**0.0078**
47	0.0300	0.0750	6	0.5500	-0.1211	-0.1063	-0.0619	-0.0470
48	0.0500	0.0750	6	0.5500	-0.2460	-0.2272	-0.1661	-0.1455
49	0.0100	0.0160	47	0.9920	-0.1433	-0.1404	-0.1143	-0.1043
50	0.0300	0.0160	47	0.9920	-0.3228	-0.3152	-0.2696	-0.2528
51	0.0500	0.0160	47	0.9920	-0.4285	-0.4221	-0.3763	-0.3593
52	0.0100	0.0455	16	0.9403	-0.0576	-0.0580	-0.0486	-0.0448
53	0.0300	0.0455	16	0.9403	-0.2185	-0.2093	-0.1710	-0.1578
54	0.0500	0.0455	16	0.9403	-0.3295	-0.3059	-0.2391	-0.2174
55	0.0100	0.0750	10	0.9500	-0.0062	-0.0061	-0.0053	-0.0049
56	0.0300	0.0750	10	0.9500	-0.1289	-0.1287	-0.1133	-0.1072
57	0.0500	0.0750	10	0.9500	-0.2157	-0.2042	-0.1626	-0.1484

REFERENCES

[1] S. Aftab, N. Razak, A. M. Rafie, and K. Ahmad, "Mimicking the humpback whale: An aerodynamic perspective," *Progress in Aerospace Sciences*, vol. 84, pp. 48–69, 2016.

[2] Airbus, *Biomimicry: Engineering in nature's style*, https://www.airbus.com/newsroom/news/en/2018/01/biomimicry–engineering-in-nature-s-style.html.

[3] R. S. Amano, "Review of wind turbine research in 21st century," *Journal of Energy Resources Technology*, vol. 139, no. 5, p. 050 801, 2017.

[4] I. Aramendia, U. Fernandez-Gamiz, J. A. Ramos-Hernanz, J. Sancho, J. M. Lopez-Guede, and E. Zulueta, "Flow control devices for wind turbines," in *Energy Harvesting and Energy Efficiency*, Springer, 2017, pp. 629–655.

[5] A. C. Aranake, V. K. Lakshminarayan, and K. Duraisamy, "Assessment of transition model and cfd methodology for wind turbine flows," in *42nd AIAA Fluid Dynamics Conference and Exhibit*, 2012.

[6] M. Asli, B. Mashhadi Gholamali, and A. Mesgarpour Tousi, "Numerical analysis of wind turbine airfoil aerodynamic performance with leading edge bump," *Mathematical Problems in Engineering*, vol. 2015, 2015.

[7] C.-J. Bai, W.-C. Wang, and P.-W. Chen, "The effects of sinusoidal leading edge of turbine blades on the power coefficient of horizontal-axis wind turbine (hawt)," *International journal of green energy*, vol. 13, no. 12, pp. 1193–1200, 2016.

[8] Y. Bar-Cohen, *Biomimetics: biologically inspired technologies*. CRC Press, 2005.

[9] L. Bellequant and L. E. Howle, "Whalepower wenvor blade," 2009.

[10] D. Berg, S. J. Johnson, and C. Van Dam, "Active load control techniques for wind turbines," *Sandia Report, SAND2008-4809*, 2008.

[11] B. Bhushan, *Biomimetics: Lessons from nature–an overview*, 2009.

[12] M. I. Blanco, "The economics of wind energy," *Renewable and sustainable energy reviews*, vol. 13, no. 6-7, pp. 1372–1382, 2009.

[13] M. D. Bolzon, R. M. Kelso, and M. Arjomandi, "Tubercles and their applications," *Journal of Aerospace Engineering*, vol. 29, no. 1, p. 04 015 013, 2015.

[14] ——, "Parametric study of the effects of a tubercle's geometry on wing performance through the use of the lifting-line theory," in *54th AIAA Aerospace Sciences Meeting*, 2016, p. 0295.

[15] T. Burton, D. Sharpe, N. Jenkins, and E. Bossanyi, *Wind energy handbook*. John Wiley & Sons, 2001.

[16] D. M. Bushnell and K. Moore, "Drag reduction in nature," *Annual review of fluid mechanics*, vol. 23, no. 1, pp. 65–79, 1991.

[17] K. M. Carley, N. Y. Kamneva, and J. Reminga, "Response surface methodology," DTIC Document, Tech. Rep., 2004.

[18] D. Chao and C. Van Dam, "Computational aerodynamic analysis of a blunt trailing-edge airfoil modification to the nrel phase vi rotor," *Wind Energy*, vol. 10, no. 6, pp. 529–550, 2007.

[19] Y.-P. Chen, "A study of the aerodynamic behavior of a nrel phase vi wind turbine using the cfd methodology," PhD thesis, Wright State University, 2011.

[20] M. Chen Quin Lam, "Sequential adaptive designs in computer experiments for response surface model fit," PhD thesis, The Ohio State University, 2008.

[21] H. Choi, "Bio-mimetic flow control," in *APS Division of Fluid Dynamics Meeting Abstracts*, 2009.

[22] H. Choi, H. Park, W. Sagong, and S.-i. Lee, "Biomimetic flow control based on morphological features of living creatures," *Physics of Fluids*, vol. 24, no. 12, p. 121 302, 2012.

[23] F. G. Collins, "Boundary-layer control on wings using sound and leading-edge serrations," *AIAA Journal*, vol. 19, no. 2, pp. 129–130, 1981.

[24] J. Conti, P. Holtberg, J. Diefenderfer, A. LaRose, J. T. Turnure, and L. Westfall, "International energy outlook 2016 with projections to 2040," USDOE Energy Information Administration (EIA), Washington, DC (United States). Office of Energy Analysis, Tech. Rep., 2016.

[25] B. Cranston, C. Laux, and A. Altman, "Leading edge serrations on flat plates at low reynolds number," in *50th AIAA Aerospace Sciences Meeting including the New Horizons Forum and Aerospace Exposition*, 2012, p. 53.

[26] K. Crombecq, D. Gorissen, D. Deschrijver, and T. Dhaene, "A novel hybrid sequential design strategy for global surrogate modeling of computer experiments," *SIAM Journal on Scientific Computing*, vol. 33, no. 4, pp. 1948–1974, 2011.

[27] D. Custodio, "The effect of humpback whale-like leading edge protuberances on hydrofoil performance," PhD thesis, Worcester Polytechnic Institute, 2007.

[28] A Dropkin, D Custodio, C. Henoch, and H Johari, "Computation of flow field around an airfoil with leading-edge protuberances," *Journal of Aircraft*, vol. 49, no. 5, pp. 1345–1355, 2012.

[29] J. E. Guerreiro and J. M. Sousa, "Low-reynolds-number effects in passive stall control using sinusoidal leading edges," *AIAA journal*, vol. 50, no. 2, pp. 461–469, 2012.

[30] R. Edel and H. Winn, "Observations on underwater locomotion and flipper movement of the humpback whale megaptera novaeangliae," *Marine Biology*, vol. 48, no. 3, pp. 279–287, 1978.

[31] J. Favier, A. Pinelli, and U. Piomelli, "Control of the separated flow around an airfoil using a wavy leading edge inspired by humpback whale flippers," *Comptes Rendus Mecanique*, vol. 340, no. 1, pp. 107–114, 2012.

[32] F Fish, P Legac, T Wei, and T Williams, "Vortex mechanics associated with propulsion and control in whales and dolphins," *Comparative Biochemistry and Physiology, Part A*, vol. 3, no. 150, S65–S66, 2008.

[33] F. Fish and G. Lauder, "Passive and active flow control by swimming fishes and mammals," *Annu. Rev. Fluid Mech.*, vol. 38, pp. 193–224, 2006.

[34] F. E. Fish, "Limits of nature and advances of technology: What does biomimetics have to offer to aquatic robots?" *Applied Bionics and Biomechanics*, vol. 3, no. 1, pp. 49–60, 2006.

[35] F. E. Fish, L. E. Howle, and M. M. Murray, "Hydrodynamic flow control in marine mammals," *Integrative and Comparative Biology*, vol. 48, no. 6, pp. 788–800, 2008.

[36] F. E. Fish, P. W. Weber, M. M. Murray, and L. E. Howle, "The tubercles on humpback whales' flippers: Application of bio-inspired technology," *Integrative and comparative biology*, vol. 51, no. 1, pp. 203–213, 2011.

[37] F. E. Fish and J. M. Battle, "Hydrodynamic design of the humpback whale flipper," *Journal of Morphology*, vol. 225, no. 1, pp. 51–60, 1995.

[38] A. Garbo and B. J. German, "Comparison of adaptive design space exploration methods applied to s-duct cfd simulation," in *57th AIAA/ASCE/AHS/ASC Structures, Structural Dynamics, and Materials Conference*, 2016, p. 0416.

[39] ——, "Performance assessment of a cross-validation sampling strategy with active surrogate model selection," *Structural and Multidisciplinary Optimization*, pp. 1–16, 2019.

[40] G. Godard and M. Stanislas, "Control of a decelerating boundary layer. part 1: Optimization of passive vortex generators," *Aerospace Science and Technology*, vol. 10, no. 3, pp. 181–191, 2006.

[41] D. T. Grant, M. Abdulrahim, and R. Lind, "Design and analysis of biomimetic joints for morphing of micro air vehicles," *Bioinspiration & biomimetics*, vol. 5, no. 4, p. 045 007, 2010.

[42] J. S. Greene and M. Morrissey, "Estimated pollution reduction from wind farms in oklahoma and associated economic and human health benefits," *Journal of Renewable Energy*, vol. 2013, 2013.

[43] T. T. Group, *Mapping the world's renewable energy potential*, http://blog.fabric.ch-/index.php?/archives/84-Mapping-the-Worlds-Renewable-Energy-Potential.html.

[44] A. Gupta, A. Alsultan, R. Amano, S. Kumar, and A. D. Welsh, "Design and analysis of wind turbine blades: Winglet, tubercle, and slotted," in *ASME Turbo Expo 2013: Turbine Technical Conference and Exposition*, American Society of Mechanical Engineers, 2013, V008T44A024–V008T44A024.

[45] GWEC, "Global wind energy council report 2016," Tech. Rep., 2016.

[46] ——, "Global wind energy council report 2018," Tech. Rep., 2018.

[47] Z. Han, Z. Mu, W. Yin, W. Li, S. Niu, J. Zhang, and L. Ren, "Biomimetic multifunctional surfaces inspired from animals," *Advances in Colloid and Interface Science*, vol. 234, pp. 27–50, 2016.

[48] M. Hand, D. Simms, L. Fingersh, D. Jager, J. Cotrell, S Schreck, and S. Larwood, "Unsteady aerodynamics experiment phase vi: Wind tunnel test configurations and available data campaigns," *National Renewable Energy Laboratory, Golden, CO, Report No. NREL/TP-500-29955*, 2001.

[49] K. L. Hansen, R. M. Kelso, and B. B. Dally, "Performance variations of leading-edge tubercles for distinct airfoil profiles," *AIAA journal*, vol. 49, no. 1, pp. 185–194, 2011.

[50] K. L. Hansen, N. Rostamzadeh, R. M. Kelso, and B. B. Dally, "Evolution of the streamwise vortices generated between leading edge tubercles," *Journal of Fluid Mechanics*, vol. 788, pp. 730–766, 2016.

[51] K. L. Hansen, "Effect of leading edge tubercles on airfoil performance.," PhD thesis, 2012.

[52] J. P. Hennessey Jr, "A comparison of the weibull and rayleigh distributions for estimating wind power potential," *Wind Engineering*, pp. 156–164, 1978.

[53] G.-Y. Huang, Y. Shiah, C.-J. Bai, and W. Chong, "Experimental study of the protuberance effect on the blade performance of a small horizontal axis wind turbine," *Journal of Wind Engineering and Industrial Aerodynamics*, vol. 147, pp. 202–211, 2015.

[54] M. Ibrahim, A. Alsultan, S. Shen, and R. S. Amano, "Advances in horizontal axis wind turbine blade designs: Introduction of slots and tubercle," *Journal of Energy Resources Technology*, vol. 137, no. 5, p. 051 205, 2015.

[55] K. Isaac and T. Swanson, "Biologically inspired wing leading edge for enhanced wind turbine and aircraft performance," in *6th AIAA Theoretical Fluid Mechanics Conference*, 2011, p. 3533.

[56] M. Islam, S Mekhilef, and R Saidur, "Progress and recent trends of wind energy technology," *Renewable and Sustainable Energy Reviews*, vol. 21, pp. 456–468, 2013.

[57] S. ITO, "Aerodynamic influence of leading-edge serrations on an airfoil in a low reynolds number," *Journal of Biomechanical Science and Engineering*, vol. 4, no. 1, pp. 117–123, 2009.

[58] J. Johansen, N. Sorensen, J. Michelsen, and S Schreck, "Detached-eddy simulation of flow around the nrel phase-vi blade," in *ASME 2002 Wind Energy Symposium*, American Society of Mechanical Engineers, 2002, pp. 106–114.

[59] H. Johari, C. W. Henoch, D. Custodio, and A. Levshin, "Effects of leading-edge protuberances on airfoil performance," *AIAA journal*, vol. 45, no. 11, pp. 2634–2642, 2007.

[60] C. Justus, W. Hargraves, A. Mikhail, and D. Graber, "Methods for estimating wind speed frequency distributions," *Journal of applied meteorology*, vol. 17, no. 3, pp. 350–353, 1978.

[61] Y. A. Kaplan, "Overview of wind energy in the world and assessment of current wind energy policies in turkey," *Renewable and Sustainable Energy Reviews*, vol. 43, pp. 562–568, 2015.

[62] S. Klän, M. Klaas, and W. Schröder, "The influence of leading edge serrations on the flow field of an artificial owl wing," in *28th AIAA Applied Aerodynamics Conference*, 2010, p. 4942.

[63] S. Kumar and R. Amano, "Wind turbine blade design and analysis with tubercle technology," in *ASME 2012 International Design Engineering Technical Conferences and Computers and Information in Engineering Conference*, American Society of Mechanical Engineers, 2012, pp. 859–872.

[64] Y. Kumar, J. Ringenberg, S. S. Depuru, V. K. Devabhaktuni, J. W. Lee, E. Nikolaidis, B. Andersen, and A. Afjeh, "Wind energy: Trends and enabling technologies," *Renewable and Sustainable Energy Reviews*, vol. 53, pp. 209–224, 2016.

[65] R. Langtry, J. Gola, and F. Menter, "Predicting 2d airfoil and 3d wind turbine rotor performance using a transition model for general cfd codes," in *44th AIAA aerospace sciences meeting and exhibit*, 2006, p. 395.

[66] R Lanzafame and M Messina, "Optimal wind turbine design to maximize energy production," *Proceedings of the Institution of Mechanical Engineers, Part A: Journal of Power and Energy*, vol. 223, no. 2, pp. 93–101, 2009.

[67] ——, "Horizontal axis wind turbine working at maximum power coefficient continuously," *Renewable Energy*, vol. 35, no. 1, pp. 301–306, 2010.

[68] K. Lee, Z. Huque, R. Kommalapati, and S.-E. Han, "Fluid-structure interaction analysis of nrel phase vi wind turbine: Aerodynamic force evaluation and structural analysis using fsi analysis," *Renewable Energy*, vol. 113, pp. 512–531, 2017.

[69] G. Lilley, "A study of the silent flight of the owl," in *4th AIAA/CEAS Aeroacoustics Conference*, 1998, p. 2340.

[70] T. Liu, K. Kuykendoll, R. Rhew, and S. Jones, "Avian wing geometry and kinematics," *AIAA journal*, vol. 44, no. 5, pp. 954–963, 2006.

[71] T. Mackman, C. Allen, M. Ghoreyshi, and K. Badcock, "Comparison of adaptive sampling methods for generation of surrogate aerodynamic models," *AIAA journal*, vol. 51, no. 4, pp. 797–808, 2013.

[72] R. Mahu and F. Popescu, "Nrel phase vi rotor modeling and simulation using ansys fluent 12.1," *Mathematical Modeling in Civil Engineering*, 2011.

[73] J. F. Manwell, J. G. McGowan, and A. L. Rogers, *Wind energy explained: theory, design and application*. John Wiley & Sons, 2010.

[74] S. Mathew, *Wind energy: fundamentals, resource analysis and economics*. Springer, 2006, vol. 1.

[75] B. D. Mattos, J. Meneghini, B. R. Padilha, and A. A. de Paula, "The airfoil thickness effect on wavy leading edge performance," in *54th AIAA Aerospace Sciences Meeting*, 2016, p. 1306.

[76] J. Melo De Sousa and J. Camara, "Numerical study on the use of a sinusoidal leading edge for passive stall control at low reynolds number," in *51st AIAA Aerospace Sciences Meeting including the New Horizons Forum and Aerospace Exposition*, 2013, p. 62.

[77] D. S. Miklosovic, M. M. Murray, and L. E. Howle, "Experimental evaluation of sinusoidal leading edges," *Journal of aircraft*, vol. 44, no. 4, pp. 1404–1408, 2007.

[78] D. Miklosovic, M. Murray, L. Howle, and F. Fish, "Leading-edge tubercles delay stall on humpback whale (megaptera novaeangliae) flippers," *Physics of Fluids (1994-present)*, vol. 16, no. 5, pp. L39–L42, 2004.

[79] J.-O. Mo and Y.-H. Lee, "Cfd investigation on the aerodynamic characteristics of a small-sized wind turbine of nrel phase vi operating with a stall-regulated method," *Journal of mechanical science and technology*, vol. 26, no. 1, pp. 81–92, 2012.

[80] B. R. Munson, D. F. Young, and T. H. Okiishi, "Fundamentals of fluid mechanics," *New York*, vol. 3, no. 4, 1990.

[81] A. A. de Paula, J. Meneghini, V. G. Kleine, and R. D. Girardi, "The wavy leading edge performance for a very thick airfoil," in *55th AIAA Aerospace Sciences Meeting*, 2017, p. 0492.

[82] G. Pechlivanoglou, "Passive and active flow control solutions for wind turbine blades," 2013.

[83] H. T. Pedro and M. H. Kobayashi, "Numerical study of stall delay on humpback whale flippers," in *46th AIAA Aerospace Sciences Meeting and Exhibit*, 2008, pp. 2008–0584.

[84] N. V. Queipo, R. T. Haftka, W. Shyy, T. Goel, R. Vaidyanathan, and P. K. Tucker, "Surrogate-based analysis and optimization," *Progress in aerospace sciences*, vol. 41, no. 1, pp. 1–28, 2005.

[85] N Rostamzadeh, R. Kelso, B. Dally, and K. Hansen, "The effect of undulating leading-edge modifications on naca 0021 airfoil characteristics," *Physics of Fluids (1994-present)*, vol. 25, no. 11, p. 117 101, 2013.

[86] J. Seguro and T. Lambert, "Modern estimation of the parameters of the weibull wind speed distribution for wind energy analysis," *Journal of Wind Engineering and Industrial Aerodynamics*, vol. 85, no. 1, pp. 75–84, 2000.

[87] N. Sezer-Uzol and L. N. Long, "3-d time-accurate cfd simulations of wind turbine rotor flow fields," *AIAA paper*, vol. 394, p. 2006, 2006.

[88] A. Skillen, A. Revell, A. Pinelli, U. Piomelli, and J. Favier, "Flow over a wing with leading-edge undulations," *Aiaa Journal*, vol. 53, no. 2, pp. 464–472, 2014.

[89] Y. Song and J. B. Perot, "Cfd simulation of the nrel phase vi rotor," *Wind engineering*, vol. 39, no. 3, pp. 299–309, 2015.

[90] N. N. Sørensen, J. Michelsen, and S Schreck, "Navier–stokes predictions of the nrel phase vi rotor in the nasa ames 80 ft x 120 ft wind tunnel," *Wind Energy*, vol. 5, no. 2-3, pp. 151–169, 2002.

[91] D. A. Spera *et al.*, *Wind turbine technology: fundamental concepts of wind turbine engineering*. ASME press New York, 1994, vol. 3.

[92] B Stein and M. Murray, "Stall mechanism analysis of humpback whale flipper models," *Proceedings of Unmanned Untethered Submersible Technology (UUST), UUST05*, vol. 5, 2005.

[93] F. W. True, *The Whalebone Whales of the Western North Atlantic: Compared with Those Occurring in European Waters*, 1414. Smithsonian institution, 1904.

[94] E. A. Van Nierop, S. Alben, and M. P. Brenner, "How bumps on whale flippers delay stall: An aerodynamic model," *Physical review letters*, vol. 100, no. 5, p. 054 502, 2008.

[95] H. Wagner, M. Weger, M. Klaas, and W. Schröder, "Features of owl wings that promote silent flight," *Interface focus*, vol. 7, no. 1, p. 20 160 078, 2017.

[96] Z. Wang and M. Zhuang, "Leading-edge serrations for performance improvement on a vertical-axis wind turbine at low tip-speed-ratios," *Applied Energy*, vol. 208, pp. 1184–1197, 2017.

[97] P. Watts and F. E. Fish, "The influence of passive, leading edge tubercles on wing performance," in *Proc. Twelfth Intl. Symp. Unmanned Untethered Submers. Technol*, Auton. Undersea Syst. Inst. Durham New Hampshire, 2001.

[98] P. W. Weber, L. E. Howle, and M. M. Murray, "Lift, drag, and cavitation onset on rudders with leading-edge tubercles," *Marine technology*, vol. 47, no. 1, pp. 27–36, 2010.

[99] P. W. Weber, L. E. Howle, M. M. Murray, and D. S. Miklosovic, "Computational evaluation of the performance of lifting surfaces with leading-edge protuberances," *Journal of Aircraft*, vol. 48, no. 2, pp. 591–600, 2011.

[100] H. Xin, G. Rui, J.-f. JIN, Y.-r. LIU, M. Yi, C. Qian, and Y. ZHENG, "Numerical simulation and aerodynamic performance comparison between seagull aerofoil and naca 4412 aerofoil under low-reynolds," *Advances in Natural Science*, vol. 3, no. 2, pp. 244–250, 2010.

[101] M. M. Yelmule and E. A. Vsj, "Cfd predictions of nrel phase vi rotor experiments in nasa/ames wind tunnel," *International Journal of Renewable Energy Research (IJRER)*, vol. 3, no. 2, pp. 261–269, 2013.

[102] D. Yen, C Van Dam, F. Braeuchle, R Smith, and S Collins, "Active load control and lift enhancement using mem translational tabs," in *Fluids 2000 Conference and Exhibit*, 2000, p. 2242.

[103] H. Yoon, P. Hung, J. Jung, and M. Kim, "Effect of the wavy leading edge on hydrodynamic characteristics for flow around low aspect ratio wing," *Computers & Fluids*, vol. 49, no. 1, pp. 276–289, 2011.

[104] M. Zhang, G. Wang, and J. Xu, "Aerodynamic control of low-reynolds-number airfoil with leading-edge protuberances," *AIAA journal*, vol. 51, no. 8, pp. 1960–1971, 2013.

[105] ——, "Experimental study of flow separation control on a low-re airfoil using leading-edge protuberance method," *Experiments in fluids*, vol. 55, no. 4, p. 1710, 2014.

[106] R.-K. Zhang and V. D.J.-Z. Wu, "Aerodynamic characteristics of wind turbine blades with a sinusoidal leading edge," *Wind Energy*, vol. 15, no. 3, pp. 407–424, 2012.

[107] G.-H. Zhu, "Comment on how bumps on whale flippers delay stall: An aerodynamic model," *Physical review letters*, vol. 101, no. 10, p. 109 401, 2008.

[108] D. S. Zinger and E. Muljadi, "Annualized wind energy improvement using variable speeds," *IEEE Transactions on Industry Applications*, vol. 33, no. 6, pp. 1444–1447, 1997.